

# UNIVERSITÀ DEGLI STUDI DI NAPOLI FEDERICO II

INGEGNERIA STRUTTURALE, GEOTECNICA E RISCHIO SISMICO



*Dottorato di ricerca*

In

**INGEGNERIA STRUTTURALE,  
GEOTECNICA E RISCHIO SISMICO  
XXXIII CICLO**

Bayesian inference of focal mechanisms and  
backprojection methods for source kinematics  
characterization

Stefania Tarantino

**Relatore**  
Prof. Antonio Emolo

**Coordinatore**  
Prof. Luciano Rosati



I would like to say thank you to all the people who taught me during this academic course and during my personal life that walked with it. It was an incredible time in an incredible historical moment. I would say thanks to the research group at RISSClab lead by Prof. Aldo Zollo, to my supervisor, Prof. Antonio Emolo, my supervisor at UCLA, professor Lingsen Meng and to his research group, to the doctorate coordinator Prof. Luciano Rosati and all the committee, to the external reviewers of this thesis, Prof. Jiri Zahradnik and Dr. Laura Scognamiglio for their insightful comments, and deep questions which offer scientific growth prospects.

Finally, I would say thanks to my family and my dear friends.

For me it was incredible to do and try to do research, for this I thank my country that tries to give the same opportunities to all citizens. However, this right can mean something only if your family supports you, as my family did strongly for me, because there are no rights if there is no one to watch over them.

I thank the good luck of being born in this society, even if there is still so much to do to destroy gender, religious and racial differences. I think that society can still learn something else from the scientific community, that is how to stay peaceful in the world.

# CONTENTS

---

Introduction.....	5
1 Theory framework .....	21
1.1 The Seismic source.....	21
1.1.1 Point source .....	25
1.1.2 Single and double couples .....	30
1.1.3 Radiation Pattern .....	31
1.1.4 Fault mechanisms and classification.....	33
1.1.5 Fault mechanism computation .....	36
1.1.6 Information from a focal mechanism .....	41
1.1.7 Kagan's angle .....	43
1.2 Early warning systems: from scientific fundamentals toward the new generation of systems.....	48
1.2.1 Network- and Station-based EEWS Systems .....	50
1.2.2 The Next Generation of the EEWS Systems.....	52
1.3 Back Projection .....	54
1.3.1 Beamforming and Stacking Back Projection for network .....	55
1.3.2 Multi Array Back Projection .....	58
1.4 Inverse Methods .....	62
1.4.1 Formulation of the inverse problem.....	62
1.4.2 Least squares solution.....	65
1.4.3 Estimation of the error associated with the least squares' solution .....	66
1.4.4 Linearization of inverse methods.....	69
1.4.5 Non-linear Inverse method.....	70
2 Methodology for Focal Mechanism estimation.....	73
2.1 Offline application.....	73
2.2 Real Time application with evolutionary approach .....	78
3 Application of methodology of focal mechanism estimation.....	81
3.1 Evolutionary approach in simulated Real Time .....	81
3.1.1 Application to 2016-2017 Central Italy sequence with P-wave peak amplitudes .....	81

3.1.2	Application to Mw 6.5 Norcia earthquake with jointly use of P-wave peak amplitudes and P-wave polarities.....	85
3.2	Offline approach applied to micro seismicity for focal mechanism estimation	87
3.2.1	Nagano, Japan .....	88
3.2.2	Rocca San Felice .....	92
4	Back Projection application.....	102
4.1	Back Projection on synthetic test .....	102
4.1.1	Set up of model and forward simulation .....	103
4.1.2	BP application and results.....	105
4.1.3	Application to the 2016, Mw 6.5 Norcia earthquake .....	117
4.2	Multi-Array Back Projection .....	120
4.2.1	The 2015, Mw 8.3, Illapel Earthquake .....	122
4.2.2	The 2010, Mw 7.2, El Mayor Cucapah earthquake .....	124
4.2.3	2016, Mw 6.5 Norcia earthquake .....	126
5	Conclusions .....	132
	References.....	137
	Appendix.....	145

INDEX OF FIGURES:

FIGURE 1.1: A SEISMIC FAULT IS HERE REPRESENTED AS A SURFACE INSIDE A VOLUME  $V$  ALONG WHICH SLIP OCCURS. THE TWO LIPS OF THE FAULT ARE SEPARATED TO INTERPRET THE DISPLACEMENT DISCONTINUITY ACROSS SUCH A SURFACE, FIGURE FROM FESTA AND ZOLLO,2006 ..... 22

FIGURE 1.2: THE DOUBLE COUPLE WHICH CAN BE USED AS AN ELEMENTARY SOURCE FOR THE COMPUTATION OF THE REPRESENTATION INTEGRAL, FIGURE FROM FESTA AND ZOLLO (2012) ..... 24

FIGURE 1.3: THE REAL FRACTURE PROCESS AT THE SOURCE INVOLVES A SERIES OF RATHER COMPLEX PHENOMENA. IT CAN BE APPROXIMATED BY AN AVERAGE DISPLACEMENT MODEL AS A FUNCTION OF TIME THAT CAN BE REPRESENTED BY AN EQUIVALENT SYSTEM OF FORCES WHICH CAN BE INCORPORATED DIRECTLY INTO THE EQUATIONS OF MOTION. FIGURE TAKEN FROM T. LAY AND T.C. WALLACE (1995). MODERN GLOBAL SEISMOLOGY. ACADEMIC PRESS..... 31

FIGURE 1.4: RADIATION PATTERN OF THE P WAVES IN FAR FIELD AND HIGH-FREQUENCY APPROXIMATION FOR A VERTICAL FAULT. THE GREY ARROWS INDICATE THE SLIDING DIRECTION WITH RESPECT TO THE FAULT PLANE. THE BLACK ARROWS REPRESENT THE AMPLITUDE OF THE P WAVE, AS THE AZIMUTH VARIES  $\Theta$  WITH RESPECT TO THE FAULT PLANE. THIS DIAGRAM IS IDENTICAL EITHER FOR A SINGLE PAIR OR DOUBLE PAIR SOURCE..... 31

FIGURE 1.5: RADIATION DIAGRAMS FOR P AND S WAVES IN FAR FIELD APPROXIMATION FOR SINGLE AND DOUBLE MODELS COUPLE (ZOLLO AND EMOLO, TERREMOTI E ONDE 2011)..... 32

FIGURE 1.6: DOUBLE PAIR OF FORCES SYSTEM. FIGURE SHOWS THE SYSTEM ASSOCIATED WITH A VERTICAL TRANSCURRENT FAULT LEFT (PARAGRAPH 8.2.6) FACING NORTH. A COMPLETELY EQUIVALENT SYSTEM IS MADE UP OF TWO DIPOLES (MAIN AXES). THE FIGURE IS INSPIRED BY A SIMILAR EXAMPLE REPORTED IN T. LAY AND T.C. WALLACE (1995). MODERN GLOBAL SEISMOLOGY. ACADEMIC PRESS ..... 33

FIGURE 1.7: CONVENTION FOR THE IDENTIFICATION OF THE TWO BLOCKS ON BOTH SIDES OF A NON-VERTICAL FAULT. THE BLOCK ABOVE OF THE FAULT IS KNOWN AS THE HANGING WALL WHILE THE BLOCK BELOW IT IS CALLED FOOT-WALL (ZOLLO AND EMOLO, TERREMOTI E ONDE, 2011)..... 33

FIGURE 1.8: DEFINITION OF THE FAULT ORIENTATION PARAMETERS AND OF THE SLIP VECTOR..... 34

FIGURE 1.9: EXAMPLE OF DIFFERENT FAULTS; FIGURE FROM T. LAY AND T.C. WALLACE (1995), MODERN GLOBAL SEISMOLOGY. ACADEMIC PRESS ..... 35

FIGURE 1.10: FOCAL SPHERE (ZOLLO AND EMOLO, TERREMOTI E ONDE,2011)..... 36

FIGURE 1.11: SIGN OF THE INITIAL MOTION P WITH RESPECT TO THE PLANE OF FAULT AND TO THE AUXILIARY PLANE (ZOLLO AND EMOLO, TERREMOTI E ONDE, 2011). ..... 38

FIGURE 1.12: DEFINITION OF A GEOGRAPHICAL REFERENCE SYSTEM WITH THE POSITIVE  $x_3$  AXIS (VERTICAL AXIS) DOWNWARDS. THE STRIKE ANGLE OF THE FAULT PLANE  $\phi_S$  IS MEASURED WITH RESPECT TO THE GEOGRAPHIC NORTH AS WELL AS THE AZIMUTH  $\phi_R$  OF THE RECEIVER. THE DIP  $\Delta$  OF THE FAULT IS MEASURED WITH RESPECT TO THE HORIZONTAL PLANE WHILE THE SLIP ANGLE  $\lambda$ , MEASURED WITH RESPECT TO THE STRIKE DIRECTION, IDENTIFIES THE DIRECTION OF THE VECTOR DISLOCATION ON THE FAULT. THE SEISMIC RAY THAT REACHES THE STATION HAS A TAKE-OFF ANGLE  $i_H$  WITH RESPECT TO THE  $x_3$  AXIS (VERTICAL AXIS).  $x_1$  IS ALONG EAST DIRECTION AND  $x_2$  ALONG NORTH DIRECTION. THE VERSORS  $L$ ,  $M$  AND  $N$  IDENTIFY A REFERENCE SYSTEM IN THE DIRECTIONS, RESPECTIVELY,  $P$ ,  $SV$ , AND  $SH$  (ZOLLO AND EMOLO, TERREMOTI E ONDE, 2011). ..... 40

FIGURE 1.13: EXAMPLE OF BEACHBALL. .... 41

FIGURE 1.14: REPRESENTATION OF THE FOCAL MECHANISMS FOR THE DIFFERENT TYPES OF FAULT. THE REGIONS IN GRAY CORRESPOND TO P MOTIONS OF THE COMPRESSIVE TYPE. THE FIGURES ON THE SIDES OF EACH BEACH BALL REPRESENT THE TWO POSSIBLE TYPE OF MOVEMENT CORRESPONDING TO THE FOCAL MECHANISM, HIGHLIGHTING THE AMBIGUITY EXISTING BETWEEN THE FAULT PLANE AND THAT AUXILIARY..... 42

FIGURE 1.15: EARTHQUAKE EARLY WARNING SYSTEMS EXAMPLE: A) ON-SITE SYSTEM: SOURCE AND STATIONS SITES COINCIDE; B) REGIONAL SYSTEM: STATIONS ARE PLACED NEAR THE SOURCE REGION WHILE TARGETS ARE SITUATED FAR AWAY. ....	48
FIGURE 1.16: CONCEPT OF AN EARTHQUAKE EARLY WARNING SYSTEM (EEW) THERE ARE TWO TYPES OF EEW SYSTEMS: (1) THE FRONT DETECTION/ALARM AND (2) THE ON-SITE DETECTION/ALARM; EACH OF THESE CAN USE TWO TYPES OF TRIGGER: (A) THE EARTHQUAKES' P WAVE, AND (B) ITS S WAVE. FIGURE FROM NAKAMURA ET AL, 2011.....	49
FIGURE 1.17: WARNING- AND LEAD-TIME FOR A. NETWORK-BASED B. ON-SITE SYSTEMS.....	52
FIGURE 1.18: STACKING THE NOISE NOT ALLOWS RETRIEVING A COHERENT SIGNAL, WHILE IN PRESENCE OF A REAL SOURCE THE STACKING PROCESS ALLOWS TO RETRIEVE THE ORIGINAL SOURCE .....	54
FIGURE 1.19: SCHEME OF THE PROCEDURE BY MAERCKLIN ET AL., 2012.....	56
FIGURE 1.20: SKETCH OF STACKING AMPLITUDE BACKPROJECTION: A PLANE ORIENTED AS THE FAULT PLANE IS SUBDIVIDED IN SUBSOURCES. ....	56
FIGURE 1.21: SCHEME OF THE TECHNIQUE OF THE MULTI ARRAY BACK PROJECTION DEVELOPED BY XIE AND MENG (2020) .....	58
FIGURE 1.22: SKETCH OF TRACKING EARTHQUAKE WITH MULTI-ARRAY BACK-PROJECTION METHOD. THE RED STARS REPRESENT THE HYPOCENTER AND EPICENTER. THE EARTHQUAKE RUPTURE AREA (RED ELLIPSE) IS IMAGED BY THE LOCAL SEISMIC NETWORKS ARRAYS (LIGHT AND DARK YELLOW TETRAHEDRONS).....	60
FIGURE 1.23: SCHEME TO REPRESENT THE DISTANCE OF A STATION TO THE NEAREST STRONG SEISMIC RADIATIONS..	60
FIGURE 1.24: (A) THE BEST ESTIMATE MEST OF THE PARAMETER $\mathbf{m}$ IS FOUND IN CORRESPONDENCE WITH THE MINIMUM OF THE FUNCTION $\mathbf{E}(\mathbf{m})$ . IF IN PROXIMITY OF THE MINIMUM THIS FUNCTION IS RELATIVELY NARROW, THEN THE FLUCTUATIONS OF $\mathbf{E}(\mathbf{m})$ GIVE ERRORS $\Delta\mathbf{m}$ ON MEST WHICH ARE SMALL. (B) IF THE FUNCTION $\mathbf{E}(\mathbf{m})$ IS INSTEAD LARGE AROUND THE MINIMUM, THE ERROR ON MEST BECOMES LARGE. ....	67
FIGURE 1.25: THE OCT-TREE SEARCH ALGORITHM STARTS FROM A SUBDIVISION OF THE SPACE THAT IS NOT VERY DENSE AND THEN REFINES THE SEARCH THROUGH RECURSIVE SUBDIVISIONS OF CELLS WITH HIGHER PDF VALUES. THE SAMPLES CORRESPONDING TO EACH CELL OF THE STRUCTURE PROVIDE A USEFUL AND COMPACT REPRESENTATION OF THE PROBABILITY DENSITY FUNCTION. FIGURE TAKEN FROM A. LOMAX AND A. CURTIS (2001) .....	72
FIGURE 2.1: BLOCK DIAGRAM OF THE ALGORITHM. THE ALGORITHM CAN WORK WITH MULTIPLE DATASETS WITH THEIR OWN PROCESSING TO GET DATA CONDITIONAL PROBABILITY FUNCTIONS, WHICH COMBINED TOGETHER PROVIDE THE DATA CONDITIONAL PROBABILITY FUNCTION OF THE ENTIRE PROBLEM AND WHICH THANKS TO THE INVERSION PROVIDES PDF, MAP MODEL AND MODEL PARAMETERS UNCERTAINTIES. ....	78
FIGURE 2.2: BLOCK DIAGRAM OF THE ALGORITHM. THE FIGURE DESCRIBES THE BLOCK DIAGRAM OF THE ALGORITHM, WHICH STARTS WORKING AS SOON AS THE EARTHQUAKE LOCATION IS AVAILABLE, AND AN AZIMUTHAL COVERAGE CONDITION IS SATISFIED. THE PRELIMINARY DATA PROCESSING INCLUDES THE PARAMETERS MEASUREMENT, THE CORRECTION FOR DISTANCE, THE NORMALIZATION, AND LINEAR COMBINATION. THE FINAL SOLUTION IS DECLARED WHEN A CONVERGENCE CONDITION IS SATISFIED. PDF, PROBABILITY DENSITY FUNCTION; RT, REAL TIME. ....	80
FIGURE 3.1: RESULTS FOR THE MW 6.5 NORCIA EARTHQUAKE. (A) THE EPICENTRAL LOCATION OF SELECTED EARTHQUAKES OF SEQUENCE (DARK GRAY STARS) AND THE RECORDING STATIONS (LIGHT GRAY SQUARES). THE SIZE OF THE STARS IS PROPORTIONAL TO THE MAGNITUDE, AND THE MAIN EVENT IS REPRESENTED WITH A WHITE STAR. THE BLACK FOCAL MECHANISM PLOT REPRESENTS THE ISTITUTO NAZIONALE DI GEOFISICA E VULCANOLOGIA (INGV) CATALOG SOLUTION, AND THE GRAY ONE SHOWS OUR BEST SOLUTION. (B-E) THE SOLUTIONS OF STRIKE, DIP, AND SLIP AT EACH ITERATION, STARTING FROM ORIGIN TIME (O.T.). P.P. STAYS FOR PRINCIPAL PLANE, A.P. FOR AUXILIARY PLANE. DASHED LINES REPRESENT INGV CATALOG SOLUTIONS. DARK DOTS REPRESENT THE SOLUTIONS UP TO THE CONVERGENCE, AND GRAY DOTS REPRESENT THE SOLUTION	

EVOLUTION AFTER THE CONVERGENCE. ERROR BARS SHOW THE 68% CONFIDENCE ELLIPSOID PROJECTION ON EACH SOLUTION. (E) THE ROOT MEAN SQUARE (RMS) OF EACH SOLUTION (EMPTY SQUARES) AND THE CONVERGENCE CONDITION (WITH BLACK AND GRAY DOTS). INSET AT THE BOTTOM LEFT SHOWS A MAP OF ITALY WITH A EMPTY SQUARE INDICATING THE REGION IN EXAM, REPRESENTED IN THE BIGGER ARTWORK. .... 83

FIGURE 3.2: SUMMARY OF RESULTS FOR THE WHOLE SEQUENCE. THE TABLE REPORTS A SYNTHETIC DESCRIPTION OF THE RESULTS FOR ALL THE ANALYZED EARTHQUAKES. FROM LEFT TO RIGHT, THE COLUMNS CONTAIN REGION, MAGNITUDE, DATE, AND TIME OF EACH EVENT; INGV REFERENCE SOLUTION (STRIKE/DIP/SLIP); MAXIMUM A POSTERIORI PROBABILITY (MAP) MODEL IN A BAYESIAN APPROACH (STRIKE/DIP/SLIP); RMS OF FINAL SOLUTION; KAGAN'S ANGLE; TIME OF CONVERGENCE FROM ORIGIN TIME; NUMBER OF DATA; FOCAL MECHANISM PLOT REPRESENTATION OF THE BEST SOLUTION (RT) AND OF THE INGV REFERENCE SOLUTION. .... 84

FIGURE 3.3: THE SOLUTIONS OF STRIKE, DIP, AND SLIP AT EACH ITERATION, STARTING FROM ORIGIN TIME (O.T.). DASHED LINES REPRESENT INGV CATALOG SOLUTIONS. *P.P.* STAYS FOR PRINCIPAL PLANE, *A.P.* FOR AUXILIARY PLANE. DASHED LINES REPRESENT INGV CATALOG SOLUTIONS. DARK DOTS REPRESENT THE SOLUTIONS UP TO THE CONVERGENCE, AND GRAY DOTS REPRESENT THE SOLUTION EVOLUTION AFTER THE CONVERGENCE. ERROR BARS SHOW THE 68% CONFIDENCE ELLIPSOID PROJECTION ON EACH SOLUTION. TOP LEFT IT IS REPRESENTED THE STRIKE OF SOLUTION IN TIME, TOP RIGHT THE DIP AND BOTTOM LEFT THE SLIP. BOTTOM RIGHT IT IS REPRESENTED THE CONVERGENCE CONDITION (WITH BLACK AND GRAY DOTS). .... 86

FIGURE 3.4: HISTOGRAM OF MAGNITUDE EVENTS FOR THE ANALYSED NAGANO DATASET. .... 88

FIGURE 3.5: A) MAP OF THE REGION WITH BEACH BALLS IN BLACK FOR SOLUTIONS B) HISTOGRAM OF RMS ON AMPLITUDE FOR ALL SOLUTIONS C) HISTOGRAM OF MEAN KAGAN'S ANGLE OF SOLUTIONS IN THE POSTERIOR DENSITY FUNCTION RESPECT THE MAP MODEL OF EACH EVENT. .... 90

FIGURE 3.6: EXAMPLE: A) REPRESENTATION OF THE RESIDUAL BETWEEN OBSERVED AND PREDICTED AMPLITUDE AT THE AVAILABLE STATIONS; B) BEACH BALL FOR THE MOST LIKELY SOLUTION. BLACK AREAS ARE FOR POSITIVE POLARITIES AND WHITE REGIONS FOR NEGATIVE ONES. THE EMPTY CIRCLES CORRESPOND TO AUTOMATIC NEGATIVE POLARITIES; CROSSES ARE FOR AUTOMATIC POSITIVE POLARITIES. STATION NAMES ARE REPORTED IN RED. C) ON THE TOP-LEFT IT IS REPRESENTED THE RMS ON AMPLITUDE VERSUS THE KAGAN'S ANGLE, ON THE TOP-RIGHT IT IS REPRESENTED THE RMS ON AMPLITUDE VERSUS THE DIFFERENCE IN SLIP WITH RESPECT TO THE SLIP OF THE MOST LIKELY SOLUTION, ON THE BOTTOM-RIGHT THE RMS ON AMPLITUDE FOR THE DIFFERENCE BETWEEN DIP ANGLES AND THE 'BEST' DIP, AND ON THE BOTTOM-LEFT THE RMS ON AMPLITUDE FOR THE DIFFERENCE BETWEEN STRIKE AND THE 'BEST' STRIKE. .... 91

FIGURE 3.7: EVENTS WITH MANUAL PICKING: A) MAP OF ALL EVENTS, BLACK TRIANGLES REPRESENT STATIONS WHILE GREY STARS THE EVENTS AND EMPTY BOX REPRESENT WITH BLACK LINE REPRESENT REGION IN SECTION B; THE INSERT ON THE RIGHT TOP IS MAP OF ITALY, WITH A BLACK EMPTY BOX REPRESENTING THE STUDY AREA B) BEACH BALL RESULTS FOR EVENT IN STUDY, IN EACH BALL WHITE DOT REPRESENT T-AXES WHILE BLACK DOTS REPRESENT T-AXES. .... 93

FIGURE 3.8: SUMMARY RESULTS FOR REVISED EVENTS WITH MANUAL PICKING: A) T-PLUNGE VS P PLUNGE. GREY TONES REPRESENT BIN POPULATION (EACH BIN HAS SIZE 30°x30°).; B) POLAR HISTOGRAM FOR STRIKE ORIENTATION; C) HISTOGRAM FOR DIP; D) HISTOGRAM FOR SLIP; E) DOUBLE ARROWS REPRESENT THE ORIENTATION OF T-AXIS, THE MAP SECTION IS THE BOX DELIMITED IN FIGURE 1 A; E) POLAR HISTOGRAM OF T-AXIS ORIENTATION: LIGHT GREY FOR ALL EVENTS, ONLY THE PERCENTAGE IN DARK GREY IS A PURE NORMAL FAULT. .... 95

FIGURE 3.9: RESULTS FOR 2020-07-03 16:19:23 ML 3.0 EVENT WITH MANUAL PICKS: A) KAGAN'S ANGLES RESPECT MAP MODEL, THE COLOR IS RELATED TO THE PROBABILITY NORMALIZED ON THE MAP MODEL: ON THE TOP LEFT THE PROBABILITY NORMALIZED ON THE MAP MODEL PROBABILITY FOR DIFFERENT SOLUTIONS BELONGING TO THE POSTERIOR PDF, THE DASHED LINE REPRESENTS THE OUTER ENVELOPE OF THE KAGAN'S ANGLE DISTRIBUTION WITH RESPECT TO THE MAP MODEL; ON THE TOP RIGHT WE REPRESENT THE KAGAN'S ANGLE OF SOLUTIONS RESPECT THE MAP MODEL IN FUNCTION OF STRIKE, ON THE BOTTOM LEFT THE KAGAN'S ANGLE OF SOLUTIONS

RESPECT THE MAP MODEL IN FUNCTION OF DIP AND ON THE BOTTOM RIGHT THE KAGAN'S ANGLE OF SOLUTIONS RESPECT THE MAP MODEL IN FUNCTION OF THE SLIP; B) SECTIONS OF MARGINAL POSTERIOR PROBABILITY DENSITY FUNCTION WITH A GRAYSCALE CODED FROM WHITE TO BLACK (0 TO MAXIMUM OF MARGINAL POSTERIOR PROBABILITY). IN THE TOP IT IS THE SECTION STRIKE-SLIP, ON THE RIGHT THE SECTION DIP-SLIP, ON THE BOTTOM THE SECTION STRIKE-DIP; C) BEACH BALL OF THE MAP MODEL, EMPTY CIRCLE REPRESENTS A DOWN POLARITY, CROX REPRESENTS AN UP POLARITY. ....	96
FIGURE 3.10: AS IN FIGURE 3.9 BUT REPRESENTING RESULTS FOR 2020-07-03 19:46:21 ML 0.6 EVENT WITH MANUAL PICKS .....	97
FIGURE 3.11: EVENTS WITH AUTOMATIC PICKS: A) BLACK TRIANGLES REPRESENT STATION, GREY STARS THE EPICENTRAL LOCATIONS OF EVENTS, THE EMPTY BOX WITH BLACK BORDER REPRESENT THE AREA IN FIGURE B), THE INSERT ON THE RIGHT TOP IS MAP OF ITALY, WITH A BLACK EMPTY BOX REPRESENTING THE STUDY AREA; B) BEACH BALL FOR EVENTS AUTOMATICALLY DETECTED, WHITE DOT REPRESENT T-AXES WHILE BLACK DOT THE P-AXES.....	98
FIGURE 3.12: SUMMARY OF KAGAN'S ANGLES BETWEEN SOLUTIONS OBTAINED WITH MANUAL PICKING AND THOSE OBTAINED WITH AUTOMATIC PICKING; A) KAGAN'S ANGLE BETWEEN MAP MODEL OBTAINED WITH AUTOMATIC PICKING RESPECT MAP MODEL OBTAINED WITH MANUAL PICKING; B) MINIMUM KAGAN'S ANGLE BETWEEN MAP MODEL OBTAINED WITH MANUAL PICKING RESPECT ALL SOLUTIONS UNTIL 75% PROBABILITY RESPECT THE MAP MODEL OBTAINED WITH AUTOMATIC PICKING. ....	99
FIGURE 3.13: SUMMARY RESULTS FOR AUTOMATIC PICKS: A) ,B) , C) , D) AS IN FIGURE 3; E) ORIENTATION OF T-AXIS, BLACK DOUBLE ARROWS F) POLAR HISTOGRAM OF T-AXIS ORIENTATION: LIGHT GREY FOR ALL EVENTS, ONLY THE PERCENTAGE IN DARK GREY IS A PURE NORMAL FAULT. ....	100
FIGURE 3.14: AS IN FIGURE 3.9 BUT REPRESENTING RESULTS FOR 2020-07-03 16:19:23 ML 3.0 EVENT WITH AUTOMATIC PICKS.....	101
FIGURE 3.15: AS IN FIGURE 3.9 BUT REPRESENTING RESULTS 2020-07-05 14:14:04 ML 1.2 EVENT WITH AUTOMATIC PICKS.....	101
FIGURE 4.1 (A) SIMPLIFIED LOW FREQUENCY GAUSSIAN SLIP DISTRIBUTION CENTERED IN THE MIDDLE OF THE FAULT. (B-C-D) LOG-NORMAL DISTRIBUTION OF THE PARAMETER ROUGHNESS K, UNIFORM DISTRIBUTION OF RUPTURE VELOCITY AND UNIFORM DISTRIBUTION OF THE MAXIMUM SLIP WITH RESPECT TO THE CENTER OF THE FAULT RESPECTIVELY. THIS VARIABILITY LEADS TO THE DEFINITION OF 1500 STOCHASTIC SLIP DISTRIBUTIONS AS THAT ONE SHOWED IN THE PANEL (E). THE SLIP DISTRIBUTIONS ARE PLACE ON A FAULT HAVING A DOUBLE LENGTH WITH RESPECT TO L. (F) FROM EACH SIMULATIONS THE PGV IS DIRECTLY EXTRACTED FROM THE HORIZONTAL COMPONENTS OF THE SYNTHETIC SEISMOGRAMS .....	107
FIGURE 4.2: SCHEME OF THE $k^2$ MODELLING OF THE SOURCE: ON THE TOP THE GAUSSIAN LOW-FREQUENCY DISTRIBUTION, IN THE MIDDLE THE STOCHASTIC DISTRIBUTION OF THE SHORTER WAVELENGTH SLIP ASPERITIES, ON THE BOTTOM THE FINAL MODEL AS THE SUMMATION OF THE LOW AND HIGH-FREQUENCY DESCRIPTIONS. (B) PROJECTION ONTO THE EARTH'S SURFACE OF THE FAULT PLANE USED IN THE FORWARD MODEL. ON THE FAULT PROJECTION THE SLIP DISTRIBUTION IS PLOTTED. THE RED DOT AND THE GREEN TRIANGLES REPRESENT THE EPICENTER AND THE USED STATIONS RESPECTIVELY. THE TEXTS REFER TO THE STATIONS WHOSE SYNTHETIC TRACES ARE PLOTTED IN THE PANELS (C) AND (D). (E-F): THE AMPLITUDE DISPLACEMENT SPECTRA FOR THE SAME STATIONS OF PANEL (C) AND (D). THE SPECTRA ARE INVERTED THROUGH A CLASSICAL $F^{-2}$ FIT (BLACK DASHED LINES) AND THE CORNER FREQUENCIES ARE EXTRACTED (BLUE DASHED LINES). ....	108
FIGURE 4.3: STUDY OF STABILITY OF THE FINAL SLIP VALUE VARYING THE THRESHOLD OF RADIATION PATTERN. THE BLUE ARROW INDICATES THE THRESHOLD EQUAL TO 0.01. ....	109
FIGURE 4.4: RESULTS OF BACK-PROJECTION BACK-PROJECTING THE SYNTHETIC DATA FROM ALL THE STATIONS WITHIN THE RANGE [15-45 KM] AND IN THE FREQUENCY BAND [0.15-0.50 Hz] : A) MAP: EPICENTER IS REPRESENTED AS A RED STAR, STATIONS ARE REPRESENTED AS TRIANGLES, BLACK TRIANGLES ARE STATIONS WITHIN (15-45) KM, WHITE TRIANGLES ARE OUTSIDE OF THIS RANGE; B) DISPLACEMENT WINDOWS FOR STATIONS ORDERED IN	

GROWING DISTANCE; C) WINDOWS READY FOR THE STACKING AFTER TIME SHIFT RESPECT THE REFERENCE STATION, ORDERED IN GROWING DISTANCE (AS IN B) WITH CORRESPONDING STATIONS NAMES; D) ON TOP THE "TRUE" SLIP MAP, ON THE BOTTOM INTERPOLATED SLIP MAP FOUND BY BACK-PROJECTION, FOR BOTH TOP AND BOTTOM THE WHITE STAR REPRESENTS THE HYPOCENTER AND COLORS ARE FOR THE VALUES OF SLIP (M). THE WHITE LINES IN THE BOTTOM ARE CONTOUR LINES OF "TRUE" MODEL FOR VALUE EQUAL TO 1 AND 2.5 M OF SLIP RESPECTIVELY.....	111
FIGURE 4.5: RESULTS OF BACK-PROJECTION BACK-PROJECTING THE SYNTHETIC DATA FROM ALL THE STATIONS WITHIN THE RANGE [15-45 KM] AND IN THE FREQUENCY BAND [0.5-2.0 Hz] A) MAP: EPICENTER IS REPRESENTED AS A RED STAR, STATIONS ARE REPRESENTED AS TRIANGLES, BLACK TRIANGLES ARE STATIONS WITHIN (15-45) KM , WHITE TRIANGLES ARE OUTSIDE OF THIS RANGE; B) DISPLACEMENT WINDOWS FOR STATIONS ORDERED IN GROWING DISTANCE; C) WINDOWS READY FOR THE STACKING AFTER TIME SHIFT RESPECT THE REFERENCE STATION, ORDERED IN GROWING DISTANCE (AS IN B) WITH CORRESPONDING STATIONS NAMES; D) ON TOP THE "TRUE" SLIP MAP, ON THE BOTTOM INTERPOLATED SLIP MAP FOUND BY BACK-PROJECTION, FOR BOTH TOP AND BOTTOM THE WHITE STAR REPRESENTS THE HYPOCENTER AND COLORS ARE FOR THE VALUES OF SLIP (M). THE WHITE LINES IN THE BOTTOM ARE CONTOUR LINES OF "TRUE" MODEL FOR VALUE EQUAL TO 1 AND 2.5 M OF SLIP RESPECTIVELY.....	113
FIGURE 4.6: RESULTS OF BACK-PROJECTION BACK-PROJECTING THE SYNTHETIC DATA FROM NORTH STATIONS IN THE FREQUENCY BAND [0.15-0.5 Hz] A) MAP: EPICENTER IS REPRESENTED AS A RED STAR, STATIONS ARE REPRESENTED AS TRIANGLES, BLACK TRIANGLES ARE STATIONS IN THE NORTH SIDE OF THE HYPOCENTER, WHITE TRIANGLES ARE OUTSIDE THIS SELECTION; B) DISPLACEMENT WINDOWS FOR STATIONS ORDERED IN GROWING DISTANCE; C) WINDOWS READY FOR THE STACKING AFTER TIME SHIFT RESPECT THE REFERENCE STATION, ORDERED IN GROWING DISTANCE (AS IN B) WITH CORRESPONDING STATIONS NAMES; D) ON TOP THE "TRUE" SLIP MAP, ON THE BOTTOM INTERPOLATED SLIP MAP FOUND BY BACK-PROJECTION, FOR BOTH TOP AND BOTTOM THE WHITE STAR REPRESENTS THE HYPOCENTER AND COLORS ARE FOR THE VALUES OF SLIP (M). THE WHITE LINES IN THE BOTTOM ARE ISOLINES OF "TRUE" MODEL FOR 1 AND 2.5 M OF SLIP RESPECTIVELY.....	114
FIGURE 4.7: RESULTS OF BACK-PROJECTION BACK-PROJECTING THE SYNTHETIC DATA FROM NORTH STATIONS IN THE FREQUENCY BAND [0.5-2 Hz] A) MAP: EPICENTER IS REPRESENTED AS A RED STAR, STATIONS ARE REPRESENTED AS TRIANGLES, BLACK TRIANGLES ARE STATIONS IN THE NORTH SIDE OF THE HYPOCENTER, WHITE TRIANGLES ARE OUTSIDE THIS SELECTION; B) DISPLACEMENT WINDOWS FOR STATIONS ORDERED IN GROWING DISTANCE; C) WINDOWS READY FOR THE STACKING AFTER TIME SHIFT RESPECT THE REFERENCE STATION, ORDERED IN GROWING DISTANCE (AS IN B) WITH CORRESPONDING STATIONS NAMES; D) ON TOP THE "TRUE" SLIP MAP, ON THE BOTTOM INTERPOLATED SLIP MAP FOUND BY BACK-PROJECTION, FOR BOTH TOP AND BOTTOM THE WHITE STAR REPRESENTS THE HYPOCENTER AND COLORS ARE FOR THE VALUES OF SLIP (M). THE WHITE LINES IN THE BOTTOM ARE CONTOUR LINES OF $k^{-2}$ CONTRIBUTION OF "TRUE" MODEL FOR 0.25 AND 0.5 M OF SLIP RESPECTIVELY.	115
FIGURE 4.8: RUPTURE VELOCITY: A) ACTIVATION TIME IN COLOR ON THE FAULT OF THE SUB-SOURCES THAT HAVE DISLOCATED, THE WHITE STAR REPRESENTS THE HYPOCENTER, THE WHITE LINE JOINS THE POINTS ON THE PLANE TO WHICH CORRESPOND THE MAXIMUM SLIP RATE OVER TIME; B) DISTANCE VS TIME CORRESPONDING TO THE SUB-SOURCE WITH MAXIMUM SLIP RAT. RED LINE REPRESENTS THE FIT, OF WHICH THE SLOPE GIVES A RUPTURE VELOCITY OF $2.4 \pm 0.3$ KM/S. ....	116
FIGURE 4.9: APPLICATION TO REAL DATA OF THE 2016, Mw 6.5 NORCIA EARTHQUAKE: A) STATIONS ARE REPRESENTED AS WHITE TRINAGLES,THE RED STAR REPRESENT THE EPICENTER, VALUES OF FINAL SLIP RETRIEVED ON THE FAULT PLANE INVESTIGATED ARE PLOTTED IN COLOR (M). ....	117
FIGURE 4.10: 6.5 Mw, 2016, NORCIA EARTHQUAKE: SLIP RATE (M/S) IN THE TIME ON THE FAULT PLANE.....	118
FIGURE 4.11: MAP OF ANALYSED EARTHQUAKES WITH THE MULTI ARRAY BACK PROJECTION.....	121
FIGURE 4.12: THE CASE STUDY OF THE 2015 Mw 8.3 ILLAPEL EARTHQUAKE: A) THE CIRCLES ARE BACK-PROJECTION RADIATORS COLOR-CODED BY TIME AND SIZED BY THE NORMALIZED POWER. THE RED STAR IS THE EPICENTER AND	

BLUE SQUARES ARE STRONG MOTION STATIONS. THE TILES ARE THE SLIP DISTRIBUTION ESTIMATED BY AN & MENG, 2017; b) RMSE OF PSA VS PERIOD COMPUTED FOR STATIONS DISTANCE FROM LOW-FREQUENCY RADIATORS AS OBTAINED IN THIS WORK (BLUE CROSSES), FROM HIGH-FREQUENCY RADIATORS BY MENG ET AL. 2018 (RED CIRCLES) AND FOR JOYNER-BOORE DISTANCE CONSIDERING THE SLIP MODEL OF AN & MENG, 2017 (BLACK SQUARES); c), d), e) WHITE TALES REPRESENT THE FAULT AND THE RED STAR REPRESENTS THE EPICENTER, IN c) THE GREY CIRCLES REPRESENT THE 80% STRONGEST HIGH-FREQUENCY RADIATORS BY MENG ET AL. 2018 WHILE THE STATIONS ARE REPRESENTED AS CIRCLES COLOR-CODED BY THE RESIDUAL BETWEEN THE OBSERVED PGA AND THE PREDICTION BASED ON THIS RADIATORS; IN d) THE GRAY TILES REPRESENT FAULT PORTION WHOSE DISLOCATION EXCEED THE 20% OF THE MAXIMUM OF THE SLIP (AN & MENG, 2017), WHILE THE STATIONS ARE THE CIRCLES COLOR-CODED BY THE RESIDUAL BETWEEN THE OBSERVED PGA AND THE PREDICTION BASED ON TRUNCATED JOYNER-BOORE DISTANCE CONSIDERING THE SLIP MODEL OF AN & MENG, 2017); IN e) GRAY CIRCLES REPRESENT THE 80% STRONGEST LOW-FREQUENCY RADIATORS OBTAINED IN THIS WORK (AS IN A) OF THIS FIGURE) AND THE STATIONS ARE THE CIRCLES COLOR-CODED BY THE RESIDUAL BETWEEN THE OBSERVED PGA AND THE PREDICTION BASED ON THE LOW-FREQUENCY RADIATORS. .... 124

FIGURE 4.13: THE CASE STUDY OF THE 2010 Mw 7.2 EL MAYOR CUCAPAH EARTHQUAKE: a) THE RED STAR IS THE EPICENTER AND SQUARES ARE STRONG MOTION STATIONS, EACH COLOUR IS FOR DIFFERENT CLUSTERS, WHILE THE LINE FAULT IS BY MENDOZA ET AL, 2013. b) THE CIRCLES ARE BACK-PROJECTION RADIATORS COLOR-CODED BY TIME AND SIZED BY THE NORMALIZED POWER. THE RED STAR IS THE EPICENTER AND THE BLACK DASHED LINE REPRESENTS THE TRACE OF FAULT AS IN MENDOZA ET AL, 2013. THE TILES ARE THE SLIP DISTRIBUTION ESTIMATED BY WEI ET AL, 2011 ; c) IN THE BACKGROUND THERE IS THE PREDICTION OF PGV (CM/S), THE RED STAR IS THE EPICENTER, THE BLACK LINE IS THE THE LINE FAULT BY MENDOZA ET AL., (2013), WHILE THE TRIANGLES REPRESENT STATIONS COLOR-CODED FOR THE OBSERVED PEAK ABSOLUTE VELOCITY; d) RMSE OF PSA VS PERIOD COMPUTED FOR STATIONS IN c) CONSIDERING DISTANCE FROM RADIATORS (BLACK SQUARES) AND WITH JOYNER-BOORE DISTANCE FOR THE MENDOZA ET AL., (2013) MODEL (MAGENTA CROSSES) AND WEI ET AL (2011) MODEL (BLUE CIRCLES). .... 125

FIGURE 4.14: THE CASE STUDY OF THE 2016 Mw 6.5 NORCIA EARTHQUAKE: a) IN THE BACKGROUND THERE IS THE PREDICTION OF PGA (CM/S<sup>2</sup>), THE RED STAR IS THE EPICENTER, THE DASHED BLACK LINES ARE CONTOUR LEVELS, THE BLACK LINE IS THE EDGE OF THE PROJECTED FAULT, WHILE THE TRIANGLES REPRESENT THE STATIONS USED IN THE BP AND THEIR COLOR REPRESENT THE OBSERVED PEAK ABSOLUTE ACCELERATION b) THE CIRCLES ARE BACK-PROJECTION RADIATORS COLOR-CODED BY TIME AND SIZED BY THE NORMALIZED POWER. THE RED STAR IS THE EPICENTER AND BLUE SQUARES ARE STRONG MOTION STATIONS. THE TILES ARE THE SLIP DISTRIBUTION ESTIMATED BY PIZZI ET AL, 2017; c) RMSE OF PSA VS PERIOD IN THE RANGE 0.02-3 S COMPUTED FOR ALL STATIONS WITHIN 200 KM OF JOYNER-BOORE DISTANCE, BLACK CROSSES ARE FOR DISTANCE FROM RADIATORS WHILE BLU CROSSES ARE FOR JOYNER-BOORE DISTANCE; d) THE SAME AS IN C, BUT FOR DISTANCE WITHIN 70 KM. .... 128

FIGURE 4.15: CASE STUDY ITALY, STATIONS NAMES AT THE CLUSTER AT SOUTH RESPECT HYPOCENTER: COLOR REPRESENTS AVAILABLE TIME IN SECONDS BETWEEN THE LAST UPDATED PREDICTION (THANKS TO THE USE OF THE DISTANCE BETWEEN THE STATION AND RADIATORS IN THE GMPE OF BINDI ET AL, 2014) AND OCCURRENCE OF THE OBSERVED MAXIMUM PEAK GROUND ACCELERATION. .... 130

FIGURE 4.16: CASE STUDY ITALY, STATIONS AT THE CLUSTER AT SOUTH RESPECT HYPOCENTER: RED LINES REPRESENT OBSERVED ABSOLUTE PEAK ACCELERATION AT EACH STATION, BLACK CROSSES REPRESENT THE PREDICTED PEAK ACCELERATION AT EACH 0.5 S IN AN EVOLUTIONARY APPROACH, GREEN PATCH IS THE UNCERTAINTY ON THE PREDICTION IN THE GMPE OF BINDI ET AL, 2014. STATIONS LOCATION ARE PLOTTED IN FIG. 4.13. .... 131

FIGURE 5.1: SCHEMATIC DESCRIPTION OF SOME OF AN IDEAL PROCESSING OF DATA WHEN AN EARTHQUAKE OCCURRS. (TOP) AT THE OCCURRENCE OF AN EVENT, MOVING ON THE TIMELINE IN THE P-WAVES TIME WINDOW FAST ESTIMATES OF THE HYPOCENTER, MAGNITUDE AND FAULT GEOMETRY ARE COMPUTED. DURING THE RECORDING OF THE S-WAVE PHASE, THE REAL PGA ESTIMATES BECOMES AVAILABLE. THE S-WAVES RECORDING ALONG WITH

THE PREVIOUS ESTIMATES ARE HENCE USED TO COMPUTE REFINED SOURCE MODELS WITH COMPLEMENTARY APPROACHES. FINALLY, THESE MODELS CAN BE USED TO COMPUTE REFINED SYNTHETIC SEISMOGRAMS AND THE FINAL SHAKE MAPS. (BOTTOM) THE DEFINITION OF A REFINED SOURCE MODEL IS EXPECTED TO REDUCE THE UNCERTAINTY ON THE PGX ESTIMATES FEW MINUTES AFTER THE END OF THE EVENT. ....136

# INTRODUCTION

Scientific and technological progress go hand in hand and feed on each other. The improvement of the instruments, as well as the new inventions, can validate theoretical models which try to explain physical processes. Just as an example, the early seismographic instruments measured only the vertical component of the ground motion. An incredible quantity of knowledge is surely evaluable along just this dimension. However, only thanks to the advent of 3-component seismographs, which were able to measure the horizontal components of the ground motion, it was possible to validate the double-couple source model with which seismic point sources are modeled. As we will describe later, for a point source the P-wave radiation pattern, which modulates the first seismic wave amplitudes in the space, is completely equivalent for a single couple of forces and a double couple of forces, but it is not the same for the S-wave radiation pattern. Today we know that the mechanisms of fracturing of the rocks, that give rise to the seismic waves, can therefore be reasonably modeled with a double couple for a point source in an elastic medium for reasons of moment balance and that it is also clearly confirmed by the observations.

As we will see in detail, the response behaviour of the medium for the seismic events' duration is of an elastic kind and the waves that propagate within it produce the effect of ground shaking that is that recorded by the seismograms.

Of course, there are more reasons why the rocks fracture, one of interest is the seismotectonic loading, which in special areas can cause moderate to large earthquakes. These target seismic events can produce severe damages and have shaped, during the time, firstly the imagination and then the story of entire countries.

Thought the ground shaking, often indicated wrongly as guilty of fatality, is, indeed, as we will see in the next chapters, an essential witness to be questioned to obtain information about the rupture process, site soil conditions, path characteristics since it is the result of the convolution of source function, site effect, instrument response and Green function which describes the ray path from source to site.

Nowadays in economically developed countries, the buildings hit by shaking can survive to collapse if built according to regulations. In such a case, different garrisons can still improve and safeguard life. It is in this perspective that earthquake early warning systems have been implemented by exploiting the difference in travel time between the first P waves, faster and carrying on information about the source, and the slower S and superficial waves, which cause greater damages. These systems can still improve the quality of resilience of production activities affected by an earthquake, allowing to stop machinery operations and automatically guarantee the safety of workers and delicate instruments. In the perspective of improving and integrating these systems, which were initially designed to provide location information and expected intensity measures at a target site in a simple way and for rapid response after the event, we firstly developed a quick algorithm to provide focal mechanism estimation, that can improve, together with length and width fault dimensions, the forecasting intensity measures modeling a finite dimensions source rather than model a point source. To infer the focal mechanism, we set up an evolutionary Bayesian approach based on the comparison of P-wave peak amplitude considering the real streaming of data and increasing time window. This quantity, opportunely corrected for the distance attenuation, reflects the geometrical radiation pattern in the space of the P-wave. We tested this methodology on the Central Italy seismic sequence (2016-2017) with a magnitude range  $M_w$  4.8-6.5. We obtained in few seconds within origin time solutions consistent with reference. Furthermore, the use of Bayesian theory allows to get probability distributions for solutions and to estimate uncertainties associated with their maximum probability estimations.

Several techniques for the focal mechanism estimation, suitable for a specific magnitude range, have been proposed and are being used at the worldwide seismic observatories. The most general approach for the determination of the focal mechanism is the computation of the moment tensor, which provides unique and robust information regarding the fault plane orientations and the size of the event. For moderate to large earthquakes, the moment tensor is usually obtained from the full waveforms modeling of far-field seismic records (Dreger and Helmberger, 1993; Dreger, 2003, Sokos and Zahradník, 2008) or spectral data inversions (Delouis, 2014). However, these methods involve the complexity of modeling the entire waveforms and are time-consuming, moreover, they

require observations enough far from the source, which means to provide results that are not timely, excluding the possibility of issuing near real-time estimations

In the framework of the EU H2020 project “Seismology and Earthquake Engineering Research Infrastructure Alliance for Europe (SERA)”, different methodologies are being developed and tested, with the final goal of generating time-evolutionary ground-shaking maps, accounting for a reliable finite-fault model of the earthquake and rupture kinematic description (the finite-fault rupture detector algorithm for the determination of fast and robust line-source models of large earthquakes; Böse et al., 2012; fast detection of rupture directivity and preliminary estimations of rupture length and rupture duration; Cesca et al., 2011). Within this context, we developed this straightforward methodology to quickly and automatically estimate the focal mechanism of earthquakes (Tarantino et al, 2019), starting from the azimuthal distribution of the early P-wave peak in displacement, velocity, and acceleration (Pd, Pv, and Pa, respectively; Colombelli et al., 2012; Carranza Gómez, 2016).

We then investigated potential applications of this new algorithm on lower magnitude earthquakes, applying it on a dataset of microearthquakes that occurred in Nagano (Japan, 2011 with magnitude  $M_v^*$  -1 to 2.6), in an offline approach and using automatic picks.

In the case of micro-seismicity, providing a focal mechanism (strike, dip and slip angles of the principal and auxiliary fault planes) is a challenging issue. A classical and very popular method, such as FPFIT software package (Reasenberg and Oppenheimer, 1985) requires the exclusive use of P-wave polarities. FPFIT works on a grid search over all possible values of the model parameters (strike, dip and slip) to find the best-fitting focal mechanism. The misfit associated with a retrieved solution is given by the number of polarity observations that mismatch with the predicted polarity, weighted by the quality of the observation and the distance from the nodal planes. Confidence intervals for each model parameter are determined by finding

\*The Japan Meteorological Agency (<https://www.jma.go.jp/jma/indexe.html>) characterizes the recorded seismicity with a velocity magnitude ( $M_{JMA}$ ), determined from the maximum amplitude of velocity seismograms (Funasaki et al. 2004).  $M_v$  is a velocity magnitude law according to a linear regression between the maximum horizontal amplitudes measured in velocity at selected seismic stations and JMA catalog data.

how much each parameter may change without exceeding a critical misfit level computed from the observed data misfit, so that, in case of multiple solutions, the solutions with lower misfit are those best constrained from available data. However, there is a limitation on the minimum number of stations (needful at least 6 polarities) and it is not always so easy to distinguish the sign of polarity for a not impulsive phase in case of low magnitude events, as well as to reliably project the polarity on the focal sphere.

Another approach consists of the joint use of P polarities and S-wave polarization in a Bayesian setting (Zollo and Bernard, 1991). P-wave polarity dataset could be not sufficient to constrain into a single solution the focal mechanism of earthquakes recorded by a local network, because of the small number of available stations and their generally poor azimuthal coverage around the source. The complementary information carried by S-wave polarization improves the resolution of the fault model thanks to the different radiation pattern of S-wave compared to the one related to P-waves. This tool shows to be useful and stable for the study of near-source records, in fact S-wave polarizations is less affected by propagation effects compared with the amplitudes, but its precise measuring can be difficult in cases of noisy records and low signal-to-noise ratio, that is the case for very low magnitude seismicity.

The techniques designed to work for moderate-to-large earthquakes waveforms or spectral data (Dreger and Helmberer,1993; Dreger,2003; Delouis, 2014; Fojtiková and Zahradík,2014) cannot be easily applied to small earthquakes due to the higher noise level and to the inadequate description of the medium response at the wavelengths at which low magnitude earthquakes radiate.

In 2002 Hardebeck and Shearer introduced a new method for constraining focal mechanism taking into accounts the possibility of errors in the computed take-off angles. They considered multiple combinations of reasonable source depths and one-dimensional velocity models. The solution is given as the average of the set of acceptable mechanisms and the uncertainty is represented by its distribution. Later, Hardebeck and Shearer (2003) showed that the observed S/P waves amplitudes ratio is consistent with the expected focal mechanism, implying that it can be useful to better constrain the focal mechanism of small earthquakes. This ratio allows neglecting both the magnitude and geometrical attenuation.

Later, De Matteis et al. (2016) made use of the ratio between P-wave and S-wave spectra jointly with polarities, correcting the data for the ratio of S and P waves velocities, allows to obtain reliable estimation for focal mechanism. Their approach does not require very high precise identification of the first arrival, it is sufficient that the portion of the seismogram used for the spectral inversion contains only the necessary seismic body phase. This methodology can work to both small and moderate-to-large magnitude earthquakes; it was applied to three earthquakes of respectively magnitude 2.9 MI, 4.1 MI and 5 Mw showing good agreement with reference solutions and more constrained solutions respect those obtained with the only use of first motion polarity.

To infer the focal mechanism of small events (M 3.4- 3.7), Zahradnik et al. (2001) used the comparison of amplitude spectra of the whole recorded signal and the one computed from synthetic signals based on different sets of focal mechanism and different value of the scalar seismic moment and centroid, finally the polarities are used to accept or reject the obtained solutions. The performance of this method runs into the challenging key aspects associated with the setting up of synthetic seismograms, which means it depends on the level of knowledge about the propagation medium and on the capability to simulate the high-frequency content of real earthquakes, moreover the use of complete records requires to exclude station with strong site-effects. The tool works on broadband stations, which suffers systematically from event-induced instabilities at horizontal components if earthquakes occurred at short distances, 10-30 km, and this method could not be easily applied for frequencies below 0.1 Hz. For this reason, the results are sensitive concerning unknown crustal structure details and the focal mechanism remains rather uncertain, however this latter issue is a common problem to also other methods that could map structural uncertainties and complexities into the focal mechanism, retrieving not the exactly true model.

Recently, Petersen et al. (2021) used in a Bayesian bootstrap-based probabilistic joint inversion scheme a combination of time-domain full waveforms and frequency domain amplitude spectra as input data for the centroid Moment tensor inference for earthquakes with  $M_w \geq 3$  that occurred in the Alps and recorded at temporary broadband stations. They optimized the used methods and combined different input data types to attempt to lower the magnitude threshold for inversions compared to

routinely reported solutions. They retrieved that for most earthquakes with magnitudes larger than Mw 3.3 a combination of time-domain full waveforms and frequency domain amplitude spectra in a frequency band of 0.02-0.07 Hz is most suitable. In case of small events, large gaps in the azimuthal station distribution can hinder successful inversions or may lead to biased results. In contrast, under favorable geometric conditions, when strike direction and tensional as well as compressional quadrants are adequately covered, inversions are possible even for small events using only a few stations.

Later, thanks to the Bayesian framework of our approach, we integrated the use of further independent datasets, such as polarity and S-wave to P-wave amplitude (S/P) ratio datasets, which methodology is illustrated in the Chapter 2. The inclusion of more data allows to better constrain the solutions as in the case of manual picking. Of course, this formulation allows working even if in absence of one dataset. The use of 3 different independent datasets contributes to expanding the range of magnitude toward its lower limit (until 0.4 MI as shown in the applications) and allows to better constrain the solution thanks to the increasing of data, which can be very poor in case of very small events. Moreover, the use of even just one polarity allows us to solve the ambiguity on the slip sign. The advantage of this approach is that it can still work also with only the use of polarities and P-wave amplitudes, which can be performed automatically by monitoring systems, revealing its potential use for automatic platforms. This allows this method to be extremely versatile and to be able to work in the presence of an operator but also in the absence of a manual reviewer, in a completely automatic setting. This versatility is the strong point of this algorithm that can work in different modes, but also for different ranges of magnitudes with an adequate tuning of the observation time windows to guarantee to observe the full duration of the source time function. As soon as an event is located and magnitude is estimated, we could select a proper time window in which estimated the P-wave peak amplitude since the arrival time at the station.

We applied this new setup to a sequence that occurred in Irpinia in 2020 (MI 0.4-3.0), in the southern Apennines, both with manual and automatic picking, the latter performed by a monitoring automatic system active on the area (Satriano, 2010, <http://www.prestoews.org/>). We then analyzed the dominant nature of the focal mechanism in the area and inferred the

orientation of the stress tensor, obtaining promising results that encourage us to use it to further investigate the behavior of microearthquakes. In fact, despite the low magnitude of the analyzed events, fault plane solutions reflect a tectonic regime consistent with the regional stress field. We tested the new setup also on the mainshock of the central Italy sequence, using P-wave amplitudes ratios and available polarities.

Then we deepened in techniques to imagine the rupture process. We followed two different approaches. Firstly, we applied a technique (Maercklin et al., 2012) able to retrieve of slip images from the Back-Projection (BP) of displacement records. This technique is based on the discretization in sub-panels of a plane oriented according to the fault plane, on which to back-project the beamformed and stacked amplitude displacements, taking into accounts for distance attenuation and geometrical factors due to focal mechanism. This allows for retrieving the final slip map directly on the fault. Later, we approached a technique of Multi-Array BP (Xie and Meng, 2020) that works on merging the results of different clusters of stations to retrieve the location of seismic radiators, that are regarded as the centroid locations of seismic sub-events at different stages during an earthquake and which contribute to the generation of the ground shaking at a site target. We applied to moderate to large events at local and regional distances to retrieve seismic radiators in the time. The location of seismic radiators is useful to infer the length of main rupture. Moreover, it has been demonstrated that it is possible to use the distance from seismic radiators to stations instead of the truncated Joyner-Boore distance (Boore and Joyner, 1982) in the Ground Motion Prediction Equations for teleseismic distances (Feng and Meng, 2018). We used also in regional and local scale the distance of the stations from the nearest seismic radiator as a metric distance in local Ground Motion Prediction Equations, overpassing assumptions on the faults and on the kinematic models. Finally, we tried to see potential benefits of predicting the final intensity measures in an evolutionary approach in which as new seismic radiators have been located, the ground shaking intensity estimate is updated.

We will describe in the first chapter of this thesis the seismic source concepts useful for the treatment, the earthquakes early warning systems, their classifications, their operational setting, and the next generation of

systems, then we will describe BP techniques, besides, we will handle the theory which inverse methods are based on. In the second chapter we will illustrate the methodology to estimate the focal mechanism and its general possible set-ups. We then will show in a dedicated chapter the different applications for focal mechanism estimation, such as in near-real-time for moderate events and in an offline configuration to study micro-seismicity. Then we will show applications of the two different approaches for BP. We will devote the final part of this thesis to conclusions.

# 1 THEORY FRAMEWORK

---

## 1.1 THE SEISMIC SOURCE

During the process of an earthquake, if we look outside the damaged zone, the Earth system behaves as a linear and stationary filter and the seismogram registered at the surface is the output of a Linear and Time Invariant filters chain which modifies the shape and the amplitude of the source-function signal. In fact, the seismogram is the convolution of the source function, which we consider as input of our filter chain, the propagation term, which is related to the contribution of the medium in which waves propagates inside, and instrumental response. This latter term is easily deconvolved because it is known from the calibration of the instrument and in our discussion, we will omit it. The ground displacement recorded at the Earth surface at the position  $\mathbf{x}$  by a receiver and deconvolved for instrumental response is given by:

$$u(\mathbf{x}, t) = s(\boldsymbol{\xi}, t) * G(\mathbf{x}, \boldsymbol{\xi}, t) \quad 1.1$$

where  $\boldsymbol{\xi}$  is the source location,  $s(\boldsymbol{\xi}, t)$  is the source time function and  $G(\mathbf{x}, \boldsymbol{\xi}, t)$  the propagation term representing the impulse response of the medium.

Earthquake ruptures are generated by the relative motion of crustal blocks, which occurs along fault surfaces embedded in the shallower Earth fragile layer. There is a complex energy balance between the dissipation occurring along the fault and in the surrounding volume, and the radiated field, which is represented by the seismic waves propagating away from the source and that produce the ground motion displacement measured by the seismometers.

A fault is a surface that divides two parts of material, inside a volume. We can assume that the fault zone is an infinitely thin surface where the different dissipation mechanisms occurring during the rupture are homogenized, in fact we know from observation that the thickness of a fault is much smaller (tens to few hundreds of meters) than the wavelengths at which we observe the rupture process. During the dislocation process, the first point on the fault plane which

dislocates and emits energy as seismic waves is defined as the hypocenter. From this point the fracture propagates on the whole fault.

If  $\lambda$  is the wavelength of the observed signal,  $r$  is the source-to-receiver distance, and  $L$  is the length of the fault, we have three different cases:

- Condition of extended source and high-frequency approximation

$$L \approx r \gg \lambda$$

- Condition of high-frequency and Fraunhofer approximation

$$\lambda \ll r \gg L$$

- Condition of point source at high-frequency:

$$L \ll \lambda \ll r$$

In high-frequency approximation, we can simplify Green's function description taking into account only the *far-field* terms.

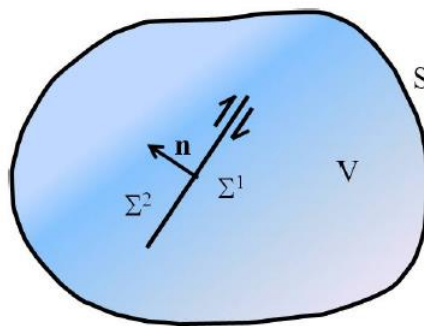


Figure 1.1: A seismic fault is here represented as a surface inside a volume  $V$  along which slip occurs. The two lips of the fault are separated to interpret the displacement discontinuity across such a surface, figure from Festa and Zollo,2006

Let us consider a volume  $V$  internal to the Earth, bounded by the surface  $S = \partial V$  inside which the linear elastodynamics hold and assume homogeneous boundary conditions on  $S$ , except for the fault surface  $\Sigma$ , along which slip occurs. We indicate

with  $\Sigma_1$  and  $\Sigma_2$  the two lips of the fault which move away from each other, and we define the normal  $\mathbf{n}$  to the fault as the normal to  $\Sigma_1$  entering  $\Sigma_2$  (Fig. 1.1) We refer all quantities on the fault to a reference configuration defined at the initial time equal to zero, such as when the two lips on the fault are at their original position. We can assume as reasonable the small-strain approximation since the amount of slip is small (centimetres to meters) compared to the size of the process zone (tens to few hundreds of meters). Because of the slippage, the displacement and its time derivative are discontinuous across the surface  $\Sigma$ . We define the slip function as the difference of the Lagrangian displacement  $\mathbf{u}$  across the two sides of the fault surface  $\delta\mathbf{u} = \mathbf{u}_1 - \mathbf{u}_2$ . We have that for spontaneous ruptures traction must be continuous across the fault surface  $\Sigma$ . Thanks to Betti's theorem, we can write the displacement seismogram observed at a location  $\mathbf{x}$  inside the Earth or at its surface can be computed as the convolution of the slip function with the elastic response of the propagation medium:

$$u_m(\mathbf{x}, t) = \int_{-\infty}^{+\infty} d\tau \int_{\Sigma} \delta u_i(\xi, \tau) c_{ijkl} n_j \frac{\partial G_{mk}}{\partial \xi_l}(\mathbf{x}, t - \tau, \xi) d\xi$$

that is in another form of the equation (1.1). The  $\mathbf{c}$  is the elastic coefficients tensor and is symmetric with respect to the exchange of all indices. For a general elastic solid it has 21 independent components, but for an isotropic medium there are only two independent coefficients, that are the Lamé constants  $\lambda$  and  $\mu$ :  $c_{ijkl} = \lambda \delta_{ij} \delta_{kl} + \mu(\delta_{ik} \delta_{jl} + \delta_{il} \delta_{jk})$ . As we explained for equation (1.1),  $\mathbf{G}$  is the Green's function tensor representing the impulse response of the medium. In a more formal way,  $G_{ij}(\mathbf{x}, t, \xi)$  is the  $i$ -th component of the displacement recorded at the position  $\mathbf{x}$  and at the time  $t$ , generated by a unidirectional impulse force acting in the  $j$ -th direction at  $\xi$  at time zero. Thanks to the property of reciprocity of the Green's function, we can exchange the source and receiver positions and write  $G_{mk}(\mathbf{x}, t - \tau, \xi) = G_{km}(\xi, t - \tau, \mathbf{x})$ . The quantity:

$$c_{ijkl} \frac{\partial G_{km}}{\partial \xi_l}(\xi, t - \tau, \mathbf{x}) n_j = T_{im}^G(\xi, t - \tau, \mathbf{x})$$

is the stress on the fault plane generated by an impulsive force at  $\mathbf{x}$ , contracted by the normal, that is the Green's traction  $\mathbf{T}_m^G$  on the fault plane generated by an impulse force at  $\mathbf{x}$  directed along the  $m$ -th direction. We can simplify the representation theorem as follow:

$$u_m(\mathbf{x}, t) = \int_{\Sigma} \delta u_i(\xi, \tau) * T_{im}^G(\xi, t, \mathbf{x}) d\xi \quad 1.2$$

where we denoted with \* the convolution operator. In this discussion we consider only mechanism representative of seismic rupture with dominant shear faulting mechanism, that means rupture may only occur in mode II (in-plane: slip parallel to the rupture direction) or mode III (anti-plane: on-fault slip orthogonal to the rupture direction). Therefore, in such a case, the component of the slip normal to the fault is always zero, reducing to six the numbers of non-zero components of the traction needed for the computation of the displacement.

The relation (1.2) can be generalized for an extended seismic source as a superposition of double couple point sources, as it is common in seismology (body force equivalence). For an isotropic medium the observed displacement is independent on the Lamé constant  $\lambda$  and we have:

$$u_m(\mathbf{x}, t) = \int_{-\infty}^{+\infty} d\tau \int_{\Sigma} \delta u_i(\xi, \tau) \mu \left( \frac{\partial G_{mi}}{\partial \xi_j}(\xi, t - \tau, \mathbf{x}) + \frac{\partial G_{mj}}{\partial \xi_i}(\xi, t - \tau, \mathbf{x}) \right) n_j d\xi$$

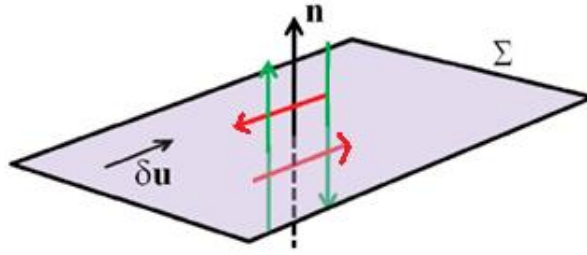


Figure 1.2: The double couple which can be used as an elementary source for the computation of the representation integral, Figure from Festa and Zollo (2012)

For the first contribution in the brackets, we have:

$$\frac{\partial G_{mi}}{\partial \xi_j} n_j = \frac{\partial G_{mi}}{\partial \xi_n} \approx \frac{G_{mi}^2 - G_{mi}^1}{\Delta \xi_n} \quad 1.3$$

Superscripts indexes are referred to as the quantities computed on the two sides of the fault, while  $\Delta \xi_n$  is the distance along the normal direction. The discrete formula (1.3) represents the superposition of the displacements provided by a couple of opposite forces acting on the two sides of the fault, in the direction of the slip (red couple in Figure 1.2). As  $\Delta \xi_n \rightarrow 0$ , the distance between the forces composing the couple becomes shorter, giving rise to a moment on the fault, with in-plane forces and arm along the normal direction. The moment would tend to

locally rotate the fault, but it is balanced by a second couple acting on a plane perpendicular to the fault. Looking also on the second term in the brackets  $\left(\frac{\partial G_{mj}}{\partial \xi_i}\right)$ , we see that this couple is formed by two forces directed along the fault normal with the arm long the slip direction (green couple in Figure 1.2). Indicating with  $D_{mi}$  the m-th component of the displacement generated by such a double couple, the representation theorem can be writtens as:

$$u_m(\mathbf{x}, t) = \mu \int_{\Sigma} \delta u_i(\xi) * D_{mi}(\xi, \mathbf{x}) d\xi$$

We replaced the contribution of the derivative of Green function with the displacement generated by a double couple of forces, whose orientation is defined by the slip and the fault normal vectors.

Another properly way to write the relationship (1.2) is:

$$u_m(\mathbf{x}, t) = \int_{-\infty}^{+\infty} d\tau \int_{\Sigma} \mu(\delta u_i(t)n_j + \delta u_j(t)n_i) \frac{\partial G_{mi}(t - \tau)}{\partial \xi_j} d\xi$$

The quantity  $m_{ij} = \mu(\delta u_i n_j + \delta u_j n_i)$  has the dimension of a moment per area unit and it is denoted as the moment density tensor. It is clearly symmetric. For observer distances and signal wavelengths much larger than the size of the fault, we can assume that the Green's function derivatives are constant, and we can bring their relative terms outside from the surface integral. The remaining part inside the integral,  $\int_{\Sigma} m_{ij} d\xi = M_0 = \mu A \delta \bar{u}$ , has the dimension of a moment and it is called the *seismic moment* and it is a key overall measure of the earthquake size. In the far field approximation, it is related to the amplitude of the displacement spectrum in the limit of the zero frequency, as we will see later.

### 1.1.1 Point source

The point source approximation, as said above, is valid if the receiver is at a distance sufficiently large with respect to the length of the fault and if observation

wavelengths are also large. In this case, we can represent the source by a system of body forces acting at a point in the space.

We will follow another formalism to infer other characteristics. Let us consider an elastic medium of volume  $V$ , surrounded by a surface  $S$ , and that inside of it there is a small region of volume  $V_0$ , surrounded by a surface  $\Sigma$  that we call the focal region, that is the region in which the fracture takes place. The process occurring in  $V_0$  can be represented by a distribution of body forces per volume unit  $F(\xi, t)$  only acting inside  $V_0$ . We assume that no further body forces are present and consider only elastic displacements and stresses outside the focal region. In this case, we can write the equation of motion as (Aki and Richards,2002):

$$\int_{V-V_0} [\rho \ddot{u}_i(x_i, t) - \tau_{ij,j}(x_i, t)] dV = \int_{V_0} F_i(\xi_i, t) dV \quad 1.4$$

where  $\rho$  is the density,  $\tau$  is the stress (the notation  $_{,j}$  denotes the derivative in respect to  $x_j$  coordinate),  $\xi_i$  and  $x_i$  denotes the coordinates inside and outside of the focal region, respectively. In the static case we have:

$$F_i(\xi_i, t) = -\tau_{ij,j}$$

In the case of a volume  $V$  infinite, we have:

$$\lim_{V_0 \rightarrow 0} \int_{V_0} F_i(\xi_i, t) dV = F_i(t) \quad 1.5$$

$F_i(t)$  are the forces per unit volume applied at the point selected as the origin of the  $x_i$  coordinates.

The equation (5) becomes:

$$\rho \ddot{u}_i(t) - \tau_{ij,j}(t) = F_i(t)$$

That, for a homogeneous medium, can be expressed in terms of displacement thanks to the Hooke's law:

$$\rho \ddot{u}_i(t) - c_{ijkl} u_{k,lj}(t) = F_i(t)$$

where  $,lj$  denotes the derivative in respect to  $x_l$  coordinate and  $x_j$ . We can furtherly simplify using the Lamé constants:

$$(\lambda + \mu) \nabla(\nabla \cdot \mathbf{u}) + \mu \nabla^2 \mathbf{u} + \mathbf{F} = \rho \ddot{\mathbf{u}}$$

That can be used to represent the kinematic processes of earthquakes. The volume forces  $\mathbf{F}$  are defined only inside a certain volume. An example of simple time-dependence is provided by the harmonic function  $F(\mathbf{x}, t) = F(\mathbf{x})e^{i\omega t}$ . This form is useful when Fourier theory is adopted. Another general form for body forces is given by a unit impulsive force in space and in time having an arbitrary direction:

$$F_i(\mathbf{x}_s, t) = \delta(\mathbf{x}_s - \boldsymbol{\xi}_s) \delta(t - \tau) \delta_{ni}$$

This force is applied at the point  $\boldsymbol{\xi}_s$  at the time  $\tau$  and is null outside this point and time. Its orientation is given by three components of subscript  $n$ . If we substitute this force in equation (1.4), the solutions obtained are the elastic displacements, as a function of time  $t$ , for any point of coordinates  $\mathbf{x}$  in a certain volume  $V$  surrounded by a surface  $S$ . We can replace the stress in terms of the derivative of the displacement, substituting the displacement with  $G_{ni}$  and inserting this impulsive force in the equation (4) and we obtain:

$$\int_V \rho \dot{G}_{ni} dV - \int_S c_{ijkl} G_{nk,l} v_j dS = \int_V \delta(\mathbf{x}_s - \boldsymbol{\xi}_s) \delta(t - \tau) \delta_{ni} dV$$

If body forces are limited to the focal region  $V_0$  and on its surface  $\Sigma$  the stresses and displacements are null, we obtain, for the volume of interest  $V$  surrounded by a surface  $S$ :

$$u_i = \int_{-\infty}^{\infty} d\tau \int_{V_0} F_k G_{ki} dV + \int_{-\infty}^{\infty} d\tau \int_S (G_{ji} T_j - u_j C_{jklm} G_{li,n} v_k) dS$$

where  $T_j = \tau_{ij} v_j$  is the stress vector,  $v_i$  is the normal to the surface element  $dS$ , and  $G_{ki}$  is the Green's function of the medium, that represents the effect of the propagation. If the medium is infinite, the conditions on the surface  $S$  are homogeneous (i.e., stress and displacement on it are null and we have:

$$u_i(\mathbf{x}_s, t) = \int_{-\infty}^{\infty} d\tau \int_{V_0} F_k(\boldsymbol{\xi}_s, \tau) G_{ki}(\mathbf{x}_s, \boldsymbol{\xi}_s, t - \tau) dV$$

The function  $G_{ki}$  acts as a 'propagator' of the effects of the forces  $F_k$  from the points where they are acting to points  $\mathbf{x}_s$  outside  $V_0$  where the elastic displacements  $u_i$  are evaluated. For a point focus at the origin of coordinates, i.e.  $\boldsymbol{\xi}_s = \mathbf{0}$ , we have:

$$u_i(\mathbf{x}_s, t) = \int_{-\infty}^{\infty} F_k(\tau) G_{ki}(\mathbf{x}_s, t - \tau) d\tau$$

The elastic displacements are given by the time convolution of the forces acting at the focus with Green's function. For simple model of the Earth, Green's function can be computed analytically once the elastic properties of the medium are known. For example, the required parameters are inferred from geophysics and geological investigations aimed at providing images of the subsoil in terms of elastic properties, such as seismic wave velocity, density and other important parameters. The uncertainties associated with the determination of the Green's functions affect the estimation of the source parameters and how deep inside we can know about the characteristics of the seismic source.

If we treat the case of homogeneous and isotropic medium, the pure shear displacement for a receiver located at a distance  $r$  from a point source is given by the formula:

$$u(t) = \frac{1}{4\pi\rho r c^3} \mathcal{R}^c \mu \langle \Delta \dot{u}(t) \rangle \Sigma$$

where  $\rho$  is the medium density and  $c$  represent the seismic wave velocity,  $\mathcal{R}^c$  is the radiation pattern coefficient for the phase  $c$ ,  $\mu$  is the shear modulus,  $\Sigma$  is the fault surface and  $\langle \Delta \dot{u}(t) \rangle$  is the average on the fault of slip-rate. The term  $\frac{1}{4\pi\rho r c^3} \mathcal{R}^c$  is the Green's function for an homogeneous and isotropic medium. The term  $\frac{1}{r}$  represents the amplitude decay with the distance (geometric attenuation) while the radiation coefficient  $\mathcal{R}^c$  depends on the focal mechanism, on the orientation of fault plane and on the angles between the receiver position and the direction of the seismic ray, and it accounts for the non-isotropic radiation of the seismic source. The term  $\mu \langle \Delta \dot{u}(t) \rangle \Sigma$  is proportional to the dislocation and to its time variation. Since we can consider that  $\mu$  and  $\Sigma$  not varying in time, the source term can be written as:

$$\mu \langle \Delta \dot{u}(t) \rangle \Sigma = \frac{dM_0(t)}{dt}$$

The term  $M_0(t) = \mu \langle \Delta u(t) \rangle \Sigma$  is the *scalar seismic moment* and it represents the moment of one of the two forces-couple adopted for describe from a dynamical point of view the seismic source, and which produce the dislocation on the fault surface.

It is possible to determine the seismic moment by analyzing the data in the frequency domain rather than in that of time. We then compute the Fourier transform of the given displacement from the equation

$$\tilde{u}(w) = \int_0^{\infty} u(t) e^{-iwt} dt = \frac{1}{4\pi\rho c^3} \frac{\mathcal{R}^c}{r} \mu \Sigma \int_0^{\infty} \langle \Delta \dot{u}(t) \rangle e^{-iwt} dt$$

In the calculation of the Fourier transform we restricted the integration interval to  $[0, \infty [$  assuming that the displacement  $u$  is zero for  $t < 0$ . At the limit for low frequencies ( $\omega \rightarrow 0$ ):

$$\begin{aligned}\tilde{u}(w \rightarrow 0) &= \frac{1}{4\pi\rho c^3} \frac{\mathcal{R}^c}{r} \mu \Sigma \int_0^\infty \langle \Delta \dot{u}(t \rightarrow \infty) \rangle dt = \frac{1}{4\pi\rho c^3} \frac{\mathcal{R}^c}{r} \mu \Sigma \langle \Delta \dot{u}(t \rightarrow \infty) \rangle \\ &= \frac{1}{4\pi\rho c^3} \frac{\mathcal{R}^c}{r} \mu \Sigma M_0\end{aligned}$$

In this case the seismic moment is evaluated by calculating the low-frequency value of the Fourier spectrum of the ground displacement for a certain phase (e.g., direct P wave).

### 1.1.2 Single and double couples

For the seismic waves of long period or comparable with the rupture duration, and for the wavelengths that are large compared to source dimension it is possible to replace the complex process of dislocation with the simple representation of figure 1.3. The source is modelled as a point and the whole dislocation process is described by a simple dislocation function  $\Delta u(t)$  associated with a single point barycentric with respect to the entire fault surface. In large wavelengths approximation, the contributions to the seismic radiation from the individual points of the fault are not distinguished at the receiver. The average dislocation model is sufficiently simple to be represented by a system of forces dynamically equivalent, that can produce a similar seismic radiation. In order to simulate the process of dislocation a couple of time-varying forces applied inside of the elastic medium is needed. The main downside of this model is that it does not explicitly include the physics of the beginning and arrest of the rupture. If we consider a model with a *single couple* of forces, the moment associated is not zero, so since it would be not balanced, introducing rotations in the medium in which the displacement occurs. We expect the presence of a second couple of forces, orthogonal to the first one, that balance the moment inside the medium. This is the so-called *double couple* source model (as mentioned in the paragraph 1.1).

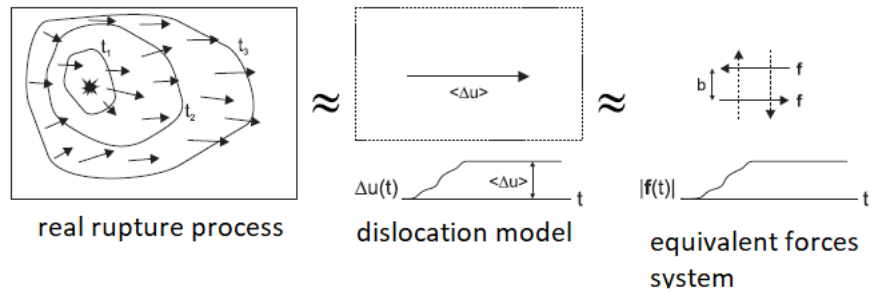


Figure 1.3: The real fracture process at the source involves a series of rather complex phenomena. It can be approximated by an average displacement model as a function of time that can be represented by an equivalent system of forces which can be incorporated directly into the equations of motion. Figure taken from T. Lay and T.C. Wallace (1995). *Modern global seismology*. Academic Press.

### 1.1.3 Radiation Pattern

The wave radiation emitted by a seismic source is not isotropic. This characteristic, which is expected from the theoretical modelling of the seismic source, is also observed experimentally. The source radiation pattern describes the angular distribution of ground motion amplitudes around the seismic source. In the figure 1.4, we show an example of radiation pattern for the P-wave.

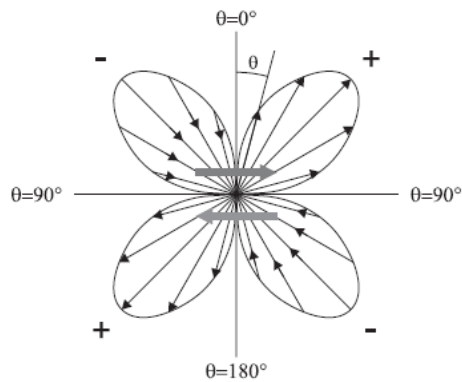


Figure 1.4: Radiation pattern of the P waves in far field and high-frequency approximation for a vertical fault. The grey arrows indicate the sliding direction with respect to the fault plane. The black arrows represent the amplitude of the P wave, as the azimuth varies  $\vartheta$  with respect to the fault plane. This diagram is identical either for a single pair or double pair source.

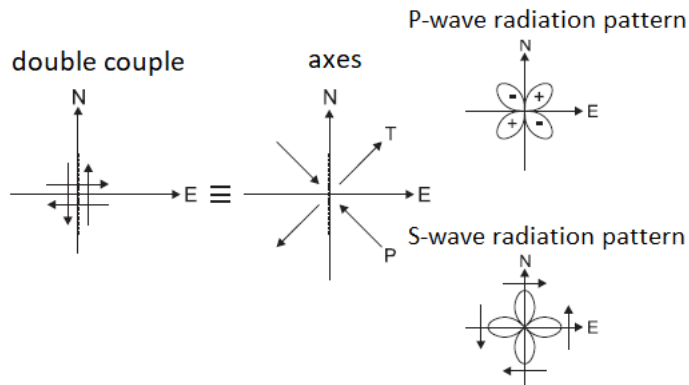


Figure 1.5: Radiation diagrams for P and S waves in far field approximation for single and double models couple (Zollo and Emolo, *Terremoti e onde* 2011).

In this case the radiation pattern has four lobes (or quadrants) having alternating directions of motions, outward or positive (compression) and inward or negative (dilatation). The radiation pattern for S-waves is different according to different models (single or double couples) as we show in figure 1.5. In the double couple model, the lobes are rotated by  $45^\circ$  with respect to the lobes of the P-waves. For this reason, where the P-waves has maximum amplitude the displacement for the S-waves is null (nodal points). The experimental observations suggest that the 'true' model is the double couple one, because in this case we observe a four lobes radiation pattern also for S-waves. Although the single model couple had less sense than the other from the physical point of view, the reason why he did not come rejected was that the seismic radiation for the P waves associated with the two models had to be indistinguishable. When, following the installation of three-component seismometers, accurate data were made available about the azimuthal variation of the amplitude of the S waves in occasion of earthquakes associated with transcurrent faults, observations confirmed that the two pair was the most appropriate one as, contrary to what was expected from the point of view theoretically, the amplitude of the S waves was significantly different from zero in the corresponding directions to the orientation of the fault, where the single pair model predicted a zero amplitude of the seismic radiation S (Fig. 1.6).

Figure 1.5 shows also how the double pair of forces system can be equivalently represented by a pair of orthogonal dipoles lying in the plane perpendicular to that of fault and form an angle of  $45^\circ$  to it (principal axes). The dipole directed towards the source is the compression axis or P axis and lies in the dilation quadrants of the radiation diagram of P wave. The dipole that moves away from the source is instead the tension axis or T axis and lies in the compression quadrants of the P wave radiation pattern

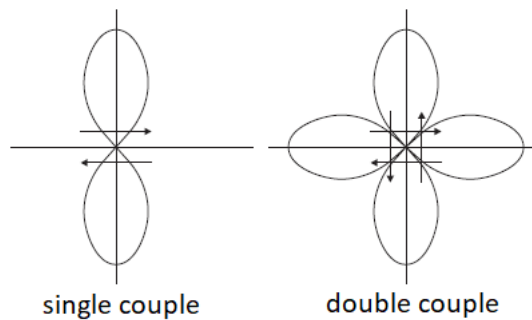


Figure 1.6: Double pair of forces system. Figure shows the system associated with a vertical transcurrent fault left (paragraph 8.2.6) facing north. A completely equivalent system is made up of two dipoles (main axes). The figure is inspired by a similar example reported in T. Lay and T.C. Wallace (1995). *Modern global seismology*. Academic Press

### 1.1.4 Fault mechanisms and classification

The focal mechanism is an important parameter that is estimated from the seismic data in the hypothesis of a point source. This consists in obtaining the orientation

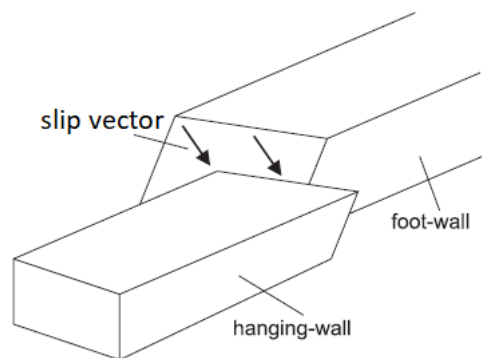


Figure 1.7: Convention for the identification of the two blocks on both sides of a non-vertical fault. The block above of the fault is known as the hanging wall while the block below it is called foot-wall (Zollo and Emolo, *terremoti e onde*, 2011).

of the fault plane and the direction of the dislocation vector on it. In order to describe the orientation of this plane in a system of geographic coordinates, two angles are required: the orientation (or strike) and the slope (or dip). The sliding direction is instead specified by one of two alternative quantities which describe the mean direction of dislocation (slip or plunge). The two sides of the fault surface are known as the hanging-wall and the footwall (Figure 1.7).

If the strike direction is defined by the angle  $\varphi_s$ , measured clockwise, formed by the trace of the fault with the geographic North. An observer looking in this direction sees the hanging-wall block (opposite the foot-wall block) of the fault on their right. Evidently,  $0 \leq \varphi_s \leq 2\pi$ . The dip  $\delta$  of the fault is the angle formed by the fault plane with the surface ground in the vertical plane orthogonal to the strike. It turns out that  $0 \leq \delta \leq \pi/2$ . Finally, the dislocation vector (slip)  $\Delta u$  represents the direction of movement of the hanging-wall respect the footwall. The slip  $\lambda$  defines the angle between the strike direction and the vector of slip and it is in the range  $-\pi \leq \lambda \leq \pi$  (Fig 1.8).

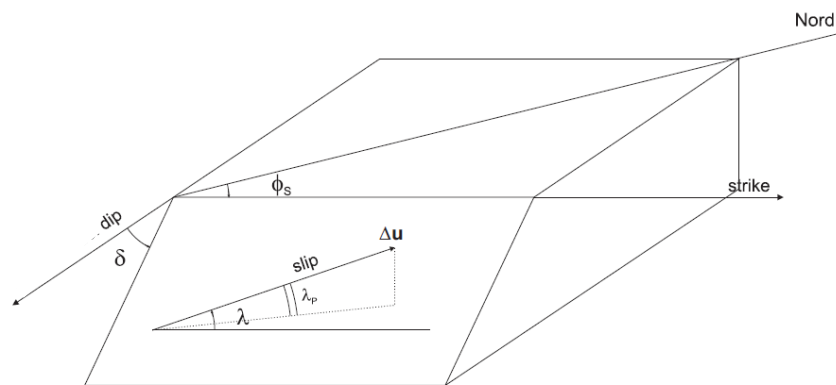


Figure 1.8: Definition of the fault orientation parameters and of the slip vector

If  $\delta$  is different than 0 and  $\pi / 2$ , and  $\lambda$  varies in the interval  $(0, \pi)$ , the corresponding fault is called *reverse* or *thrust fault*; conversely, if  $\lambda$  is included between  $(-\pi, 0)$ , the fault is called *normal*. A *strike-slip* fault is characterised by a slip vector which is horizontal ( $\lambda = 0$  or  $\lambda = \pi$ ). For a vertical strike-slip fault (i.e. for which  $\delta = \pi / 2$  in addition to  $\lambda = 0$  or  $\lambda = \pi$ ) there are two possible choices to define the direction of the strike and, depending on the choice made, it is determined which of the two fault surfaces defines the block hanging-wall (i.e. which block is on the right when looking in the direction of the strike) and such as that of the foot-wall.

Consequently, a right transcurrent fault can be immediately distinguished from a left transcurrent fault using only the slip value: if  $\lambda = 0$  the fault is left transcurrent while if  $\lambda = \pi$  the fault is right transcurrent. A *dip-slip* fault is one for which the slip vector is orthogonal to the strike ( $\lambda = \pm \pi / 2$ ). For a vertical dip-slip fault (i.e. for which  $\delta = \pi / 2$ ) an ambiguity arises again in the strike definition. If we assume that the foot wall lies in the low block and that the strike direction is always that one for which the hanging wall is on the right, we can conclude that

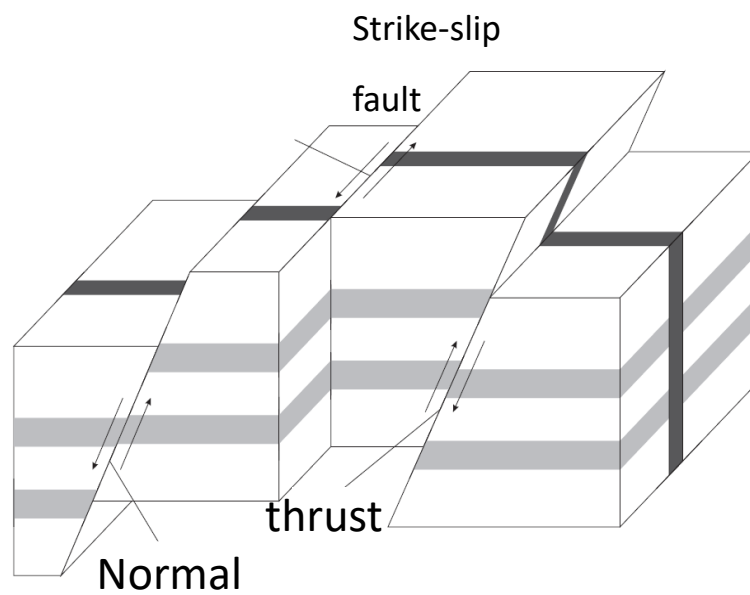


Figure 1.9: Example of different faults; figure from T. Lay and T.C. Wallace (1995), *Modern global seismology*. Academic press

for a dip-slip fault  $\lambda = \pi / 2$  (Fig. 1.9).

### 1.1.5 Fault mechanism computation

The focal sphere for a point source is defined as the sphere centred in the hypocenter and having unit radius. It is the surface on which radiation pattern is represented. The radiation pattern is the azimuthal variation, at fixed distance, of the amplitude of the ground motion caused by P-wave and S-wave. This procedure is based on a back-projection of the wave amplitude following backwards ray path from receiver to the source to find the point at which the ray intersects the sphere. It is, of course, needful to know the velocity model and source location. Of course, any lack of knowledge on these elements, beyond the number and azimuthal distributions of the observations, affects the accuracy of the fault mechanism retrieved. We can specify a point of focal sphere by mean of angular coordinates

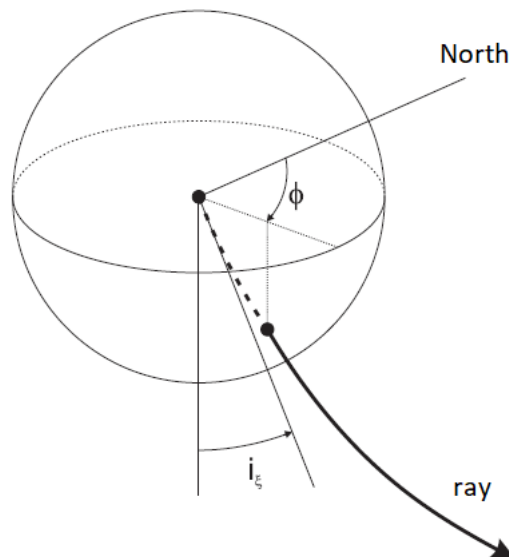


Figure 1.10: focal sphere (Zollo and Emolo, Terremoti e onde,2011)

$(i_\varepsilon, \varphi)$  in a spherical coordinates system centred in the source (Figure 1.10).  $i_\varepsilon = 0$  individuates the vertical direction oriented on the bottom and  $\varphi$  the angle is the azimuth with respect to the Nord.

In an homogeneous and infinite medium and in the case of pure shear displacement and a source composed by a double-couple of forces, in terms of far-field  $FF$ , intermediate-field  $IF$ , near-field  $NF$ , we have that the displacement  $\mathbf{u}$  in a point  $\mathbf{r}$  in terms of seismic moment  $M_0(t)$  is given by:

$$\begin{aligned}
\mathbf{u}(\mathbf{r}, t) = & \frac{1}{4\pi\rho} \mathcal{R}^{NF} \frac{1}{r^4} \int_{r/v_p}^{r/v_s} \tau M_0(t - \tau) d\tau + \frac{1}{4\pi\rho v_p^2} \mathcal{R}_P^{IF} \frac{1}{r^2} M_0\left(t - \frac{r}{v_p}\right) \\
& + \frac{1}{4\pi\rho v_s^2} \mathcal{R}_S^{IF} \frac{1}{r^2} M_0\left(t - \frac{r}{v_s}\right) + \frac{1}{4\pi\rho v_p^3} \mathcal{R}_P^{FF} \frac{1}{r^2} \dot{M}_0\left(t - \frac{r}{v_p}\right) \\
& + \frac{1}{4\pi\rho v_s^3} \mathcal{R}_S^{FF} \frac{1}{r^2} \dot{M}_0\left(t - \frac{r}{v_s}\right)
\end{aligned}$$

With  $\rho$ ,  $v_p$ ,  $v_s$  that are respectively the density, the P-wave and S-wave velocity. The radiation pattern in far-field approximation is completely equivalent to the radiation pattern for the static displacement at all distances from the source and, in particular, on the focal sphere. Radiation patterns are given by:

$$\begin{aligned}
\mathcal{R}^{NF} &= 9 \sin 2\theta \cos \varphi \hat{\mathbf{r}} - 6(\cos 2\theta \cos \varphi \hat{\boldsymbol{\theta}} - \cos \theta \sin \varphi \hat{\boldsymbol{\phi}}) \\
\mathcal{R}_P^{IF} &= 4 \sin 2\theta \cos \varphi \hat{\mathbf{r}} - 2(\cos 2\theta \cos \varphi \hat{\boldsymbol{\theta}} - \cos \theta \sin \varphi \hat{\boldsymbol{\phi}}) \\
\mathcal{R}_S^{IF} &= -3 \sin 2\theta \cos \varphi \hat{\mathbf{r}} + 3(\cos 2\theta \cos \varphi \hat{\boldsymbol{\theta}} - \cos \theta \sin \varphi \hat{\boldsymbol{\phi}}) \\
\mathcal{R}_P^{FF} &= \sin 2\theta \cos \varphi \hat{\mathbf{r}} \\
\mathcal{R}_S^{FF} &= \cos 2\theta \cos \varphi \hat{\boldsymbol{\theta}} - \cos \theta \sin \varphi \hat{\boldsymbol{\phi}}
\end{aligned}$$

where  $\mathbf{r}$  is the length of the vector from the center and proportional to the amplitude of the radiation pattern,  $\varphi$  is the angle of the projection of  $\mathbf{r}$  in the horizontal plane respect to the North direction,  $\theta$  is the angle between  $\mathbf{r}$  and the vertical direction, while  $\hat{\mathbf{r}}$ ,  $\hat{\boldsymbol{\phi}}$  and  $\hat{\boldsymbol{\theta}}$  are respectively the versors. It is also possible to obtain the final static displacement value associated with a shear displacement of seismic moment  $M_0$  by calculating the limit for  $t \rightarrow \infty$  of the quantities  $\dot{M}_0(t - \tau)$ ,  $M_0(t - \tau)$  and  $\int_{r/v_p}^{r/v_s} \tau M_0(t - \tau) d\tau$  in the hypothesis that the seismic moment has a constant final value equal to  $M_0(\infty)$ . In this case we have:

$$\begin{aligned}
\mathbf{u}(\mathbf{r}, t \rightarrow \infty) = & \frac{M_0(\infty)}{4\pi\rho r^2} \left[ \frac{1}{2} \left( \frac{3}{v_s^2} - \frac{1}{v_p^2} \right) \sin 2\theta \cos \varphi \hat{\mathbf{r}} \right. \\
& \left. + \frac{1}{v_p^2} (\cos 2\theta \cos \varphi \hat{\boldsymbol{\theta}} - \cos \theta \sin \varphi \hat{\boldsymbol{\phi}}) \right]
\end{aligned}$$

The radiation pattern in the far-field approximation is completely equivalent to the radiation pattern for the static displacement at all distances from the source and, in particular, on the focal sphere.

Let us now consider the radiation pattern for the displacement P associated with a shear dislocation, arbitrarily oriented. We expect that, in correspondence to a dislocation, the particles of the medium that belong to the arranged quadrants around the fault are subject to an initial motion that is compressive (i.e. directed towards the receiver) or dilated (i.e. directed towards the source). In the spherical reference system, the displacement for P waves is proportional to  $\sin 2\theta \cos \varphi$ . When  $\varphi = 0$ , it holds that is, in the  $x_1x_3$  plane, it turns out  $u_r \propto \sin 2\theta$  which corresponds to four diagram lobes reflecting the alternating sign quadrants (Figure 1.11). Polarity reversal occurs when the amplitude of the motion has become zero. Outside the dislocation zone therefore, there is a continuous transition from the motion directed towards the source to that directed towards opposite to the source. The maximum amplitude for the displacement P is therefore expected at half of the four quadrants, that means  $45^\circ$  from the fault plane belonging to the  $x_1x_2$  plane.

The polarity of the displacement for the direct P wave is preserved along the path of the ray to any receiver. Consequently, if a sufficient number of observations first motion of P-wave is available, if we back-project the wave amplitude from receiver to the source, it is possible to determine the orientation of the fault planes. The symmetry inherent in the quadrilobar radiation pattern with alternating signs makes it impossible to determine uniquely the fault plane with the only observations of the P-wave polarities and/or P-wave amplitudes.

In fact, there is a second plane orthogonal to the fault plane (called auxiliary plane) on which the fracture process could have occurred, but with the opposite direction to the slip vector, which is indistinguishable from the fault plane on the base of P polarity data only. However, if it is possible to measure post-seismic static deformations on the surface or to observe the fault trace, this determination is

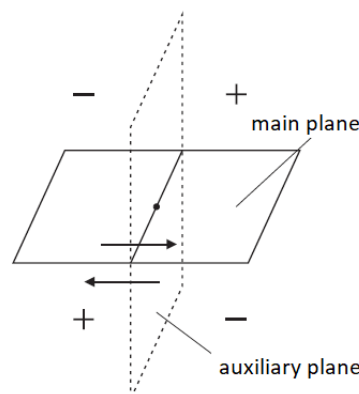


Figure 1.11: Sign of the initial motion P with respect to the plane of fault and to the auxiliary plane (Zollo and Emolo, *Terremoti e onde*, 2011).

unique. Furthermore, the hypocenters of the aftershocks of a strong earthquake are often located on the fault plane which produced the main earthquake and that can thus be distinguished from the auxiliary plane. This is of course simpler in the case of transcurrent fault mechanisms where the main and auxiliary planes have an orthogonal orientation directly visible on the earth's surface. The distinction is more difficult between main plane and auxiliary plane in the case of normal or reverse faults, unless the hypocenters of the replicas are determined with extreme precision. The stereographic and equal length projections are used to project on a plane the information relating to the polarities represented on the focal sphere. It is generally projected the lower hemisphere since, by virtue of the symmetry inherent in the radiation diagrams, the seismic rays that leave the source upwards, and therefore intersect the upper part of the sphere focal length, can be brought back to the lower hemisphere simply by adding  $180^\circ$  to the azimuth of the stations. The fault plane and the auxiliary plane intersect the focal sphere and these projections are represented as curves separating the compressive P motions from the dilatational P motions.

Figure 1.12 shows the geographic reference system and that identified by the versors  $\hat{l}$ ,  $\hat{m}$  and  $\hat{n}$  in the directions, respectively, P, SV, and SH. The equations for P and S wave, in far field approximation, associated with a double couple point source having orientation  $\varphi_s$ ,  $\delta$  and  $\lambda$  and for a take off angle  $i_h$  for a ray path which reach the receiver having an azimuth  $\varphi_R$  are given by:

$$\mathbf{u}_p(\mathbf{r}, t) = \frac{1}{4\pi\rho r v_p^3} \mathcal{R}^P \frac{\partial}{\partial t} \left[ M_0 \left( t - \frac{r}{v_p} \right) \right]$$

$$\mathbf{u}_{sv}(\mathbf{r}, t) = \frac{1}{4\pi\rho r v_s^3} \mathcal{R}^{SV} \frac{\partial}{\partial t} \left[ M_0 \left( t - \frac{r}{v_s} \right) \right]$$

$$\mathbf{u}_{sh}(\mathbf{r}, t) = \frac{1}{4\pi\rho r v_s^3} \mathcal{R}^{SH} \frac{\partial}{\partial t} \left[ M_0 \left( t - \frac{r}{v_s} \right) \right]$$

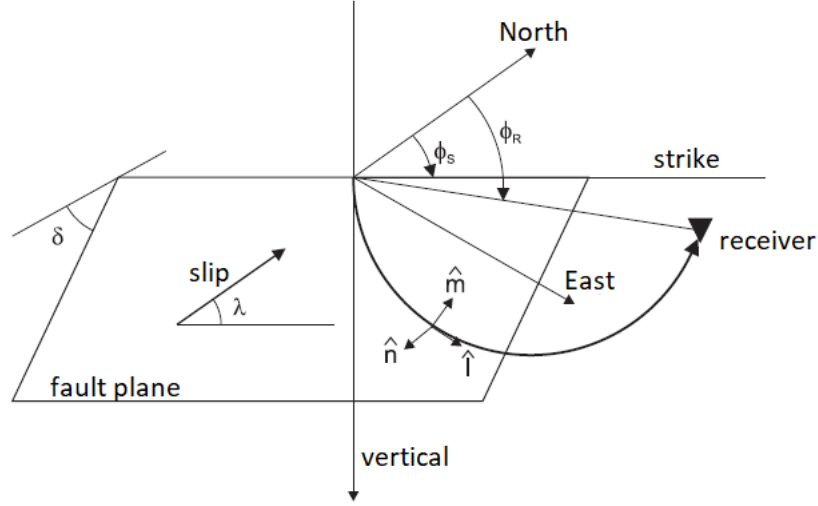


Figure 1.12: Definition of a geographical reference system with the positive  $x_3$  axis (vertical axis) downwards. The strike angle of the fault plane  $\phi_s$  is measured with respect to the geographic North as well as the azimuth  $\phi_R$  of the receiver. The dip  $\delta$  of the fault is measured with respect to the horizontal plane while the slip angle  $\lambda$ , measured with respect to the strike direction, identifies the direction of the vector dislocation on the fault. The seismic ray that reaches the station has a take-off angle  $i_h$  with respect to the  $x_3$  axis (vertical axis).  $x_1$  is along East direction and  $x_2$  along North Direction. The versors  $\hat{l}$ ,  $\hat{m}$  and  $\hat{n}$  identify a reference system in the directions, respectively, P, SV, and SH (Zollo and Emolo, Terremoti e onde, 2011).

Where  $\mathcal{R}^P$ ,  $\mathcal{R}^{SV}$  and  $\mathcal{R}^{SH}$  are the radiation pattern respectively for P, SV and SH wave and are equal to:

$$\begin{aligned} \mathcal{R}^P = & \cos \lambda \sin \delta \sin^2 i_h \sin 2\varphi - \cos \lambda \cos \delta \sin 2i_h \cos \varphi \\ & + \sin \lambda \sin 2\delta (\cos^2 i_h - \sin^2 i_h \sin^2 \varphi) \\ & + \sin \lambda \cos 2\delta \sin 2i_h \sin \varphi \end{aligned}$$

$$\begin{aligned} \mathcal{R}^{SV} = & \sin \lambda \cos 2\delta \cos 2i_h \sin \varphi - \cos \lambda \cos \delta \cos 2i_h \cos \varphi \\ & + \frac{1}{2} \cos \lambda \sin \delta \sin 2i_h \sin 2\varphi - \frac{1}{2} \sin \lambda \sin 2\delta \sin 2i_h (1 + \sin^2 \varphi) \end{aligned}$$

$$\begin{aligned} \mathcal{R}^{SH} = & \cos \lambda \cos \delta \cos i_h \sin \varphi + \cos \lambda \sin \delta \sin i_h \cos 2\varphi \\ & + \sin \lambda \cos 2\delta \cos i_h \cos \varphi - \frac{1}{2} \sin \lambda \sin 2\delta \sin i_h \sin 2\varphi \end{aligned}$$

where  $\varphi = \varphi_R - \varphi_S$ .

### 1.1.6 Information from a focal mechanism

The graphic representation of the focal mechanism of an earthquake, known as a "beach-ball" (due to the characteristic shape of light and dark segments, Fig. 1.13), represents the deformation in a volume circumscribed to the seismic source (assumed to be point-like) from which the seismic waves radiate. The focal mechanism allows to trace three important pieces of information on the development modalities of the seismic fracture:

- the orientation in the space of the fracture surface (fault), assumed planar, through the strike and dip angles;
- the direction of the dislocation vector, which represents the relative movement of the separate blocks from the fracture surface, by mean of the slip angle;
- the orientation of the main axes of effort, P (compressive) and T (extensional), which individuate the directions of the dipoles of forces.

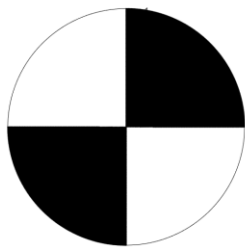


*Figure 1.13: Example of beachball.*

The beach-ball diagram is constructed through representation in stereographic projection of the polarity of the first arrival P recorded at a set of seismic stations displaced around the epicenter. Nowadays the focal mechanism is also determined using other information, such as the polarization of the S waves, the amplitude of the displacement spectrum or the comparison between theoretical (synthetic) and observed seismograms.

Using the seismograms recorded in the first tens of minutes following a strong earthquake, different seismic agencies calculate the main source parameters (location, magnitude, seismic moment) and therefore perform the determination

of the size and orientation of the components of the moment tensor. From the latter, in the hypothesis of one double-torque distribution of forces, it is possible to trace the displacement vector and orientation of the possible fracture planes. The orientation of the fracture plane and the direction of the dislocation vector are determined with an accuracy that depends on the azimuth coverage of the stations' measure. The estimate of the orientation of the axes of compressive and extensive stress, starting from the axes P and T of the focal mechanism, on the other hand, can be fallacious in the case in which the fracture is pre-existing. In this case the angle between the direction of the forces acting and the fracture plane can be less than 45°, which is the predicted value of fracture mechanics for "new" fractures.

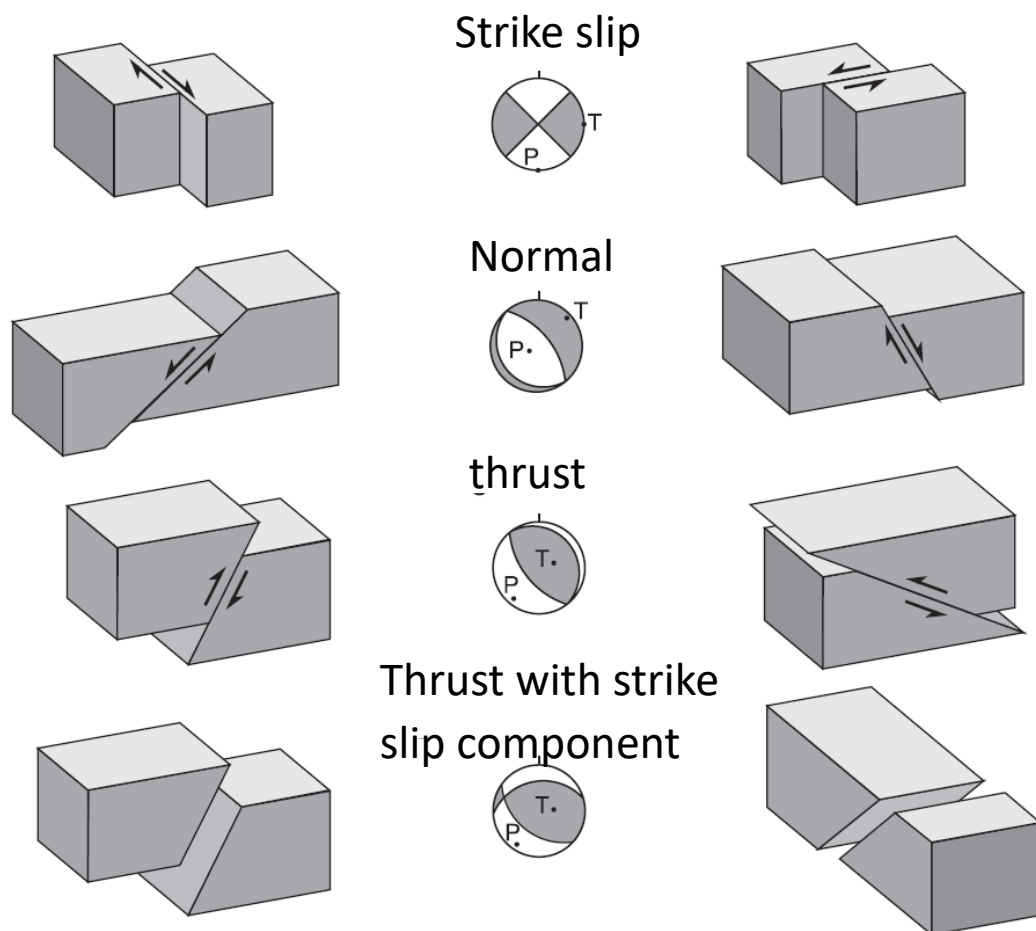


Figure 1.14: Representation of the focal mechanisms for the different types of fault. The regions in gray correspond to P motions of the compressive type. The figures on the sides of each beach ball represent the two possible type of movement corresponding to the focal mechanism, highlighting the ambiguity existing between the fault plane and that auxiliary.

In the beach-ball diagram, the coloured segments indicate sectors with positive P-wave amplitudes, while those in white indicate compression. This is the reason why on the focal sphere the P and T axes are represented by points that are positioned inside of the wedges in white and in colour, respectively.

As mentioned before, the areas in compression and expansion on the focal sphere are separated by two orthogonal planes, which correspond to the potential planes on which it is developed the seismic fracture (Fig 1.14). The real fault plane is not uniquely deducible from the analysis of the mechanisms and it is necessary, to resolve this ambiguity, to integrate other information such as, for example, the identification of the fault through surface geological observations, the spatial distribution aftershocks or modelling of the directivity effect.

## 1.1.7 Kagan's angle

The Kagan's angle definition was presented by Kagan (1991) in a study in which he inferred the focal mechanism rotations for obtaining a better prediction of the future evolution of rupture during earthquake sequences. He proposed an inversion scheme which yields all of the four rotations of one double couple to be superimposed upon another one, in the way to define a minimum rotation angle between two earthquake focal mechanisms.

### 1.1.7.1 *Calculation of the Rotation Quaternion for double couple*

Using the correspondence between normalized quaternions and 3D rotations, we can calculate the normalized quaternion corresponding to an arbitrary double couple (Klein, 1932; Le Pichon et al., 1973; Altmann, 1986; Chang et al., 1990; Kagan, 1991).

The quaternion  $\mathbf{q}$  is defined as

$$\mathbf{q} = q_0 + q_1\mathbf{i} + q_2\mathbf{j} + q_3\mathbf{k}$$

$q_0$  is the scalar part,  $q_1$ ,  $q_2$  and  $q_3$  are the components of a 'pure' quaternion, and the imaginary units  $\mathbf{i}$ ,  $\mathbf{j}$  and  $\mathbf{k}$  obey the multiplication rules:

$$\mathbf{i}^2 = \mathbf{j}^2 = \mathbf{k}^2 = -1$$

$$ij = -ji = k, ki = -ik = j, jk = -kj = i$$

The multiplication of quaternions is not commutative, and the non-commutability is also a property of finite 3D rotations. The conjugate  $\mathbf{q}^*$  and the inverse  $\mathbf{q}^{-1}$  of a quaternion are defined as

$$\mathbf{q}^* = q_0 - q_1\mathbf{i} - q_2\mathbf{j} - q_3\mathbf{k}, \mathbf{q}\mathbf{q}^{-1} = 1$$

A normalized quaternion requires the additional request that

$$q_0^2 + q_1^2 + q_2^2 + q_3^2 = 1$$

The normalized quaternion defines a 3D rotation. The vector part of a quaternion corresponds to the rotation axis. For normalized quaternion results

$$\mathbf{q}^* = \mathbf{q}^{-1}$$

Using normalized quaternions, we can compute the rotated vector  $\mathbf{R}(\mathbf{v})$  by using the rules of quaternion multiplication as:

$$\mathbf{R}(\mathbf{v}) = \mathbf{q}\mathbf{v}\mathbf{q}^{-1}$$

A double couple focal mechanism is characterized by three degrees of freedom, therefore we can obtain an appropriate correspondence of the double-couple source with normalized quaternions. In particular, the quaternion  $\mathbf{1} = [1,0,0,0]$  corresponds to the double couple with the **T** axis (0,0) and the **P** axis (0,90) which we define the 'original' (non-rotated) position of a double couple. The first term in parentheses is the *plunge* angle in degrees, the second value is the azimuth. The original, right-handed system of source coordinates consists of the **T** axis pointing toward North, the **P** axis pointing eastward, and the **B** axis pointing down. Only four right-handed coordinate systems can be formed from these three axes. We can represent an earthquake focal mechanism in two ways: 1) through plunge  $\lambda_p$  and azimuth  $\alpha$  of the **T** and **P** axes; 2) through fault plane angles  $\varphi$  (strike),  $\delta$  (dip) and  $\lambda$  (slip). In the first case, we compute the components of the **T** axis as:

$$t_x = \cos \alpha \cos \lambda_p, t_y = \sin \alpha \cos \lambda_p, t_z = \sin \lambda_p$$

where  $\mathbf{t}$  is a unit vector in the direction of the  $\mathbf{T}$  axis. The components of the  $\mathbf{P}$  axis are calculated in a similar manner. In the second case, we compute the components of the slip  $\mathbf{u}$  and fault normal  $\mathbf{v}$  vectors as:

$$u_x = \cos \lambda \sin \varphi - \sin \lambda \cos \varphi$$

$$u_y = -\cos \lambda \cos \varphi - \sin \lambda \cos \delta \sin \varphi$$

$$u_z = -\sin \lambda \sin \delta$$

And

$$v_x = \sin \delta \cos \varphi$$

$$v_y = \sin \delta \sin \varphi$$

$$v_z = -\cos \delta$$

where the  $\mathbf{t}$  and  $\mathbf{p}$  vectors are defined as  $\mathbf{t} = \frac{(\mathbf{v}+\mathbf{u})}{\sqrt{2}}$  and  $\mathbf{p} = \frac{(\mathbf{v}-\mathbf{u})}{\sqrt{2}}$ . To ensure the mutual orthogonality of all three axes, the unit vector  $\mathbf{b}$  is computed as the vector product of  $\mathbf{t}$  and  $\mathbf{p}$  for both cases 1) and 2). The  $\mathbf{T}$ ,  $\mathbf{P}$  and  $\mathbf{B}$  axes specify a rotated system of coordinates for the source,  $\mathbf{R}$ . We use the correspondence between the orthogonal matrix and the normalized quaternion (Moran, 1975; Altmann, 1986):

$$\mathbf{R} = \begin{vmatrix} t_1 & p_1 & b_1 \\ t_2 & p_2 & b_2 \\ t_3 & p_3 & b_3 \end{vmatrix} = \begin{vmatrix} q_0^2 + q_1^2 - q_2^2 - q_3^2 & 2(q_1q_2 - q_0q_3) & 2(q_1q_3 + q_0q_2) \\ 2(q_1q_2 + q_0q_3) & q_0^2 - q_1^2 + q_2^2 - q_3^2 & 2(q_2q_3 - q_0q_1) \\ 2(q_1q_3 - q_0q_2) & 2(q_2q_3 + q_0q_1) & q_0^2 - q_1^2 - q_2^2 + q_3^2 \end{vmatrix}$$

to obtain the quaternion's components.

If  $q_0$  is not close to zero

$$q_0 = \frac{1}{2}(t_1 + p_2 + b_3 + 1)^{1/2}$$

$$q_1 = \frac{(p_3 - b_2)}{(4q_0)}$$

$$q_2 = \frac{(b_1 - t_3)}{(4q_0)}$$

$$q_3 = \frac{(t_2 - p_1)}{(4q_0)}$$

That correspond to the rotation of a coordinates system connected with a double couple source from initial position into an arbitrary position. Since as many as three of the quaternion components may be close to zero, a simpler way to compute the components is to choose the component with the maximum absolute value and use it to calculate the remaining three components. Since a clockwise rotation is equivalent to a counterclockwise rotation about the same axis viewed from the opposite direction, to make the problem unique, we use only counterclockwise rotations corresponding to positive angles of rotation with a rotation pole distributed over the whole sphere. As a measure of the disorientation, we use the value of the rotation angle  $\varphi_k$ , which is necessary for rotating the focal mechanism from one position into another ( $0 \leq \varphi_k \leq \pi^\circ$ ). This angle depends on the degree of initial disorientation and on the symmetry of a rectangular box with unequal sides. The symmetries of the double couple make the orientation of a source non unique. The double couple focal mechanism can be rotated from one position into another by four different rotations (Kagan, 1991). To find the other rotations we multiply the normalized quaternion by  $\pm \mathbf{i}$ ,  $\pm \mathbf{j}$  or  $\pm \mathbf{k}$ . For example

$$\mathbf{q}' = \mathbf{q}\mathbf{i}$$

with  $\mathbf{i} = [0,1,0,0]$ . As a result of these multiplication, the quaternions components are permuted and change their sign. Quaternions of opposite sign correspond to the same rotation, we change the quaternions' sign so that its scalar part is positive, corresponding to the positive value of  $\varphi_k$ . The final result of all these four rotations is the same focal mechanism. We select the rotation which is the smallest rotation angle among the four rotations obtained. To find the minimum rotation of a double couple, we replace the quaternion's scalar component by the largest (in absolute value) among all of the components available,  $q_{max}$ , and then calculated the rotation angle  $\varphi_{kmin} = 2 \arccos q_{max}$ . Since largest of the four components of a normalized quaternion cannot be smaller than 0.5, the minimum rotation angle cannot exceed  $120^\circ$  (Kagan, 1991).

The rotation from one arbitrary position into another is more complicated to be computed. If one of the rotation angles is small, this rotation can be found relatively easily by trial-and-error. Averaging the positions of the **T**, **P** and **B** axes from several focal mechanism on a reference sphere, produces good estimates of an average mechanism and its variations for small rotations. On the other hand, if the rotations are large, we need to find all of the four rotations to be able to choose the smallest one. Moreover, straightforward averaging of the axes' positions becomes more questionable when the rotation angle approach 90° and we need to choose which of the two positions of any axis on the reference sphere is to be used. For example, we want to determine all possible rotations from one solution  $\pm q_1$  into  $\pm q_2$

$$q_2 = q'q_1$$

where  $q'$  is a quaternion corresponding to one of the rotations, transforming  $q_1$  into  $q_2$ . In terms of composition of rotations, the original quaternion [ 1,0,0,0] is firstly rotated by  $q_1$ , then by  $q'$  to obtain  $q_2$ . To determine  $q'$ , we can write

$$q' = q_2q_1^{-1}$$

To find three other solutions we multiply  $q_1$  or  $q_2$  by  $i$ ,  $j$ ,  $k$  and repeat the calculations.

## 1.2 EARLY WARNING SYSTEMS: FROM SCIENTIFIC FUNDAMENTALS TOWARD THE NEW GENERATION OF SYSTEMS

In the last two decades, the Earthquake Early Warning System (EEWS) has become one of the interesting topics for many seismologists around the world to reduce damage caused by earthquakes.

The earthquake warning systems can be classified in two main categories:

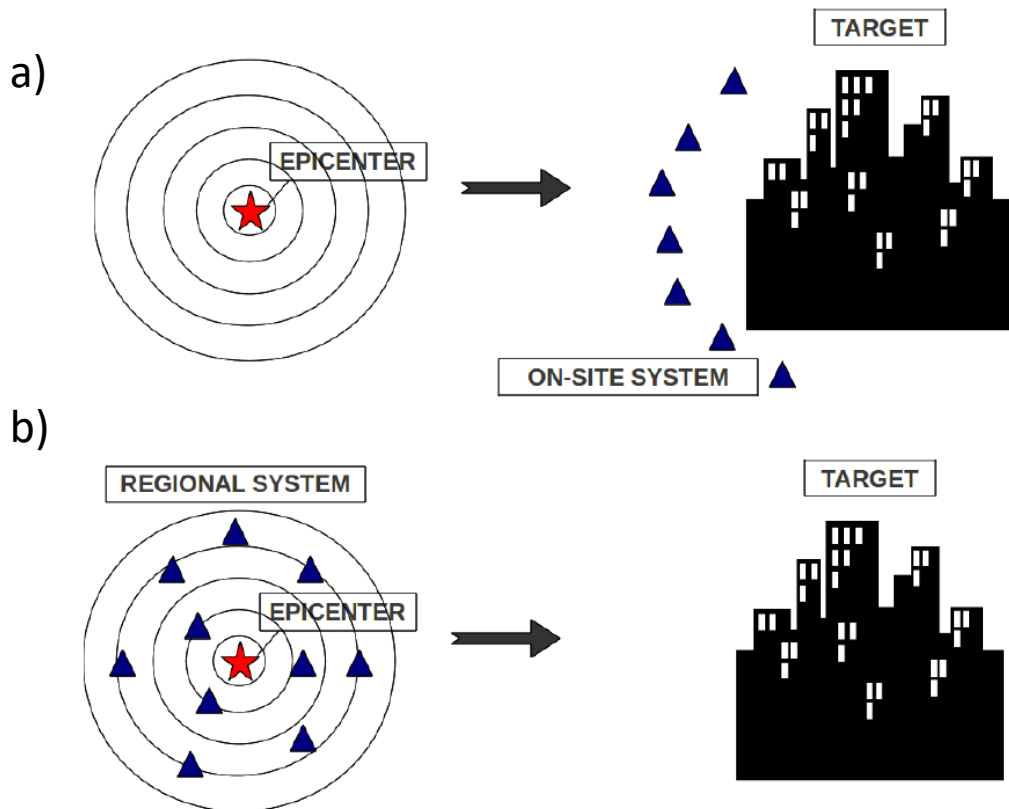


Figure 1.15: Earthquake Early Warning systems example: a) On-Site system: source and stations sites coincide; b) Regional system: stations are placed near the source region while targets are situated far away.

- 1) EEWS including On-site (or single station)
- 2) Regional (or network based). Regional systems include also Front detection (a kind of regional system based on a line).

The first kind of EEWS (*i.e.*, both On-site and Regional, Fig. 1.15) are following more rapid alternative strategies for earthquake risk mitigation, based on very short time scales (a few seconds to tens of seconds) *i.e.* the initial part of the P-waves. The front-detection systems are mainly used for those earthquakes located in the subduction zones or at a far distance from the targets (Fig. 1.16). An example is the Mexican Seismic Alert System, a front-detection system, in which the active seismic region is approximately located 300 km far from the city center. In fact, before issuing the alarm to the impacted zones, there is enough time to determine the required parameters such as expected amplitude vibration, magnitude and location of the event enough far-distance.

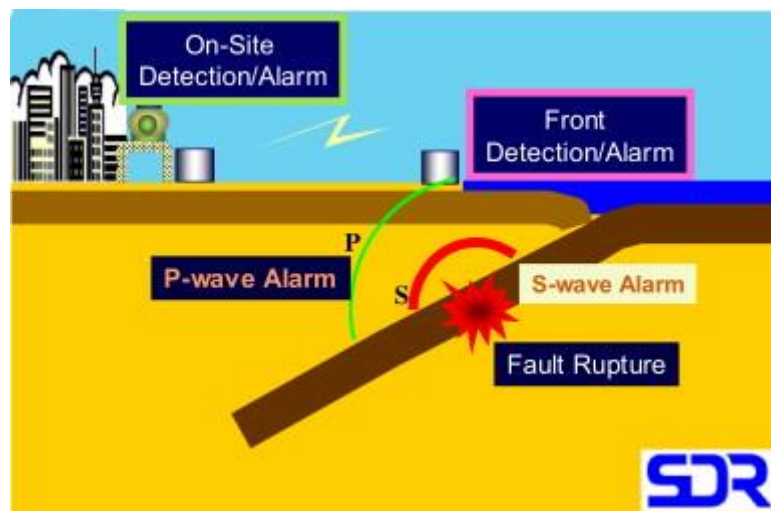


Figure 1.16: Concept of an earthquake early warning system (EEW) There are two types of EEW systems: (1) the Front detection/alarm and (2) the On-site detection/alarm; each of these can use two types of trigger: (a) the earthquakes' P wave, and (b) its S wave. Figure from Nakamura et al, 2011

EEWS is under development worldwide (already operational in Japan, Taiwan and Mexico, under development in California, southern Italy, Turkey and Romania), using real-time information about natural events which is provided by advanced monitoring infrastructures. However, the main conception of the EEWS refers to the optimal use of the few available data on the shortest possible time window to issue target warning several seconds before the arrivals of seismic waves (essentially surface waves) including damages in the target zone.

Most of the recent EEWS must work out in few seconds after the earthquake rupture nucleation and before the impact of waves including the devastating effect on population and buildings. Indeed, the EEWS represents the practical

implementation of Real-Time seismology concepts, methods and technologies. A Real-Time system is a protocol based on hardware devices controlled by software tools; it must react to an event before a well-defined deadline. The operational “deadline” of this system is related to the properties of the event being analyzed and the characteristics of the recording system. For seismic warning monitoring, the “deadline” is defined based on different quantities such as the length of a data packet in seconds, the minimum trace length required to measure a certain parameter (location, magnitude) in tens/hundreds of seconds, the number of triggered stations and the impact zone among other parameters. On the other hand, in seismic monitoring three concepts are often employed to describe the time efficiency of a system, as they are listed below:

1. Real-Time: the rapid system to react to an event (earthquake) within a given deadline; for instance, the data packet < 1 sec
2. Near Real-Time: the system is fast, but no deadline is set (the system can accumulate delays in special or critical conditions).
3. Off-Line: no constrain is set on the response time of the system.

For the real-time seismic risk mitigation, a useful approach is the development of EEWS which are automatic, real-time information systems able to detect an ongoing earthquake and broad-casting a warning in a target area, before the arrival of the most destructive waves (*Nakamura, 1984, 1988; Heaton, 1985; Teng et al., 1997; Wu et al., 1998; Wu and Teng, 2002; Allen and Kanamori, 2003*).

### 1.2.1 Network- and Station-based EEW Systems

In general, EEWS can be classified into two approaches as “Regional” or network-based, and “On-site” or a single station-based (*Nakamura, 1988; Caruso et al, 2017*). A regional EEWS is a network-based system integrating a dense seismic array deployed around the earthquake source zone and in this configuration the contents of the first few seconds of the P-waves are used to rapidly determine the magnitude and hypocenter of an earthquake. When a seismic event is detected, a regional system issues an alert for a wide epicentral area. The alert is generally based upon the estimation of the earthquake location and magnitude and previously known Ground Motion Prediction Equations (GMPEs; *e.g., Allen et al., 2009; Satriano et al., 2011*, among others). Furthermore, there are a few regional and/or multiple stations EEW algorithms that predict the ground motion level at target sites bypassing the source parameter estimation [*Hoshiba, 2013; Hoshiba*

and Aoki, 2015]. The region close to the source area, where the alert cannot be made available before the arrival of the dangerous seismic waves, is called the blind zone. Lead time is the time available for a mitigation action after the alarm whose definition differs for two types of EEW systems. In the network-based approach, Lead Time is the time difference between the first S-wave arrived at the target and the first P-wave recorded at the network, and it increases with the distance from the source, while in the on-site based systems, it is defined by the time difference between the first S-wave and P-wave arrived at the target, and it increases with a smaller distance comparing that one for the network-based EWS. In the case of a regional network, computational time can be longer than an on-site EEW (Fig. 1.15), but estimations on source parameters obtained by a multi-station network are more accurate than a single station network. *Stankiewicz et al.*, (2015) show that to have a more precise EEW system for events less than 60 km from the target, there should be a combination of both regional and onsite systems.

An on-site EEW is a stand-alone system based on a single sensor (or a small array of sensors) located in the proximity of the target to secure. In this configuration, the early P wave amplitudes and/or the characteristic frequency are used to predict the strong shaking associated with the late S and surface wave arrivals at the same site. This approach is particularly useful for sites located within the blind zone of a regional EEW system, allowing for a usable warning before the arrival of strong shaking waves. The P wave-based, on-site approaches use previously determined empirical relations to estimate the maximum ground-shaking amplitude, through the measurement of P-wave amplitude, frequency, integral of squared velocity, and other related quantities (*Kanamori, 2005; Wu and Kanamori, 2008; Böse et al., 2009; Zollo et al., 2010; Picozzi, 2012; Colombelli et al., 2015; Brondi et al., 2015*).

On the other hand, the maximum ground shaking can be predicted using the initial part of the P-phase amplitude and/or frequency content of each seismic station in the on-site method. Thus, precise determinations of the magnitude and hypocenter are not needed in an onsite application. In addition to these two main methods, a combination of these approaches is also available in the EEWS (*e.g., Picozzi et al., 2015*).

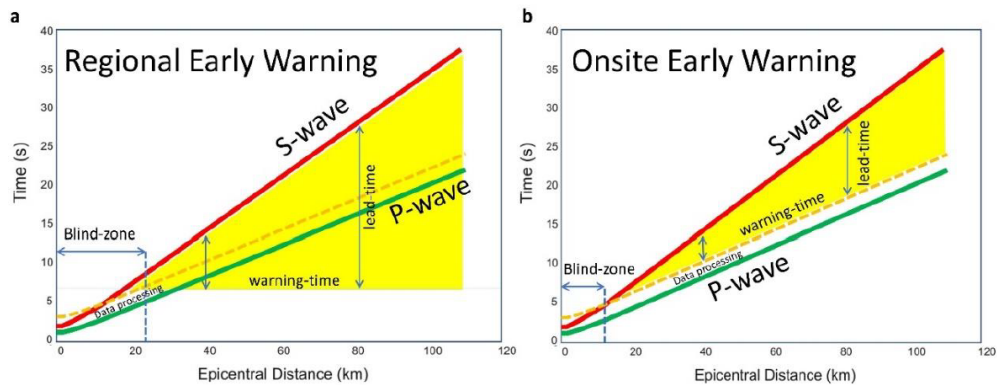


Figure 1.17: Warning- and Lead-time for **a.** network-based **b.** on-site systems.

## 1.2.2 The Next Generation of the EEW Systems

The technology on which EEW is based is still at the beginning. Estimation of all earthquake characteristics is mainly based on the initial part of the motions with rather non-negligible uncertainty. Simplifications of most processes and algorithms used in standard EEW approaches are a dominant part of computations to model the earthquake source and the related wave propagation. Just to list some critical points, the peak motion prediction in EEW methods is typically based on the point-source approximation and on 1D empirical attenuation relationships, depending on the magnitude and hypocentral distance. This representation became inadequate for large events ( $M > 6$ ) and may result in unreliable predictions of the expected shaking, thus reducing the efficacy of the EEW systems for those earthquakes producing extremely severe ground shaking. On average few portions of the P-waves, maximum 3 seconds, are used to real-time estimation of the event magnitude and location, which could be a problem for any calculation of the ground motion of large events, for which the source time function can last longer. In fact, the earthquake rupture process is the result of a complex combination of many factors, and the final magnitude depends on some average quantities of the whole process. In case of a large earthquake ( $M > 7$ ), tens of seconds are necessary for the whole process to be finished. The final goal of the next generation of EEW is to improve intensity measures by rapidly determining of magnitude and fault plane geometry, which are used to build simplified kinematic source models and then convolving with pre-computed Green's functions to provide complete wavefield synthetic seismograms. In this way, it is possible to provide early estimates of the expected intensity measures (Peak Ground Acceleration, PGA; Peak Ground Velocity, PGV) at the EEW target sites more reliable than those obtained modelling a point source. The alert

decision scheme is defined upon the exceedance of a user-compliant PGA or PGV threshold by the predicted synthetic values.

### 1.3 BACK PROJECTION

The basic idea behind the Back Projection (BP) methods is that each value of amplitude in the time of a seismic ground shaking record, observed at a certain station, is generated by a specific portion of the fault involved in the rupture process. So, if we back project on the source zone the information recorded at more stations, opportunely taking into account for the travel path, we will illuminate the portions of the fault gradually involved in the rupture process. Naturally, the more and more station records are available, the more it will be possible to constrain the portions of the fault that may have been involved in the process. While the noise is incoherent, the contributions of a source are consistent with each other and allow us to retrieve information about the source itself (Fig. 1.18).

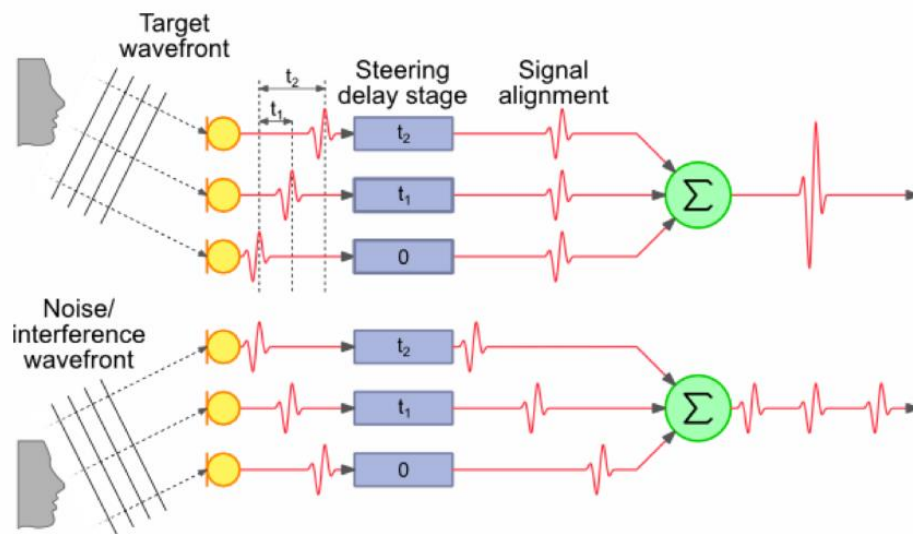


Figure 1.18: Stacking the noise not allows retrieving a coherent signal, while in presence of a real source the stacking process allows to retrieve the original source

To timely assess potential damages and manage post seismic operations, it is essential to characterize the rupture area of moderate to large earthquakes ( $M > 6$ ). BP has been widely used (Ishi, 2011; Maercklin et al., 2012; Kiser and Ishi, 2013, Meng et al, 2014) to obtain images of the rupture process of large earthquakes owing to the ever-increasing dense large-scale seismic networks. To summarize,

the BP technique allows imaging the spatial and temporal earthquake evolution based on the wave arrivals (Meng et al, 2014).

Traditionally BPs are performed at teleseismic distances because in this case seismograms at distances less than  $95^\circ$  present direct P and S waves arrivals relatively simple, while the seismograms at local distances are dominated by path effects through the crust with complex reverberations and in the regional distances' records are dominated by refracted and/or reflected waves by the crust-mantle discontinuity and inter crust (Zollo and Emolo, 2011).

We have deepened 2 different techniques:

- A beamforming and stacking BP approach that back projects the displacement amplitudes recorded at a local seismic network on the discretized fault plane to retrieve the slip rate in the time (Maercklin et al.,2012).
- A multi-array BP technique that uses the coherency between waveforms to locate the sub-sources intersecting the back-azimuth of more clusters, both for local or regional distances (Xie and Meng, 2020).

### 1.3.1 Beamforming and Stacking Back Projection for network

We worked at the development of a dedicated platform that develops beamforming and stacking technique to back-project at the local distance the direct S-wave recorded amplitudes into the source region, following the approach of Maercklin *et al.*, (2012). This work contributed to enrichment of the SERA (Seismology and Earthquake Engineering Research Infrastructure Alliance for Europe) Project for rapid kinematic rupture parameter estimation. The technique was applied by Maercklin et al., to S waves at local distances (from 100 to 420 km) for a giant earthquake (Mw 9.0, 2011 Tohoku, Japan), while here we try to apply it on local distance (<70 km) for moderate earthquakes. The slip imaging approach combines a spatial weighted estimate on where seismic energy is radiated with proper scaling of the recorded displacement amplitudes to recover the slip rate amplitude at the source as a function of space and time.

A flowchart of the procedure is shown in Fig. 1.17. Specifically, the procedure is structured as follows:

- Knowing the fault plane orientation, the earthquake source region is subdivided into a grid of small sub-sources, and for any given sub-source the delay times are computed to all seismic stations respect to a reference station (Fig. 1.20).
- The recorded amplitudes at all stations, within a time window bracketing the theoretical times, are summed using a weighted stacking to enhance coherent arrivals, and the obtained coherency value is assigned to the current sub-source. The time window for a single back-projection image is based on the period of the dominant phases. Repeating this process for all sub-sources provides the back-projected slip rate distribution in the earthquake source region at a given arrival time.

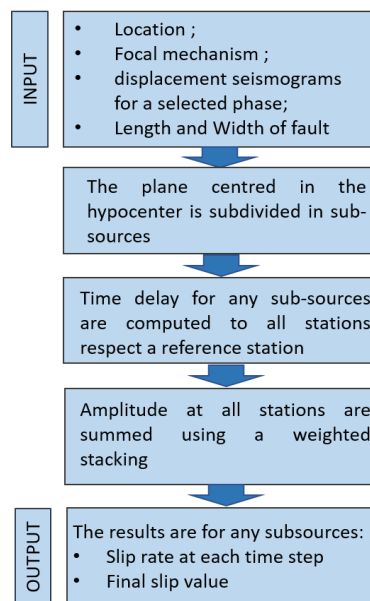


Figure 1.20: Scheme of the procedure by Maercklin et al., 2012

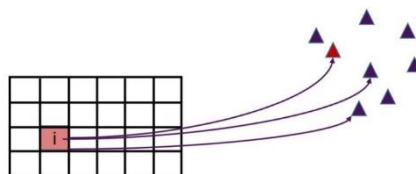


Figure 1.19: sketch of stacking amplitude backprojection: a plane oriented as the fault plane is subdivided in subsources.

- For the computation of the slip rate, the displacement amplitudes appropriately corrected by distance  $R_{ij}$  (the geometrical spreading) and radiation pattern  $F_{ij}$  for a constant focal mechanism are stacked and back projected for all possible elementary sources located along the fault surface. In fact for each sub-fault we can use the point-source approximation (paragraph 1.1.1). The resulting slip rate for the  $i$ -th grid point on the fault and at the time  $t$  is obtained as the summation:

$$\dot{S}_i(t) = \frac{2\pi\rho v_s^3}{\mu AN_s} \sum_{j=1}^{N_s} \frac{R_{ij}}{F_{ij}} U_j(t + t_i^R + \delta t_{ij}) \quad 1.6$$

where  $U_{ij}$  is the observed displacement at the  $j$ -th station,  $t_i^R$  the travel time to the reference station,  $\delta t_{ij}$  the time shift between the  $j$ -th station and the reference station,  $N_s$  the number of stations,  $\rho$  is the crustal density,  $v_s$  the S-wave velocity,  $\mu$  the shear modulus, and  $A$  the area of the sub-fault.

- We define an objective function for slip source location as the standard weighted back-projected stack amplitude for the  $i$ -th grid point and the time  $t$ :

$$W_i(t) = C(t) \left( \sum_{j=1}^{N_s} \text{sign}(U_j) \sqrt[n]{|U_j(t + t_i^R + \delta t_{ij})|} \right)^n \quad 1.7$$

which corresponds to the  $1/n$  quasi-norm of the displacement at all stations,  $n$  is set equal to 4 (Maercklin et al., 2012). The normalization factor  $C(t)$  ensures that the sum of  $W$  over all grid points is 1, so that the  $W$  function will be used as a spatial weighting function, assigning a larger value of slip rate to fault points where most likely high-radiating asperities were located.

- The slip rate map at the time  $t$  is obtained as the product  $W_i(t) \cdot S_i'(t)$ , while the integration of the slip rate over time provides the final slip map.

This approach guarantees that larger values of slip function will be retrieved in fault regions that are more likely to radiate seismic energy (Maerckin et al., 2012).

### 1.3.2 Multi Array Back Projection

The Multi Array BP approach was developed by Xie and Meng (2020) to estimate from S-wave at the local scale the location of sub-sources in order to release alert for early tsunami warning.

A flowchart of the technique is shown in figure 1.19.

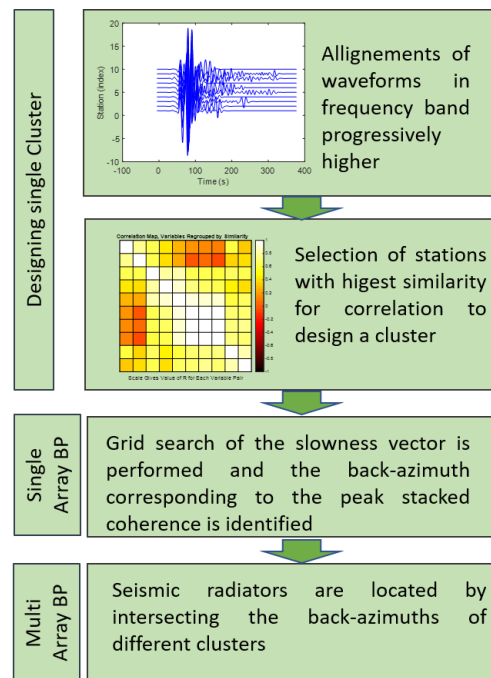


Figure 1.21: scheme of the technique of the Multi Array Back Projection developed by Xie and Meng (2020)

This technique is composed of 2 steps:

First, a single-cluster BP approach determines the locations of strong seismic radiations by analyzing a select wave train recorded by multiple local clusters of stations. The seismic radiators can be regarded as the centroid locations of seismic sub-events at different stages during an earthquake. In fact, differently from the

previous technique (Maerckling et al., 2012) in which the displacement amplitudes recorded at the stations were used to find the slip and slip rate on the fault plane, here we locate in space and in time the centroid of seismic sub-events of the earthquake. The source back-azimuths with respect to each cluster are calculated assuming plane wave arrivals. For a selected time-window, the source slowness vector is determined using the correlation stacking approach. This method beamforms the cross-correlation coefficients of all station pairs to improve the robustness against scattering, multipathing and contamination of coda waves (Frankel, 1991; Borcea et al., 2002; Fletcher et al., 2006; Meng et al., 2014). The coherence function  $C$  for the  $m$ -th cluster

$$C_m(t_0, \theta) = \sum_{i,j} cc_{ij}(t_0, \theta) = \sum_{i,j} \frac{\sum_{t=t_0-t_1/2}^{t_0+t_1/2} x_i(t - \tau_i(\theta))x_j(t - \tau_j(\theta))}{\sum_{t=t_0-t_1/2}^{t_0+t_1/2} (x_i(t)^2 x_j(t)^2)^{1/2}}$$

where  $i$  and  $j$  are the station index.  $cc_{ij}$  is the correlation coefficient between two stations.  $x_i$  is the seismogram.  $t_0$  is the time after the origin time.  $\tau_i(\theta)$  is the time delay compared to a reference station assuming the slowness vector is  $\theta$ . The sums in the equations are computed in a running time window of length  $t_1$  centered at  $t_0$ .

A grid search of the slowness vector is performed and the back-azimuth corresponding to the peak stacked coherence is identified.

The second step is to locate the seismic radiators by intersecting the back-azimuths in the source area (Figure 1.22). For each cluster, the possible source locations are along a vector pointing from the center of the cluster towards the back-azimuth. A Gaussian smoothing to this source location vector is applied to account for the uncertainty of the back-azimuths. The joint spatial probability distribution of the source location determined with multiple arrays is given by:

$$p(i, j, t) = \sum_{k=1}^n \exp \left[ -\frac{\theta_{T_k}(i, j) - \theta_{M_k}(t + t_{0_k})}{(2\sigma_k)^2} \right]$$

where  $i$  and  $j$  are the grid index,  $k$  is the cluster's index,  $t_{0_k}$  is the time after the origin time,  $\sigma_k$  is the Gaussian smoothing factor,  $\theta_{T_k}$  and  $\theta_{M_k}$  are the theoretical and measured back-azimuth, respectively and  $t_{0_k}$  is the theoretical arrival time of phase wave at the reference station. The source grid with the highest probability is considered as the location of the radiator at that time step.

In conclusion, we wanted to validate our results and to assess the usefulness of the information they reveal. Once the strong seismic radiators are located, we can use this information to make ground motion predictions. At this purpose, we used local GMPE to compute the 5% damping pseudo spectral acceleration (PSa). For the predicted pseudo spectral acceleration, we use the distance from stations to seismic radiators in GMPEs (Fig. 1.21) which include site effects and calibrated for each study region. The distance is computed as the minimum distance between the station and the seismic radiator.

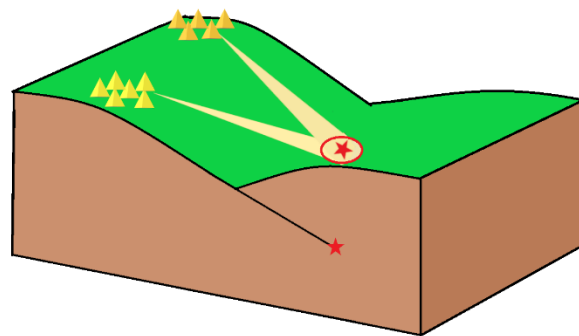


Figure 1.22 : Sketch of tracking earthquake with multi-array back-projection method. The red stars represent the hypocenter and epicenter. The earthquake rupture area (red ellipse) is imaged by the local seismic networks arrays (light and dark yellow tetrahedrons).

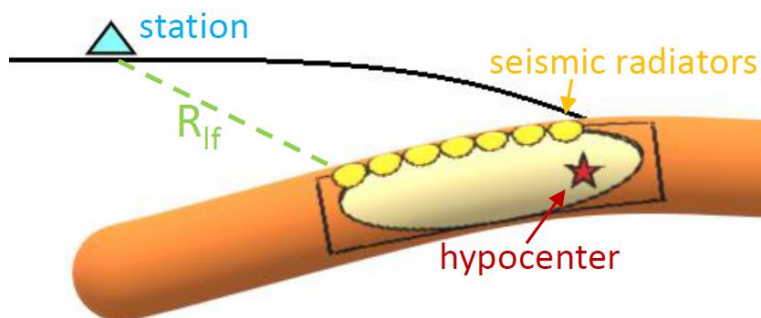


Figure 1.23: Scheme to represent the distance of a station to the nearest strong seismic radiators.

In fact, it has been demonstrated that it is possible to use the distance from seismic radiators to stations instead of the truncated Joyner-Boore (JB) distance in the Ground Motion Predicted Equations for teleseismic distances (Feng and Meng, 2018).

The root-mean-square error (RMSE) represents the average logarithmic residuals between model-predicted PSa with the data:

$$RMSE = \sqrt{\sum_{i=1}^n \frac{[\ln(PSa_i^{obs}) - \ln(\widehat{PSa}_i)]^2}{n}} \quad 1.7$$

$PSa_i^{obs}$  is the PSa measured from recording  $i$  and  $\widehat{PSa}_i$  is the corresponding value predicted by the GMPE, while  $n$  is the total number of available recordings.

We also compute PSa with the use of a truncated Joyner-Boore distance, measured as the closest distance to the fault portions that exceed the 20 % of peak slip, which reflects the slip distribution.

In particular, we computed PSa, PGV (Peak Ground Velocity) and PGA (Peak Ground Acceleration). The PGA was commonly used in engineering as a good determinant of buildings damage, especially for moderate earthquakes.

Wald et al. (1999) found that PGV correlates well with higher values of Modified Mercalli intensity (MMI), and Kaka and Atkinson (2004) similarly found good correlations between PGV and intensity in eastern North America. So, it has been shown PGV is an indicator of the potential of the ground motion to cause structural damage. While PGA and PGV are simple measures of a single peak, the PSa, instead, gives us information at different frequencies and represents the maximum acceleration response of an equivalent single degree of freedom systems. We use the Newmark Method for linear systems to compute the PSa (Chopra, 2001).

## 1.4 INVERSE METHODS

We define as Inverse Methods a set of methods (essentially numerical) that allow to extract information that are not directly measurable on a physical system starting from a set of data.

The two elements underlying the theory are the observations (data) and the model (described through a series of parameters) that expresses our knowledge of the physical system under study. The data can be direct or indirect measures of the properties of interest. For example, if we want knowing the thermal state of a system, we can perform direct temperature measurements. On the other hand, we can derive the propagation speed of the seismic waves starting from the indirect measurement of the arrival time of a given seismic phase. The model represents, in general, the link between the parameters describing the physical system and the data, and we usually express it in a mathematical relationship.

The solution of an inverse problem is often related to that of a problem direct. The terms 'direct' or 'inverse' basically indicate the direction of the passage from the data space to the space of the parameters of the model through the mathematical relationship that describes the model itself.

Most of data inversion methods implicitly include direct problem computation. In fact, the solution of the direct problem allows to determine a set of theoretical (or synthetic) data whose comparison with the real ones provides the basis for the estimation of the model parameters. The goal of inversion methods is not just to derive the best possible estimate of parameters of a model starting from the observations, but also be able to evaluate the goodness of the solution obtained in the terms of its uniqueness and which effect measurement errors have on parameter estimates, furthermore especially if, for a given geometry of acquisition, the data collected are sufficient to determine all the parameters and, in case not all of them can be determined, which ones can be estimated (resolution study).

### 1.4.1 Formulation of the inverse problem

The starting point is the description of the data and parameters of the model. Generally, the data represent a series of experimental measurements of one or

more variables. Suppose we perform  $N$  measurements on a particular physical system. It is possible to organize the measures in a matrix of dimensions  $N \times 1$  of the type:

$$\mathbf{d} = \begin{pmatrix} d_1 \\ \dots \\ d_N \end{pmatrix}$$

since, for subsequent applications, it is convenient to use matrix notation. The parameters of the model that characterizes the physical system are also arranged in a matrix of size  $M \times 1$  of the type:

$$\mathbf{m} = \begin{pmatrix} m_1 \\ \dots \\ m_M \end{pmatrix}$$

One intuitive and simple method to estimate the solution of an inverse problem is based on the evaluation of the difference between the datum and the theoretical estimate obtained of the datum itself, using a set of parameter values that define the model: the more the simulated value is close to the experimental one the more the parameters used to obtain the theoretical values provide a valid representation of reality. According to this, for any given data it is possible define a prediction error, or distance, between the theoretical estimate ( $d_{teo}$ ) and observation ( $d_{obs}$ ).

The solution of the inverse problem can therefore be obtained by searching for the parameters that minimize the sum of the absolute values or squares of the prediction error  $e_i = d_{obs}^i - d_{teo}^i$ .

The least squares method is based on the minimization of the function  $E = \sum e_i^2$ . The quantities  $e_i^2$  express the square of the Euclidean distance between observations and values predicted by the model. The prediction errors  $e_i$  are the components of the vector:

$$\mathbf{e} = \begin{pmatrix} e_1 \\ \dots \\ e_N \end{pmatrix}$$

The commonly used definitions of a vector norm are based on the sum of some power of the elements of the vector  $\mathbf{e}$ . Depending on the power value  $n$  used, the norm  $L_n$  is defined as:

$$\text{Norm } L_1: \|\mathbf{e}\|_1 = \sum |e_i|$$

$$\text{Norm } L_2: \|\mathbf{e}\|_2 = (\sum e_i^2)^{1/2}$$

$$\text{Norm } L_n: \|\mathbf{e}\|_n = (\sum e_i^n)^{1/n}$$

This  $E$  term can be considered as the  $L_2$ - norm of the vector  $\mathbf{e}$ . Since the inverse methods are based in any case on the principle of minimization of a norm, the definition of norm that is adopted takes on particular importance. In facts, if we choose a high-powered norm, we will give a greater importance to the data that strongly deviate from the predicted values (outlier) since, at the limit for  $n \rightarrow \infty$ , only the largest element of  $\underline{e}$  will have weight other than zero.

Choosing a low-order norm is equivalent to giving almost identical weight to the data, whatever their error of prediction. The least squares method uses a  $L_2$  norm. It is possible to verify that assigning a  $L_2$  norm is equivalent to assume a Gaussian distribution for the observations.

We can classify inverse problems in linear problems, if the mathematical relationship between data and model is linear, so that the operator which maps model parameters into the data that model predicts, defined as forward operator, is linear and non-linear problems, for which this operator is non-linear.

Moreover, we can classify problems in underdetermined if there are fewer equations than unknowns (fewer observations than model parameters) or overdetermined, for which there are more equations than unknowns. To easily interpretate this, we can think to the model parameters as available degree of freedom. Each observation introduces a constrain that restricts one degree of freedom. Since each measure is always affected by noise, we look for an approximate solution to the overdetermined systems.

## 1.4.2 Least squares solution

Methods for solving the following inverse linear problem:

$$\mathbf{d} = \mathbf{G}\mathbf{m}$$

where  $G$  is a forward operator, using the  $L_2$  norm are called least squares methods. The principle on which they are based consists in determining an estimate of the parameters of the model  $\mathbf{m}$  which minimizes the norm function

$$E = \sum_{i=1}^N |e_i|^2$$

To do this, it is necessary to calculate the derivatives of  $E$  with respect to each parameter of the model and equal them to zero. Explicitly, the vector:

$$\mathbf{e} = \mathbf{d} - \mathbf{G}\mathbf{m}$$

We have:

$$\begin{aligned} E &= \sum_{i=1}^N e_i^2 = \mathbf{e}^T \mathbf{e} = (\mathbf{d} - \mathbf{G}\mathbf{m})^T (\mathbf{d} - \mathbf{G}\mathbf{m}) \\ &= \sum_{i=1}^N \left[ d_i - \sum_{j=1}^M G_{ij} m_j \right] \left[ d_i - \sum_{k=1}^M G_{ik} m_k \right] \end{aligned}$$

Calculating the partial derivatives of  $E$  with respect to each parameter  $m_q$  and imposing that they are null, we arrive at a system of equations that is written in matrix notation:

$$\mathbf{G}^T \mathbf{G}\mathbf{m} - \mathbf{G}^T \mathbf{d} = \mathbf{0}$$

We note that, since  $\mathbf{G}$  is a matrix of order  $N \times M$ , the matrix  $\mathbf{G}^T \mathbf{G}$  is square of order  $M$ . Assuming that the determinant  $|\mathbf{G}^T \mathbf{G}| \neq 0$  and that the inverse matrix  $(\mathbf{G}^T \mathbf{G})^{-1}$  exists, the solution of previous equation is given by:

$$\mathbf{m}^{est} = (\mathbf{G}^T \mathbf{G})^{-1} \mathbf{G}^T \mathbf{d}$$

which represents the least squares solution of the inverse linear problem  $\mathbf{d} = \mathbf{G}\mathbf{m}$ . In general we define the generalized inverse matrix  $\mathbf{G}^{-g}$  as the matrix that allows us to write the solution to the inverse problem as:

$$\mathbf{m}^{est} = \mathbf{G}^{-g} \mathbf{d}$$

In the case of the least squares solution, the generalized inverse matrix is given by:

$$\mathbf{G}^{-g} = (\mathbf{G}^T \mathbf{G})^{-1} \mathbf{G}^T$$

### 1.4.3 Estimation of the error associated with the least squares' solution

Let us imagine that we can ideally represent the function in a graph:

$$e^T e = E(m_1, \dots, m_N) = \sum_i \left( d_i - \sum_j G_{ij} m_j \right)^2$$

by varying all the possible models that would be obtained by varying the parameters, each in the own maximum variation range. This function, in the multi-dimensional space of parameters, generally has a complex form that essentially depends on the degree of constraint that the data provide to the various parameters, which in turn is dependent on the acquisition geometry some data. The least squares solution represents the point in the parameter space for which the function  $E$  is minimum.

For example, in the case of two parameters, if the problem is overdetermined, they are both solvable. Conversely, if the problem is underdetermined one of the

two parameters, for example  $m_1$  is not solved while  $m_2$  is solved. A problem is then completely undetermined if the parameters  $m_1$  and  $m_2$  are correlated and therefore the value of  $m_1$  depends on that of  $m_2$ . Ideally, the graph of the function  $E$  allows us to obtain all the information about the ability of the data to resolve parameters.

If the problem is strongly nonlinear, it is highly likely that there are more minima than the function  $E$  associated with different parameter values. Let us consider an overdetermined problem that presents a single minimum of the function  $E$  (unique solution) and for simplicity

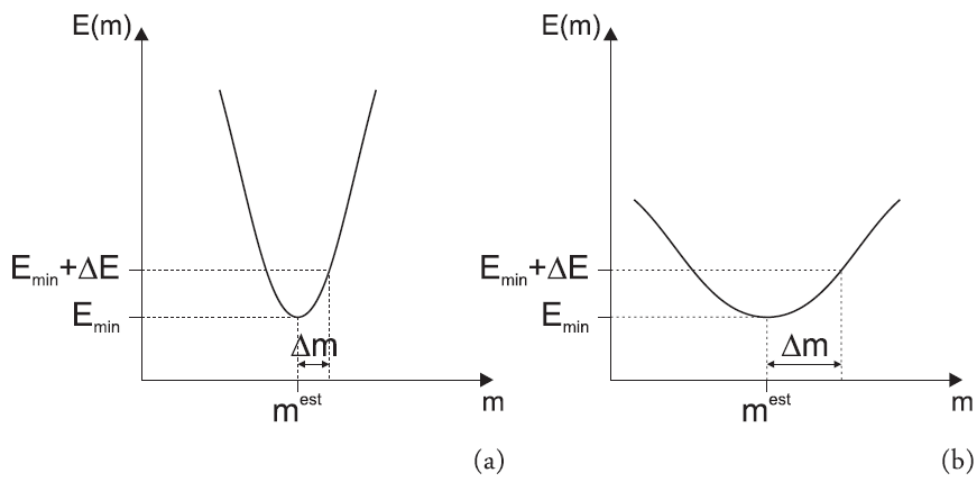


Figure 1.24: (a) The best estimate  $m^{est}$  of the parameter  $m$  is found in correspondence with the minimum of the function  $E(m)$ . If in proximity of the minimum this function is relatively narrow, then the fluctuations of  $E(m)$  give errors  $\Delta m$  on  $m^{est}$  which are small. (b) If the function  $E(m)$  is instead large around the minimum, the error on  $m^{est}$  becomes large.

we consider the case of a problem with only one parameter. The best estimate of the parameter (the one obtained for example with least squares) is the one corresponding to the minimum of function  $E$ . We establish an arbitrary variation  $\Delta E$  around the minimum. The line  $E = E_{min} + \Delta E$  intersects the curve  $E(m)$  (Figure 1.24). Likewise of variation  $\Delta E$ , depending on the shape of the function  $E$  around the minimum, we obtain a variable range of the parameter (parameter error). It seems intuitive that more the curve  $E(m)$  is tight around the minimum the smaller the error on the estimated parameter. The error on the parameters of the model can then be evaluated by studying the shape of the function around it

and therefore through the calculation of the second derivative of the function  $E$  calculated in the minimum.

The error and correlations between the parameters are described by the covariance matrix:

$$cov(\mathbf{m}) = \begin{pmatrix} \sigma_{11} & \dots & \sigma_{1N} \\ \dots & \dots & \dots \\ \sigma_{M1} & \dots & \sigma_{MN} \end{pmatrix}$$

The diagonal of the covariance matrix expresses the error (square of the standard deviation) on each parameter, while the off-diagonal elements are the correlation coefficients between the parameters. The least squares solution is associated with the covariance:

$$cov(\mathbf{m}) = \sigma_d^2 [\mathbf{G}^T \mathbf{G}]^{-1}$$

where  $\sigma_d$  is the error (standard deviation) on the data, assuming a single constant data variance  $\sigma_d$ . The matrix  $\mathbf{G}$  determines completely the "map" of the errors on the parameters. There is a relationship between the second derivative of the error function  $E$  and the covariance matrix. Indeed, it is shown that:

$$\frac{1}{2} \frac{\partial^2 E}{\partial \mathbf{m}^2} = \mathbf{G}^T \mathbf{G}$$

And then

$$cov(\mathbf{m}) = \sigma_d^2 [\mathbf{G}^T \mathbf{G}]^{-1} = \sigma_d^2 \left[ \frac{1}{2} \frac{\partial^2 E}{\partial \mathbf{m}^2} \right]_{\mathbf{m}=\mathbf{m}^{est}}^{-1}$$

Consequently, small values of the second derivative of  $E$  (slight variations in shape around the minimum) produce large values of variance (errors) in the solution.

## 1.4.4 Linearization of inverse methods

Let us assume to have the non-linear problem:

$$\mathbf{d} = \mathbf{G}(\mathbf{m})$$

One possible approach to solve this problem is to make it locally linear, ie in a neighbourhood of a point. We can write:

$$\mathbf{d} = \mathbf{G}(\mathbf{m}_0) + \frac{\partial \mathbf{G}}{\partial \mathbf{m}} \delta \mathbf{m}$$

In this case the problem is linear in the neighbourhood of the point  $\mathbf{m}_0$ . In fact, we can write:

$$\mathbf{d} - \mathbf{G}(\mathbf{m}_0) = \mathbf{A} \delta \mathbf{m}$$

Where  $A_{ij} = \frac{\partial G_i}{\partial m_j}$ . If the function  $\mathbf{G}$  is analytically defined, then the matrix  $\mathbf{A}$  is exactly known; otherwise, it can be obtained deriving numerically  $\mathbf{G}$ . In this way, starting from an initial model  $\mathbf{m}_0$ , it is possible to get the solution  $\mathbf{m}_1$  of the linearized inverse problem. Probably the solution  $\mathbf{m}_1$  will not be the true solution.

However, it is possible to obtain, using  $\mathbf{m}_1$  as the initial model, a new solution to the problem which will be better than the previous one. This procedure is repeated iteratively until the solution obtained is not sufficiently accurate in the sense that the misfit assumes values lower than a given threshold selected a priori. Ultimately, by means of the linearized approach, the inverse non-linear problem is reduced to a series of linear problems solved in succession.

## 1.4.5 Non-linear Inverse method

If the equation

$$d = G(m)$$

is strongly non-linear, the linearization approach is completely unusable. In fact, a strongly non-linear function is often multimodal and, if the initial model is chosen around, for example, a relative minimum, the linearized solution will tend to converge towards it. From a purely conceptual point of view, non-linear inverse methods are more simplistic than linearized ones: in fact, they aim to find the model that best justifies the observed data by minimizing the distance between these and the theoretical ones envisaged based on the model. The cost function (misfit)  $E$  is a measure of this deviation. The optimization methods of the cost function are therefore placed at the expense of non-linear inverse methods.

The search for the absolute minimum of a function is a problem whose difficulty essentially depends on the shape of the function to be optimized, i.e., on the fact that it possibly has more relative minima, perhaps comparable with the absolute one. The optimization methods are divided into local and global. The former ones provide that, starting from an initial point, one progressively moves towards the areas where the function takes on lower values. These methods can be classified, based on the type of information used, in:

- methods using the gradient of the function; these methods in practice calculate the fastest descent direction along the function and, obviously, they can be used only when the function is sufficiently smooth otherwise there is a high probability of being trapped in a relative minimum;
- methods that use only the value of the function; these methods are preferably used when the calculation of the gradient of the function is complicated or in any case expensive.

The local search methods are quite sensitive to the presence of relative minima. Global optimization methods, on the other hand, explore the function to be optimized more broadly, less affected by the presence of relative minima.

For global search there are more algorithms. The first is a grid-search algorithm which consists of a succession of calculations of the equation in nested and increasingly finer grids within a three-dimensional volume. This algorithm requires very long calculation times but on the other hand it guarantees systematic and exhaustive coverage of solutions space and is also able to identify different optimal solutions and confidence volumes highly irregular.

The second approach is based on the Metropolis-Gibbs algorithm: a path is executed in the space of solutions which tends towards the regions of the rough space likelihood for the Probability Density Function. At each iteration, the current position of solution  $m^{curr}$  is perturbed of a quantity, having arbitrary direction and fixed modulus, thus obtaining the new one position at which the probability density is evaluated.

If the probability density function is higher, the new position  $m^{new}$  is accepted immediately; otherwise, the new position is accepted with a probability normalized by the previous value  $p = \sigma^p(m^{new})/\sigma^p(m^{curr})$ . This algorithm works very well for moderately irregular PDFs and is only slightly slower (about 10 times) than the techniques localization iteratives based on a linearized approach while it is much faster than the grid-search.

Another available search algorithm is known as Oct-Tree (Fang et al., 1996). It uses recursive subdivisions of three-dimensional space and a density of the cells which is directly related to the value of the Probability Density Function. The algorithm is initialized with a global sampling of the entire space of research carried out with a thin grid. The value of the probability density function is then calculated at center of each cell and the cell with the highest probability value is subdivided into smaller cells and the process is iterated. This recursive procedure converges very rapidly producing a structure that has a greater number of cells in the space regions characterized by the highest Probability Density Function values (Figure 1.25).

## Oct-Tree sampling procedure

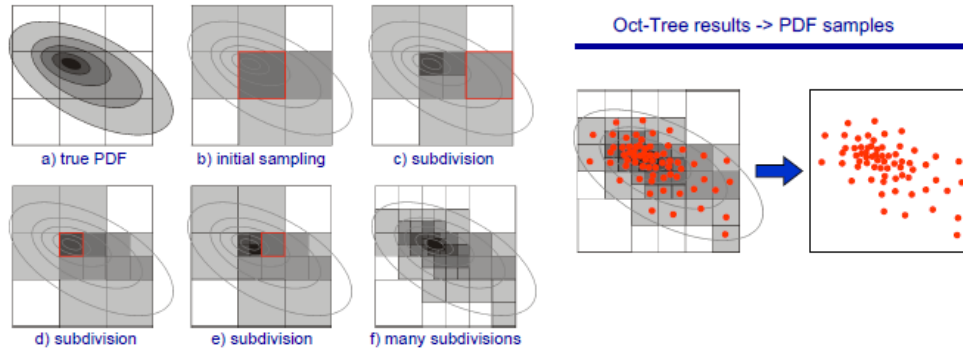


Figure 1.25: The Oct-Tree search algorithm starts from a subdivision of the space that is not very dense and then refines the search through recursive subdivisions of cells with higher PDF values. The samples corresponding to each cell of the structure provide a useful and compact representation of the probability density function. Figure taken from A. Lomax and A. Curtis (2001)

## 2 METHODOLOGY FOR FOCAL MECHANISM ESTIMATION

---

### 2.1 OFFLINE APPLICATION

In this section we will describe the general methodology for offline application to retrieve a focal mechanism.

We want to infer the model parameters  $\mathbf{m}$  (strike  $\phi$ , dip  $\delta$  and slip  $\lambda$ ) which describe an earthquake focal mechanism from a dataset  $\mathbf{d}$ , composed by 3 different and independent datasets, which are the P-wave absolute amplitude  $\mathbf{d}^A$ , the P-wave polarity  $\mathbf{d}^P$  and the S-wave-P-wave amplitude ratio  $\mathbf{d}^R$  and will fourthly be explained later. The data are the measures of physical quantities, which are related to the model parameters through general *nonlinear theoretical relationships*, so that the problem we want to solve is:

$$G(\mathbf{m}) = \mathbf{d}$$

where  $G$  is a forward operator. Let us assume a Bayesian approach (Tarantola, 1987) in which the model  $\mathbf{m}$  is a random variable, the solution is a probability density function for the model parameters.

We will denote the prior distribution by  $\rho(\mathbf{m})$  and we will use the notation  $f(\mathbf{d}|\mathbf{m})$  for the data conditional probability density function. The posterior probability density function for the model parameters is given by:

$$q(\mathbf{m}|\mathbf{d}) = cf(\mathbf{d}|\mathbf{m})\rho(\mathbf{m})$$

where  $c$  is a normalization constant,  $c = \int_{all\ models} f(\mathbf{d}|\mathbf{m})\rho(\mathbf{m})d\mathbf{m}$ . We refer to the maximum of the posterior probability distribution  $q(\mathbf{m}|\mathbf{d})$ , that is the most likely parameters model, as the maximum a posteriori (MAP) model (Aster et al,2013).

In our case study, we will consider an uninformative prior distribution in which all model parameters values have equal likelihood, for instance  $\rho(\mathbf{m}) = constant$ . Given this choice, we have:

$$q(\mathbf{m}|\mathbf{d}) = cf(\mathbf{d}|\mathbf{m})$$

and the posterior distribution is the likelihood function  $L(\mathbf{m}|\mathbf{d})$ . Under the maximum likelihood principle, we would select the model that maximizes  $L(\mathbf{m}|\mathbf{d})$ , that is the MAP model.

As briefly mentioned above, in our study case, we have 3 independent data sets, the P-wave absolute amplitude  $\mathbf{d}^A$ , the P-wave polarity  $\mathbf{d}^P$  and the S-wave-P-wave amplitude ratio  $\mathbf{d}^R$ . We can write:

$$f(\mathbf{d}|\mathbf{m}) = f(\mathbf{d}^A \cap \mathbf{d}^P \cap \mathbf{d}^R|\mathbf{m}) = f(\mathbf{d}^A|\mathbf{m}) * f(\mathbf{d}^P|\mathbf{m}) * f(\mathbf{d}^R|\mathbf{m})$$

where  $\cap$  indicates the intersection, while  $*$  the product. Let us assume the noise in the measured amplitude is independent and normally distributed with standard deviation  $\sigma$ . Because the measurement errors are independent, we can write the likelihood function as the product of the likelihoods of the individual data points:

$$L(\mathbf{m}|\mathbf{d}^A) = f(\mathbf{d}^A|\mathbf{m}) = \prod_{i=1}^N f(d_i^A|\mathbf{m})$$

Because the individual data points  $d_i^A$  are normally distributed with expected values  $G(\mathbf{m})_i^A$  and standard deviation  $\sigma$ , we can write:

$$f(\mathbf{d}^A|\mathbf{m}) = \left(\frac{1}{\sigma^A \sqrt{2\pi}}\right)^{N^A} e^{-\sum_{i=1}^{N^A} \frac{(G(\mathbf{m})_i^A - d_i^A)^2}{2\sigma^A{}^2}}$$

It is possible to apply nonlinear regression when the measurement errors are independent and normally distributed, and the standard deviations are unknown but assumed to be equal.

Considering  $\sigma^A$  are unknown, we can write weighted residuals  $r_{wi}^A$  as:

$$r_{wi}^A = \frac{d_i^A - G(\mathbf{m})_i^A}{\sigma^A} = d_{wi}^A - G(\mathbf{m})_{wi}^A$$

while the weighted standard deviations are:

$$s_W^A = \sqrt{\frac{\sum_{i=1}^{N^A} r_{wi}^A{}^2}{N^A - N^m}}$$

where  $N^m$  is the number of model parameters. For an homogeneous, isotropic and infinite medium, the P-wave displacement observed amplitude at a station  $i$  is given by (Aki & Richards,1980):

$$u_i(t) = \alpha \frac{R_i^{\theta\varphi} \dot{M}(t)}{r_i}$$

With  $\alpha$  equal to a constant depending on the velocity wave velocity and the density of the medium,  $r_i$  considering the distance,  $R_i^{\theta\varphi}$  is the radiation pattern depending by take-off angle  $\theta$  and azimuth angle  $\varphi$ , while  $\dot{M}(t)$  is the derivative of the seismic moment.

At a fixed time  $t_0$  we have

$$u_i(t_0) = \alpha \frac{R_i^{\theta\varphi} \dot{M}(t_0)}{R_i}$$

And, similarly, for velocity at a fixed time  $t_0$

$$\dot{u}_i(t_0) = \alpha \frac{R_i^{\theta\varphi} \ddot{M}(t_0)}{R_i}$$

As well as for acceleration.

Let consider  $N^A$  stations, we have  $\dot{u}_i$  with  $i=\{1, \dots, N^A\}$ .

We remove the dependence by the distance using pre-computed local empirical relationships between the P-wave peak amplitude and distance. The general form of these empirical relationships is:

$$\log_{10}(P_*) = a + b M + c \log_{10}(dist)$$

where  $P_*$  is for  $P_A$ ,  $P_V$  or  $P_D$ , while  $M$  is the moment magnitude,  $dist$  is the hypocentral distance and  $a, b$  and  $c$  are empirical constants. In our case, for a fixed event, the moment magnitude is the same for all the stations and its effect will be corrected thanks to the normalization of the P-wave amplitudes to the maximum observed P-wave amplitude corrected for the distance.

The correction for the distance that we implement is:

$$P_*^c = 10^{(\log_{10}(P_*) - c \log_{10}(dist))}$$

So, we have:

$$u_i^c(t_0) = \alpha' R_i^{\theta\varphi} \dot{M}(t_0)$$

Let  $i_{max}$  be the station with maximum corrected amplitude  $u_i^c(t_0)$ , we can write:

$$\frac{u_i^c(t_0)}{u_{i_{max}}^c(t_0)} = \frac{\alpha' R_i^{\theta\varphi} \dot{M}(t_0)}{\alpha' R_{i_{max}}^{\theta\varphi} \dot{M}(t_0)} = \frac{R_i^{\theta\varphi}}{R_{i_{max}}^{\theta\varphi}}$$

So we will have our data in amplitude at the station i is given by:

$$d_i^A = \left| \frac{u_i^c(t_0)}{u_{i_{max}}^c(t_0)} \right|$$

We will compare it with the theoretical amplitude in absolute value for a given triplet of focal mechanism angles  $(\lambda, \delta, \varphi)$  and similarly normalized:

$$u_i^{th} = \left| \frac{R_i^{\theta\varphi}(\lambda, \delta, \varphi)}{R_{i_{max}}^{\theta\varphi}(\lambda, \delta, \varphi)} \right|$$

Therefore, in our case we will have:

$$G(\bar{m})_i^A = G(\lambda, \delta, \varphi)_i^A = \left| \frac{R_i^{\theta\varphi}(\lambda, \delta, \varphi)}{R_{i_{max}}^{\theta\varphi}(\lambda, \delta, \varphi)} \right|$$

Regarding the conditional probability density function associated with S-wave/P-wave ratio  $f(\bar{d}^R | \bar{m})$ , we can do same considerations as for P-wave amplitudes, that means thanks the fact that individual data points  $d_i^R$  are normally distributed with expected values  $G(\bar{m})_i^R$  and standard deviation  $\sigma^R$ , we can write:

$$f(\bar{d}^R | \bar{m}) = \left( \frac{1}{\sigma^R \sqrt{2\pi}} \right)^{N^R} e^{-\sum_{i=1}^{N^R} \frac{(G(\bar{m})_i^R - d_i^R)^2}{2\sigma^R{}^2}}$$

We have in a homogeneous, isotropic and unlimited medium

$$\frac{u_i^S(t_0)}{u_i^P(t_0)} = \frac{R_i^{\theta\varphi S}}{R_i^{\theta\varphi P}} * \frac{\alpha_s^2 \alpha_r}{\beta_s^2 \beta_r}$$

Where  $\alpha_r$  and  $\alpha_s$  are respectively the P-wave velocity at receiver and source, and  $\beta_r$  and  $\beta_s$  similarly for S-wave velocity. So that  $d^R$  at a station k is:

So that  $d^R$  at a station k is:

$$d_k^R = \left| \frac{u_k^S(t_0)}{u_k^P(t_0)} \right| * \frac{\beta_s^2 \beta_r}{\alpha_s^2 \alpha_r}$$

The theoretical ratio r for a given triplet given triplet  $\lambda, \delta, \varphi$  in the model space at a station k is:

$$G(\bar{m})_i^R = r_k^{th} = \left| \frac{R_k^{\theta\varphi S}(\lambda, \delta, \varphi)}{R_k^{\theta\varphi P}(\lambda, \delta, \varphi)} \right|$$

The theoretical polarity for a given triplet  $\lambda, \delta, \varphi$  in the model space at a station j is defined as the sign of the radiation pattern for a given triplet  $\lambda, \delta, \varphi$ :

$$u_j^{P th} = \text{sign}[R_j^{\theta\varphi}(\lambda, \delta, \varphi)]$$

Regarding the conditional probability density function associated with polarities  $f(\bar{d}^P | \bar{m})$ , we use the formulation proposed by Brillinger (1980):

$$f(\bar{d}^P | \bar{m}) = \prod_j^{N^P} \frac{1}{2} * [1 + (1 - 2\gamma_j) * \text{erf}(\rho_0 | R_j^{\theta\varphi}(\lambda, \delta, \varphi)) * u_j^{P th} * d_j^P] \quad 2.1$$

with erf that is the error function. The quantity in the square brackets represents the probability that the j-th observed polarity  $d_j^P$  is consistent with the polarity predicted by the model  $\bar{m}$ . The expression of this probability density function is complicated because we want to represent in a continuous way the information provided by the polarities, which are discrete quantities. The transition between the zones with positive, negative and null polarity values is given by the factors  $\rho_0$  and  $\gamma_j$  which are the parameters that control the shape of the probability density function  $f(\bar{d}^P | \bar{m})$ . The values of  $\rho_0$  and  $\gamma_j$  vary respectively between  $[0, \infty)$  and  $[0, 1/2]$ . For imprecise polarities data,  $\gamma_j$  is near 0.5 or  $\rho_0$  near 0, precise data correspond to small  $\gamma_j$  and large  $\rho_0$  ( $\rho_0 > 0$ ).

The meaning of this formulation is that larger is the radiation pattern  $R_j^{\theta\varphi}(\lambda, \delta, \varphi)$ , higher is the probability to measure the right polarity.

The posterior probability  $q(\bar{m} | \bar{d})$  is given by:

$$q(\bar{m}|\bar{d}) = kf(\bar{d}^A|\bar{m}) * f(\bar{d}^P|\bar{m}) * f(\bar{d}^R|\bar{m})$$

with k constant of normalization.

We look for the MAP model of the posterior probability distribution. However, the availability of the a posteriori probability distribution allows quantifying the uncertainty level associated with the MAP model. For example, we compute the 68% Bayesian confidence interval, and we compute the covariance matrix. Diagonalizing this matrix, we can find its eigenvalues and eigenvectors. Then, we can project the half-axes of the 68% confidence ellipsoid, centred on the MAP model, onto the dimensions of strike, dip, slip, and find the solution uncertainties. We can also provide 68% range interval around MAP model inferred from single parameter marginal distributions.

The block diagram of the algorithm is shown in figure 2.1.

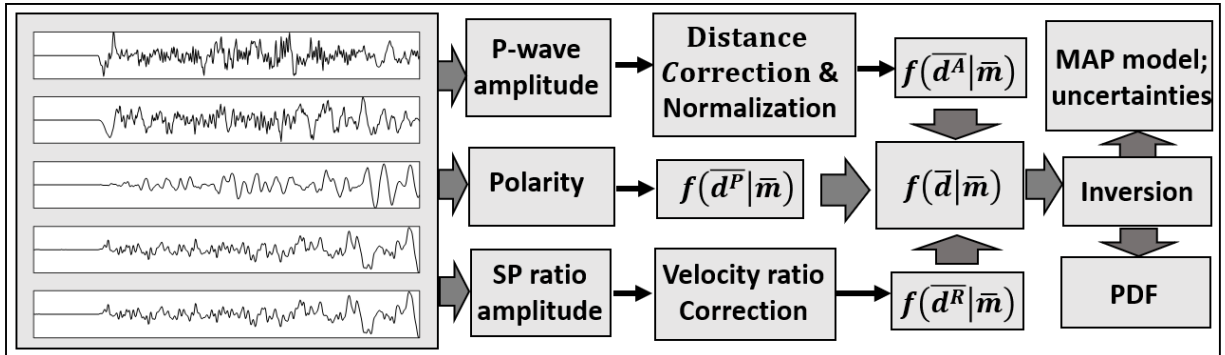


Figure 2.1: Block diagram of the algorithm. The algorithm can work with multiple datasets with their own processing to get data conditional probability functions, which combined together provide the data conditional probability function of the entire problem and which thanks to the inversion provides PDF, MAP model and model parameters uncertainties.

## 2.2 REAL TIME APPLICATION WITH EVOLUTIONARY APPROACH

In the case of application in real-time, we used the algorithm in an evolutionary approach (Tarantino et al., 2019) in which the input parameters are estimated in

different and progressively expanded P-wave time windows and data are included as they become available at the recording network. In this way, at each time, all the available records are used with a different time window depending on the P-wave arrival time and on the S-P travel-time difference. This strategy allows the number of stations that contributes to the solution to increase with time while the risk of any S-wave contamination is as low as possible. At the first iteration, we can either use an uninformative prior probability density function (PDF) or define a specific one, based for instance on available tectonic information of study area. At each following step the posterior probability density function, that we obtain solving the inverse problem of the previous step, will be used as prior distribution for the successive timestep and so on for later iterations until a convergence condition is satisfied.

A flowchart showing the basic working of this approach in an evolutionary mode is plotted in figure 2.2. Our input data are the initial P-wave peak amplitudes, which correspond to the maximum absolute amplitude values of measured displacement, velocity, and acceleration (Pd, Pv, and Pa, respectively). The three parameters are measured on the vertical component of the ground motion in progressively expanded P-wave time windows, starting from the arrival of the P wave and stopping at the expected arrival of the S waves. We use for the sequence of central Italy, that is for moderate earthquakes, a P-wave time window of 1, 2, or 3 s, depending on the hypocentral distance (1 s for hypocentral distance less than 25 km, 2 s for hypocentral distance between 25 and 30 km and 3 s for larger distances). We then apply a set of empirical corrections to the recorded data, to compare the observed P-wave amplitude distribution to the theoretical shape of the P-wave radiation pattern. Specifically, to account for the path attenuation effect, we correct each parameter using precomputed empirical scaling relationships between the P-wave peak amplitude, magnitude, and hypocentral distance. Finally, we normalize the observed P-wave peak parameters to their maximum value (Pd, Pv, and Pa are independently normalized) and then we take their mean.

At each iteration, the convergence of the solution is evaluated by comparing the current solution ( $\overline{m}_i$ ) at the timestep  $i$  to the most likely triplet at the previous step ( $\overline{m}_{i-1}$ ) requiring that:

$$\delta\overline{m} = \frac{\|\overline{m}_i - \overline{m}_{i-1}\|}{\|\overline{m}_{i-1}\|} < \varepsilon \quad 2.2$$

in which  $m = [\text{strike, dip, slip}]$  and we fixed  $\varepsilon=0.05$ . The convergence is declared if the condition in equation (2.2) is continuously satisfied for a 3 s wide time window.

We provide the MAP model as solution and the semi-axes length of the 68% confidence ellipsoid centered on the MAP model as uncertainties.

In order to evaluate the consistence of an obtained solution with this approach respect to a reference, we provide the Kagan's angle (KA). KA measures the minimum angle to rotate one mechanism into another, or in simpler words, the smallest angle between the slip vectors of two FMs. The smaller the KA, the more similar are the two FMs, with KA equal to zero in the case of two identical FMs (Sokos and Zahradník, 2008; Michele et al., 2014).

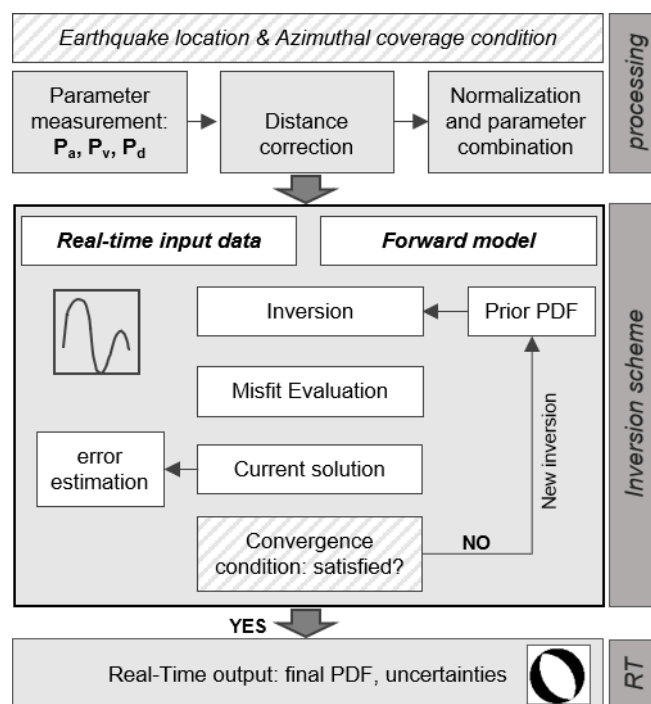


Figure 2.2: Block diagram of the algorithm. The figure describes the block diagram of the algorithm, which starts working as soon as the earthquake location is available, and an azimuthal coverage condition is satisfied. The preliminary data processing includes the parameters measurement, the correction for distance, the normalization, and linear combination. The final solution is declared when a convergence condition is satisfied. PDF, probability density function; RT, real time.

## 3 APPLICATION OF METHODOLOGY OF FOCAL MECHANISM ESTIMATION

---

### 3.1 EVOLUTIONARY APPROACH IN SIMULATED REAL TIME

In Tarantino et al. (2019) we firstly introduced an approach for the automatic determination of the earthquake focal mechanism, using the spatial distribution of observed absolute initial P-wave peak amplitudes, corrected for the distance attenuation effect, in an evolutionary, Bayesian framework. This quantity contains information about the radiation pattern of P-wave. Of course, the shape of the radiation pattern can be affected by some effect, as i.e., the directivity which can amplify one lobe rather than another, however the position of the lowest value (close to the nodal planes) and of the maxima is not affected. We applied the proposed methodology to the main earthquakes of the 2016–2017 central Italy seismic sequence finding that our rapid automatic estimates of the focal mechanism are in good agreement with those of the reference solutions.

#### 3.1.1 Application to 2016-2017 Central Italy sequence with P-wave peak amplitudes

We apply the methodology described in the Chapter 2 to a selection of 12 events that occurred during the 2016–2017 Central Italy sequence, which lasted from August 2016 to January 2017. This region is characterized by an extensional regime and normal faults events are expected. We used this piece of knowledge in an a priori constrain on the slip ( $\lambda \leq 0$ , see Appendix, Figure A1). In the absence of this a priori condition, there will be an equivalent fault planes solution with a positive slip. This indeterminacy can be solved reading at least one polarity of the P wave. The selected events have moment magnitude ranging from 4.7 to 6.5. We used three-component accelerometric stations distributed over azimuth and distance, within a maximum hypocentral distance of about 50 km. For all the analyzed

events, we simulate the real-time streaming of data, accounting for the P-wave propagation arrival time as a function of hypocentral distance. To avoid the inclusion of the S waves in the selected P-wave time window, we used variable time windows, depending on the source-to-receiver distance. Specifically, for stations within 25 km, we used a maximum time window of 1 s; 2 s are used from 25 to 30 km, and a P-wave time window of 3 s is used for larger distances. The inversions are performed every 1 s and start as soon as the predetermined condition on the azimuthal coverage is satisfied. This condition is to have at least 5 stations to start in the estimation or at least 4 bins populated on 6 bins (width of 60°), each filled by at least one station.

For the Mw 6.5 Norcia earthquake, we use a total of 54 three-component accelerometric stations (Fig 3.1 a). The first solution is available about 4.7 s after the earthquake origin time (O.T.), when data from six stations within 20 km of hypocentral distance are available, and the covering condition on the azimuthal distribution is satisfied. The evolution in time of model parameters is shown in Fig 3.1 (b, c, d, e) convergence of the solution is reached after four iterations, that is, 5 s after the arrival of first P wave, which corresponds to 7.7 s after the O.T. of the event (data latencies and computational times are not considered).

At this time, the RMS of amplitude error ( $\sqrt{\frac{\sum_{i=1}^{N^A} (d_{wi}^A - G(\mathbf{m}_{MAP})_{wi}^A)^2}{N^A - N^m}}$ ) of the solution reaches a stable value of 0.26. The final best solution (strike,  $151^\circ \pm 4^\circ$ ; dip,  $56^\circ \pm 3^\circ$ ; slip,  $-95^\circ \pm 6^\circ$ ) includes the amplitude data from 30 stations within 35 km of hypocentral distance. The inferred solution presents small errors both on strike, dip, and slip angles, and is consistent with the focal mechanism solution provided by the reference agency (INGV), with a KA of  $11^\circ$ . For simplicity we are not propagating the errors present in the data (i.e. we are not considering the uncertainties of location).

We note that slip and dip get slightly worse after the convergence is declared (Fig. 3.1). This could be due to the fact that, with the passing of time, data from farther stations (with a smaller signal-to-noise ratio [SNR]) are included in the inversion procedure, or to the inclusion of later, indirect and or converted phase arrivals, that might contaminate the focal mechanism estimation. One possible solution could be to stop the inclusion of stations as soon as a good azimuthal coverage is satisfied, for instance when we reach an azimuthal gap minor or equal to a selected threshold.

Results for the entire dataset are summarized in the table of Figure 3.2. For all the analyzed events, the final solution is declared within 5.5 and 12.7 s from O.T. and is consistent with the catalog focal mechanism solution, with a KA varying

between  $7^\circ$  and  $29^\circ$  (average KA equal to  $17^\circ$ ). The rms varies between 0.12 and 0.35, with an average value of 0.26.

For a selected real earthquake scenario, we also tested the sensitivity of the algorithm to the earthquake location and to the prior distribution by moving the source position (both on the horizontal plane and in depth) and using a completely uninformative prior distribution. In both cases, we found that the algorithm converges to realistic solutions, with KAs of  $11^\circ$  and  $17^\circ$ , respectively (Tarantino et al., 2019).

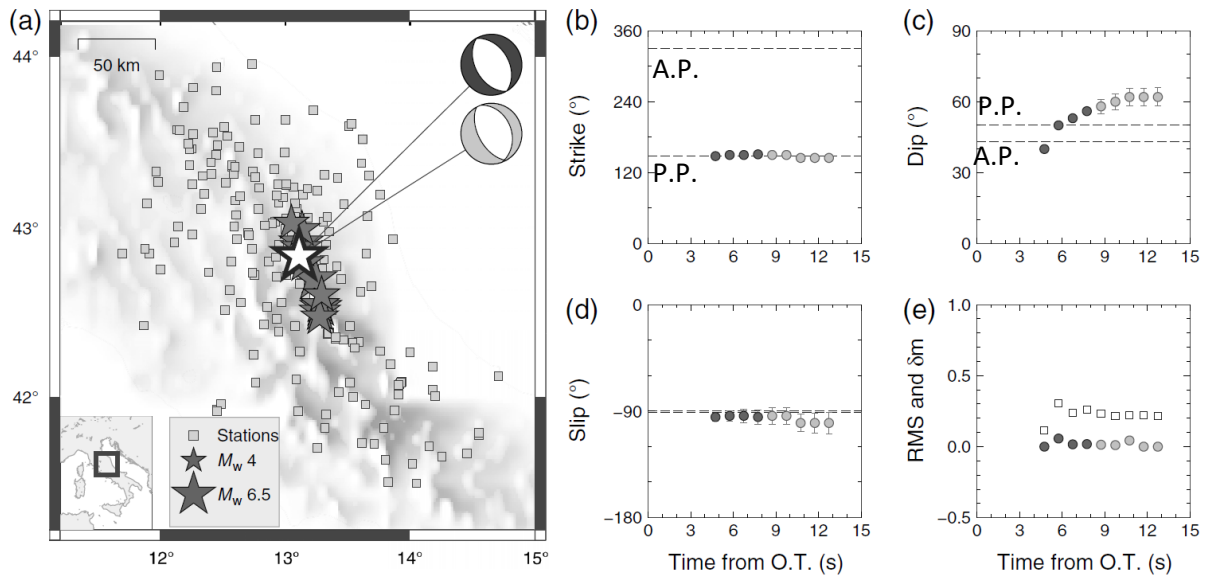


Figure 3.1: Results for the Mw 6.5 Norcia earthquake. (a) The epicentral location of selected earthquakes of sequence (dark gray stars) and the recording stations (light gray squares). The size of the stars is proportional to the magnitude, and the main event is represented with a white star. The black focal mechanism plot represents the Istituto Nazionale di Geofisica e Vulcanologia (INGV) catalog solution, and the gray one shows our best solution. (b–e) The solutions of strike, dip, and slip at each iteration, starting from origin time (O.T.). *P.P.* stays for principal plane, *A.P.* for auxiliary plane. Dashed lines represent INGV catalog solutions. Dark dots represent the solutions up to the convergence, and gray dots represent the solution evolution after the convergence. Error bars show the 68% confidence ellipsoid projection on each solution. (e) The root mean square (rms) of each solution (empty squares) and the convergence condition (with black and gray dots). Inset at the bottom left shows a map of Italy with an empty square indicating the region in exam, represented in the bigger artwork.

Region, magnitude, date, time	INGV reference solution	MAP model	rms	Kagan angle (°)	Time (s)	Number of data	RT best solution	INGV reference solution
Accumoli, $M_w$ 6.0 2016-08-24 01:36	155/49/-87 331/41/-93	147/49/-108	0.24	17	9.37	31		
Norcia, $M_w$ 5.3 2016-08-24 02:33	135/47/-98 327/43/-81	146/48/-104	0.28	16	8.49	20		
Amatrice, $M_w$ 4.8 2016-08-26 04:28	128/53/-106 333/40/-70	141/49/-80	0.35	21	8.44	11		
C.S. Angelo, $M_w$ 5.4 2016-10-26 17:10	161/38/-90 341/52/-90	157/56/-93	0.25	18	5.55	14		
Ussita, $M_w$ 5.9 2016-10-26 19:18	159/47/-93 344/43/-87	162/40/-105	0.21	16	9.56	46		
Norcia, $M_w$ 6.5 2016-10-30 06:40	151/47/-89 330/43/-91	151/56/-95	0.26	11	7.74	30		
Acquacanina, $M_w$ 4.8 2016-11-01 07:56	161/46/-82 330/45/-98	141/44/-96	0.33	14	9.34	20		
Acquacanina, $M_w$ 4.7 2016-11-03 00:35	162/24/-76 327/67/-96	158/38/-83	0.29	15	6.31	16		
Amatrice, $M_w$ 5.1 2017-01-18 9:25	153/32/-88 331/58/-91	162/49/-72	0.23	20	7.16	21		
Amatrice, $M_w$ 5.5 2017-01-18 10:14	161/51/-86 335/39/-95	160/48/-80	0.28	7	7.38	23		
Amatrice, $M_w$ 5.4 2017-01-18 10:25	140/35/-89 319/55/-91	139/58/-83	0.12	24	9.22	33		
Montereale, $M_w$ 5.0 2017-01-18 13:33	188/30/-39 313/71/-115	181/53/-62	0.27	29	12.70	35		

Figure 3.2: Summary of results for the whole sequence. The table reports a synthetic description of the results for all the analyzed earthquakes. From left to right, the columns contain region, magnitude, date, and time of each event; INGV reference solution (strike/dip/slip); maximum a posteriori probability (MAP) model in a Bayesian approach (strike/dip/slip); rms of final solution; Kagan's angle; time of convergence from origin time; number of data; focal mechanism plot representation of the best solution (RT) and of the INGV reference solution.

### 3.1.2 Application to Mw 6.5 Norcia earthquake with jointly use of P-wave peak amplitudes and P-wave polarities

We solve the inverse problem in Real Time for the mainshock of the Central Italy sequence using 2 independent datasets: P-wave peak amplitudes and P-wave polarities. As in the previous section, we simulated the streaming of data and considered increasing time windows of the S-P signal. In fact, in a simulated real time perspective, we only used the portion of the signal relating to the P wave, before the arrival of the S waves.

In this case, thanks the inclusion of information carried out by polarities, we can also infer the sign of the slip and solve the implicit ambiguity determined by the exclusive use of the absolute amplitudes. So that, the slip is explored between  $-180$  to  $180^\circ$ , while the strike is explored from  $0$  to  $360^\circ$  and the range for dip is from  $0$  to  $90^\circ$ . We used the same prior probability distribution as in the previous work, that means a combination of a Gaussian function with a cosine taper function at the edge of the space to smooth the transition toward zero. Our purpose is to help the exploration of the model space without excluding any other possible solution.

Thanks to the use of multiple datasets, we ignored the condition on the bin population for azimuth angle, indeed we are more confident about solution also with fewer stations.

In the case of Norcia earthquake, the first iteration is performed at 2.74 s after origin time with 3 stations and 2 polarities and it converges in 3 iterations at 5.74 s with just 15 stations, specifically with 15 mean amplitudes and 7 polarities. After that, the solution is not changing too much, consistently with our declared solution and as shown by the parameter  $\delta\bar{m}$  (Fig. 3.3). In particular, the strike is equal to  $156 \pm 17$  ( $^\circ$ ), dip equal  $33 \pm 6$  ( $^\circ$ ) and the slip equal to  $-95 \pm 10$  ( $^\circ$ ). The auxiliary plane is equal to  $342^\circ$  for strike,  $57$  for dip and  $-87$  for slip. Of course, also uncertainties associated to the solution tend to decrease in the time, since the solution is going to be more constrained as new data are acquired.

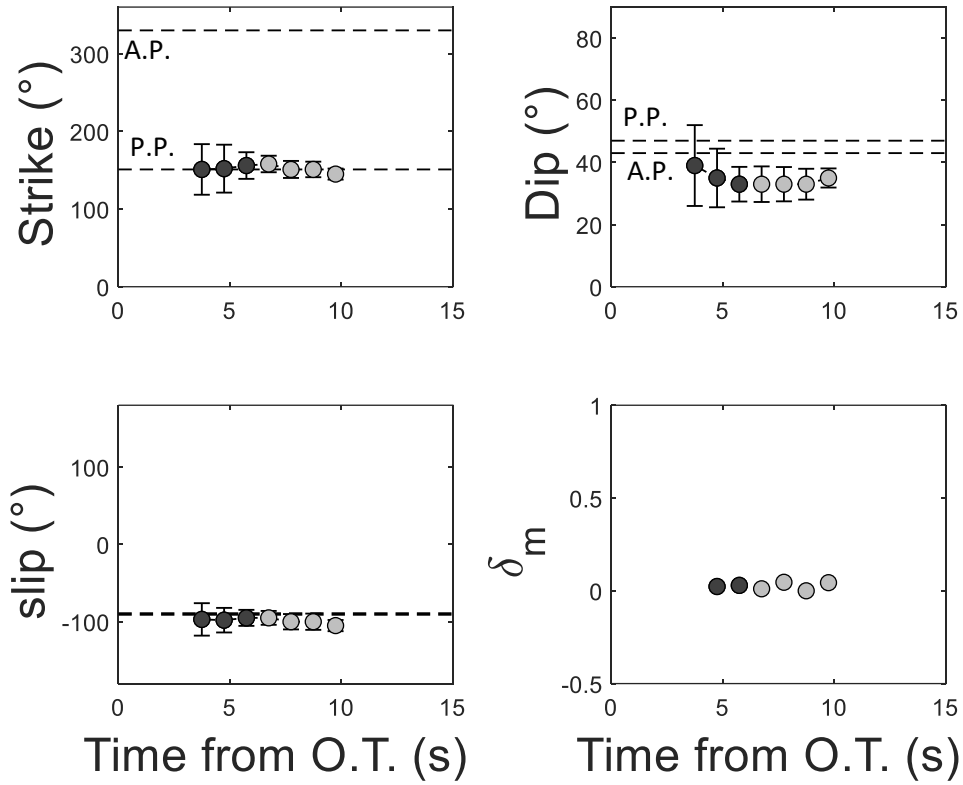


Figure 3.3: The solutions of strike, dip, and slip at each iteration, starting from origin time (O.T.). Dashed lines represent INGV catalog solutions. *P.P.* stays for principal plane, *A.P.* for auxiliary plane. Dashed lines represent INGV catalog solutions. Dark dots represent the solutions up to the convergence, and gray dots represent the solution evolution after the convergence. Error bars show the 68% confidence ellipsoid projection on each solution. Top left it is represented the strike of solution in time, top right the dip and bottom left the slip. Bottom right it is represented the convergence condition (with black and gray dots).

In this case we find a solution 2 seconds sooner than using only amplitudes datasets and with fewer stations. The fault mechanism we found has a Kagan's angle equal to  $17^\circ$  respect the INGV solution.

## 3.2 OFFLINE APPROACH APPLIED TO MICRO SEISMICITY FOR FOCAL MECHANISM ESTIMATION

The study of micro-seismicity ( $M_l \leq 3$ ) in areas characterized by the presence of active fault systems could reveal essential and larger-scale characteristics. Indeed, a challenging topic that is still open and arousing interest over the years is whether and if low magnitude earthquakes could show the regional stress field (De Matteis, 2012). If the micro-earthquakes behavior is a spy of regional stress field and could indicate what could happen on a larger scale, any essential information we can capture from microfractures could become essential in the forecasting and thinking about what the scenario for the next moderate event could be.

The main limitations associated with the study of micro-seismicity derive from the ability to detect this kind of events and from the large localization errors determined by the geometry of the network, by the lower signal-to-noise ratio, which affects the number and accuracy of the reading of the arrival times, as well as by the accuracy of the velocity model.

However, the installation of seismic networks with high spatial density can allow better quality localization and reduce the magnitude of completeness of detected events.

In this section, we will analyze natural and induced seismicity.

In general, when we talk about induced seismicity, we refer to seismic events that are the product of human activity. There are many ways in which human activity can cause induced seismicity, i.e., geothermal operations, reservoir impoundment (water behind dams), wastewater injections, and oil and gas operations including hydraulic fracturing.

### 3.2.1 Nagano, Japan

With the aim of investigating whether it was possible to use the method of Tarantino et al., (2019) to infer the orientation of the fault planes in the case of micro-seismicity, we studied the Nagano region, Japan, which is a well monitored area, affected by micro-seismicity. A fully automatic platform has been designed to study micro-seismicity and induced seismicity. This platform was able to detect events, pick waveforms and locate. The target magnitude was extremely low (Figure 3.4).

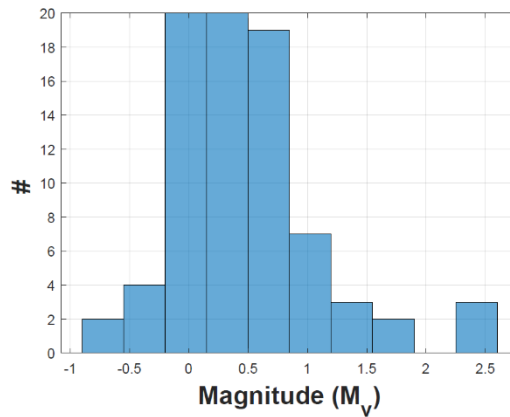


Figure 3.4: histogram of magnitude events for the analysed Nagano dataset.

Starting from the automatic picks provided by this platform, to determine the focal mechanism of the analyzed earthquakes, we divide the procedure into two steps. In the first part, we determine the strike, dip, and the absolute value of slip according to Tarantino et al, (2019), but in an offline framework and with an uninformative prior. Therefore, we performed an offline inversion considering all the stations for which we have automatic picks for P-wave. About the data processing, we first correct observed ground velocity and displacement P-wave peaks for the distance attenuation using empirical relationships between the P-wave peak amplitude and distance (see Appendix, Figure A2 for further details). Then, we normalize separately them respect their maximum. These values are finally combined in a simple average with equal weights and normalized again. The

data obtained in this way represent a measure of the absolute value of the radiation pattern observed at all available stations.

Secondly, we determine the sign of the slip considering all available automatic polarities performed by FilterPicker (Lomax et al., 2011) and minimising the associate error RMS for the 2 possible solutions (negative or positive slip). This couple of solutions are slip=  $\lambda$ , dip=  $\delta$ , strike=  $\phi$  (positive slip) and slip=  $\lambda - 180$ , dip=  $\delta$ , strike=  $\phi$  (negative slip).

We defined the 2 possible values of  $RMS_{\pm}$  on polarities, respectively for positive slip and negative slip, as:

$$RMS_{\pm} = \frac{1}{4(N_s - N_{unknown})} \sum_j^{N_s} [\Pi_j^{obs} * (\Pi_j^{obs} - |\Pi_j^{th\pm}|)]^2$$

where  $N_s$  is the number of available stations,  $N_{unknown}$  the number of stations without polarity data,  $\Pi_j^{obs}$  is the observed polarity at j-th station, while  $\Pi_j^{th\pm}$  is the theoretical polarity at j-th station for the predicted model with positive or negative slip inferred from first step.

We applied the methodology only to events with at least 6 picks for P-wave and excluding those events characterized by 0 km depth.

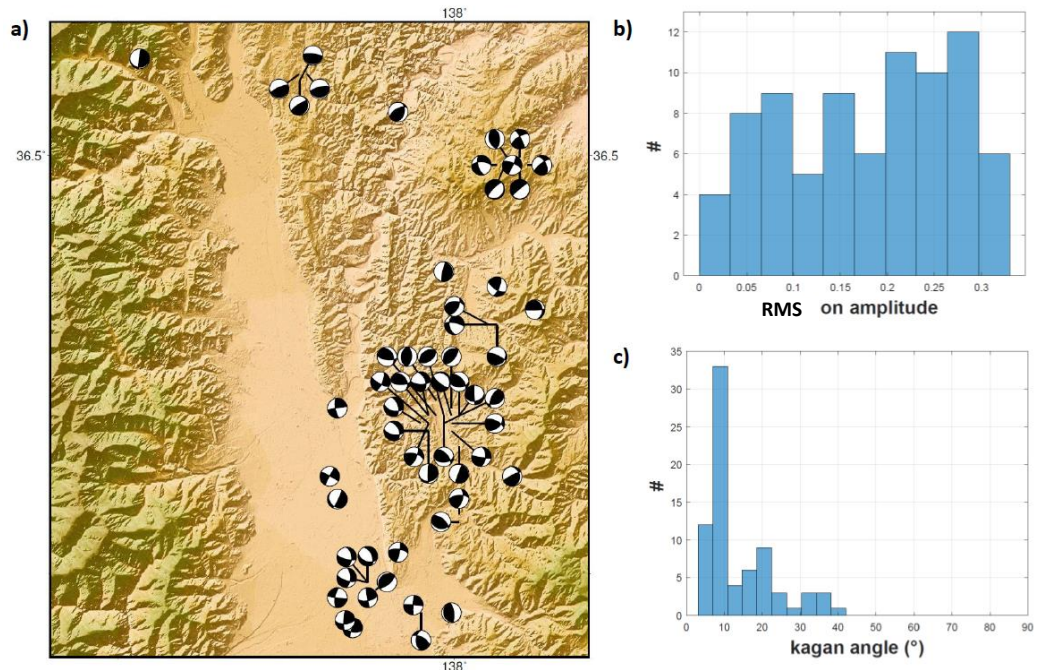


Figure 3.5: a) Map of the region with beach balls in black for solutions b) Histogram of RMS on amplitude for all solutions c) histogram of mean Kagan's angle of solutions in the posterior density function respect the MAP model of each event.

In Figure 3.5 a, we represent the beach balls for all solutions. The majority of events present a reverse mechanism, pure or with a strike-slip component. We also find some pure strike-slip events. Most events present very small values of the RMS on polarity, with a mean value of 0.21, while the mean value of the RMS on the amplitude is 0.18, that is a reasonable value. All solutions are available in the appendix (Table A1). In figure 3.5 b we show the RMS on amplitude. Moreover, we computed for each event the mean Kagan's angle of solutions until the 95% of probability in the posterior probability density function respect the MAP model and we plotted the histogram of mean Kagan's angles for all events. (Figure 3.5 c)

Figure 3.6 shows the event *2011.05.02.23.59.02* as an example. It is located at 3.6 km in depth, its magnitude is  $M_v 1.16$  and 22 stations are available (Figure 3.6a). The most likely solution has strike, dip and slip equal to  $278 \pm 1$  ( $^\circ$ ),  $72 \pm 2$  ( $^\circ$ ), and  $138 \pm 3$  ( $^\circ$ ), respectively, while the auxiliary plane is identified by  $(24^\circ, 50^\circ, 24^\circ)$ . The RMS on amplitude is equal to 0.29, while the RMS on polarity is equal to 0.06. In figure 3.6 a we represent the residual between the observed amplitude and the predicted one. We can see that residuals on the Radiation Pattern absolute value  $R_j^{obs} - R_j^{th}$  between observed and predicted by the MAP model, are all positive in the North of the hypocentre residuals, meaning an underestimation of predictions, while they are mostly negative in the South, meaning an

overestimation with respect to the observations. This can provide us some insights about the source directivity that likely occurred along the south-north direction and about the real fault plane. This because the directivity amplifies the observed amplitude in the directive direction, while decreases it in the opposite direction. In figure 3.6b we show the focal mechanism best solution, with the available automatic polarities reported. In figure 3.6c, on top left, we represent RMS on amplitude versus the Kagan's Angle (Zahradnik and Custodio, 2012; Michele et al., 2014) for all solution until the 95% of the maximum of the probability associated with the most likely solution. We observe a single solution since all of them present a Kagan's angle less than  $20^\circ$ . In the other panels we show, on the top-right the RMS on amplitude versus the difference in slip with respect to the slip of the most likely solution, on the bottom-right the misfit on amplitude for the difference between dip angles and the 'best' dip, and on the bottom-left the RMS on amplitude for the difference in strike. For all the tree parameters, we have a cluster of solutions concentrated around  $0^\circ$ , that means that they are all associated with the most likely plane, while there is another concentration of dots in correspondence of the values for the auxiliary plane.

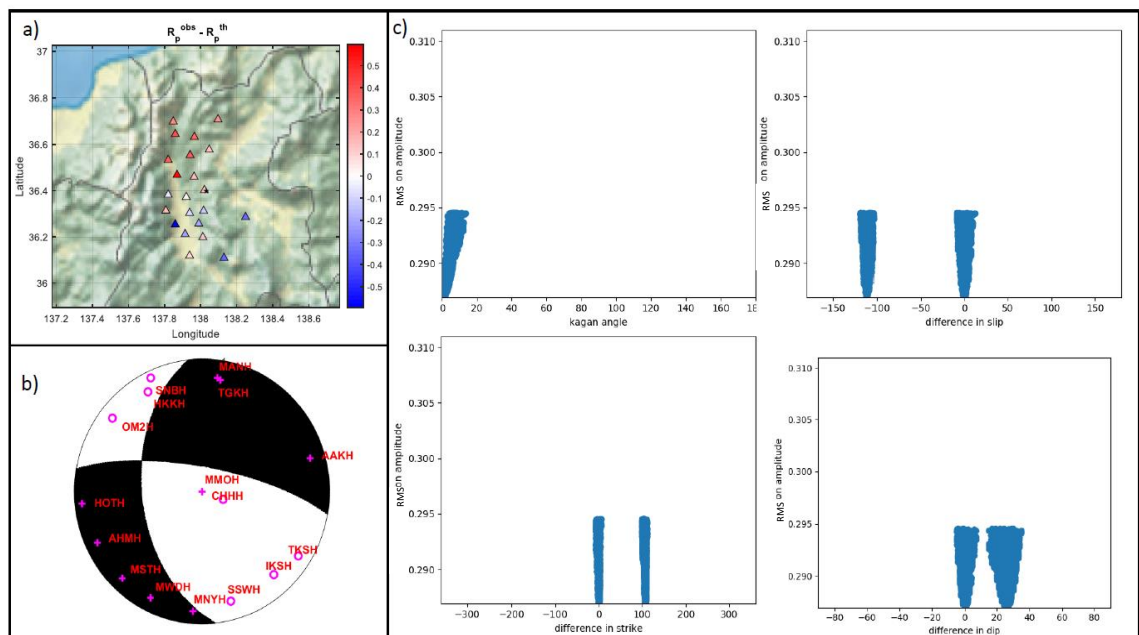


Figure 3.6: Example: a) Representation of the residual between observed and predicted amplitude at the available stations; b) Beach ball for the most likely solution. Black areas are for positive polarities and white regions for negative ones. The empty circles correspond to automatic negative polarities; crosses are for automatic positive polarities. Station names are reported in red. c) On the top-left it is represented the RMS on amplitude versus the Kagan's angle, on the top-right it is represented the RMS on amplitude versus the difference in slip with respect to the slip of the most likely solution, on the bottom-right the RMS on amplitude for the difference between dip angles and the 'best' dip, and on the bottom-left the RMS on amplitude for the difference between strike and the 'best' strike.

## 3.2.2 Rocca San Felice

The study region is Rocca San Felice, in the southern Apennines in Italy, that is monitored, together with the entire Irpinia region, by a high-density permanent network, Irpinia Seismic NETwork (ISNet), with a mean minimum interstation distance of 15 km and a completeness magnitude detection of 1.5 MI. This network is equipped with co-located tri-axial strong motion accelerometers and three-components short period or broad-band seismometers, allowing for high dynamic range (Weber, 2007). An Ms 6.9 event, the Campania-Lucania earthquake, occurred in 1980 south-east than Rocca San Felice. It involved 3 fault segments, activated at 0, 18 and 39 s after the first shock, and it was a pure normal-faulting event (Bernard and Zollo, 1989). The faults system was approximately 60 km long and northwest-southeast striking oriented.

It has been observed that along Campania-Lucania region there are zones of weakness producing repeated earthquakes and swarm-like microearthquake sequences characterized by co-located events that share the same focal mechanism, which has been observed in the area (Stabile et al., 2012).

Along the Apennines we observe northwest-southeast striking normal faults with a T-axis orientation of approximately  $70^\circ$  in azimuth and a roughly east-west oriented strike-slip fault transversely cutting the belt (Pantosti and Valensise, 1990; Frepoli and Amato, 2000; Montone et al., 2004; DISS Working Group, 2010; Pasquale et al., 2009; Festa et al., 2021).

On the 3<sup>rd</sup> of July 2020, it occurred a sequence in Rocca San Felice with two MI 3.0 mainshocks and lasted 7 days. 21 of these events ( $>1.5$  MI) presented an orientation consistent with the ones of the first fault segment fractured during the 1980 earthquake (Festa et al, 2021).

We applied and tested our updated methodology focusing on the Rocca San Felice sequence and infer the T-axes orientation in this area. In fact, we know from the literature that the microearthquakes in the entire Irpinia area are not randomly oriented but occur on subparallel fracture planes highly organized inside the volume delimited by the faults of the 1980 earthquake (De Matteis, 2012, Stabile, 2022). Our main purpose here is to push beyond in the minimum limit on magnitude range for this kind of study (MI 0.4-3.0).

Firstly, we applied to the full sequence of 64 events that occurred in Rocca San Felice using manual picking of P and S-wave arrival times in order to show potential benefits of this method to study micro-seismicity; in fact, it is a useful tool to study T-axis orientation and investigate the behaviour of micro-events respect to the regional stress field.

Then we applied the technique to 39 events of those previously studied and which were automatically detected by PRESTO (Satriano, 2010, <http://www.prestoews.org/>), a free and open-source software platform for Earthquake Early Warning. We used only available data from automatic picking performed by PRESTO. We compared these new results with those obtained with the manual picking and we found corresponding focal mechanisms. Our results show that this procedure could easily integrate this kind of platform to produce post events results in a fast and automatic way also for low magnitude events ( $M_l < 3$ ). Of course, the possibility to have multiple solutions is still present as in classical methods applied to microseismicity.

### 3.2.2.1 Rocca San Felice with manual picking

We applied this methodology to 64 events with magnitude ranging between 0.4 – 3.0  $M_l$  that occurred in Rocca San Felice, Irpinia, from 3<sup>rd</sup> of July to 10<sup>th</sup> of July. They occurred mostly in the northern border of the network (Figure 3.7 a). Because of the quality of the data, we used broadband stations records in the case of co-located tri-axial strong motion accelerometers and three-components broad-band seismometers were both available. Otherwise, we integrated the data on tri-axial strong motion accelerometers to retrieve the velocity records. We

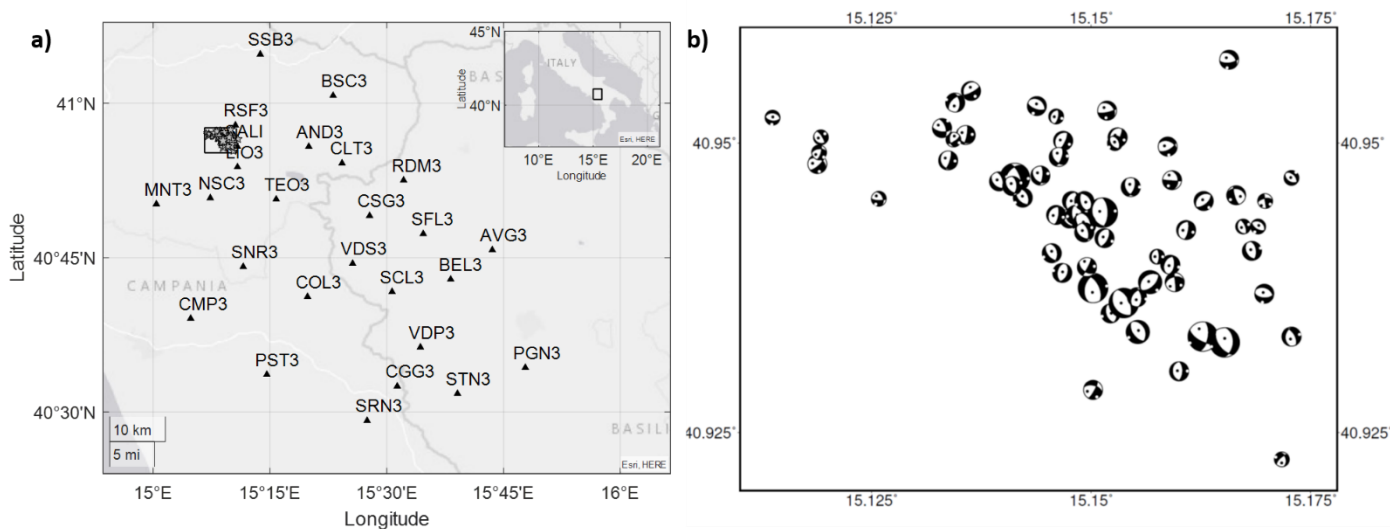


Figure 3.7: Events with manual picking: a) map of all events, black triangles represent stations while grey stars the events and empty box represent with black line represent region in section b); the insert on the right top is map of Italy, with a black empty box representing the study area b) beach ball results for event in study, in each ball white dot represent T-axes while black dots represent P-axes.

used polarities, P-wave amplitudes and S-wave/P-wave amplitudes ratio recorded

at 3-components velocimeters and accelerometric stations of ISNet network. In this case, the picking is manually performed. We used precomputed empirical relationship, specific for the region, to correct P-wave amplitudes for distance (Bobbio, 2009) and we obtained S/P-wave amplitudes ratio using the velocity model (Matrullo et al.,2013). We remind that the only difference between S and P wave amplitudes is in the phase velocity while the other factors cancel each other out. (See the methodology in Chapter 2) The beachballs are plotted in Figure 3.7 b and the results in strike, dip and slip angles are listed with their uncertainties in the Appendix (Table A2).

The events which show a pure normal focal mechanism (T-axes essentially horizontally oriented with a plunge  $\leq 30^\circ$  and P-axes plunge  $\geq 60^\circ$ ) represent the 69% of events, while the 28% it is a normal fault with a strike slip component (T-axes essentially horizontal with a plunge  $\leq 30^\circ$  and P-axes plunge ranging in the range  $30-60^\circ$ ) and 2% is pure strike slip. The strike orientation has a mean value of  $349^\circ$  and a mode of  $351^\circ$  (Figure 3.8 b). The mean dip is  $54^\circ$  and the mean slip angle is  $-83^\circ$ . The T-axes show an azimuth mostly oriented between  $70^\circ$  and  $90^\circ$ , with a mean value of  $83^\circ$ . This observation is in agreement with that we expect along Apennines and it was observed for this sequence (Festa et al,2021). We also computed the mean Kagan's angle between our MAP model and solutions for the common events in Festa et al, 2021, obtaining a median value of  $20^\circ$  and a mode of  $6^\circ$ , so that they are very consistent.

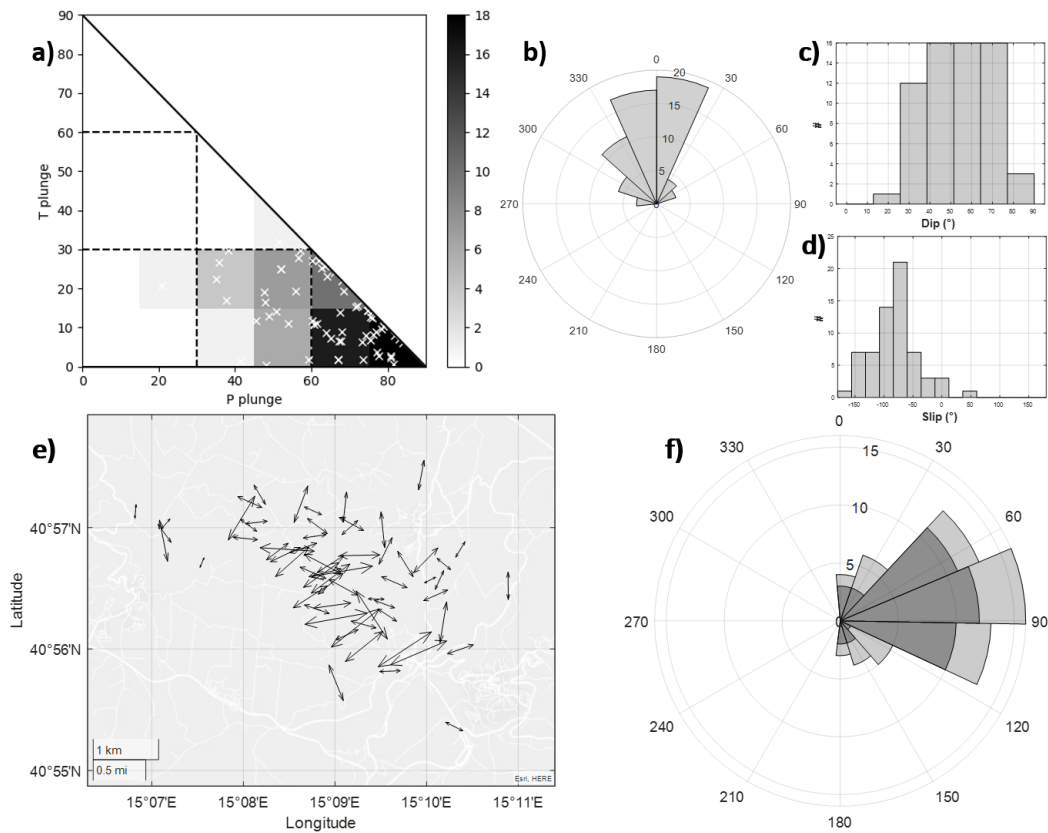


Figure 3.8: Summary results for revised events with manual picking: a) T-plunge vs P plunge. Grey tones represent bin population (each bin has size  $30^\circ \times 30^\circ$ ).; b) polar histogram for strike orientation; c) histogram for dip; d) histogram for slip; e) Double arrows represent the orientation of T-axis, the map section is the box delimited in Figure 1 a; e) Polar histogram of T-axis orientation: light grey for all events, only the percentage in dark grey is a pure normal fault.

The result for 2020-07-03 16:19:23 event with a local magnitude of 3.0 ML is shown in Fig. 3.9. The number of available stations is 14, with 14 amplitudes, 12 polarities and 10 S-wave/P-wave amplitudes. The results are a strike angle of  $360^\circ \pm 8^\circ$ , a dip of  $61^\circ \pm 1^\circ$  and a slip angle of  $-80^\circ \pm 9^\circ$ . It is a normal focal mechanism with a strike slip component. The posterior probability distribution has a single solution well constrained (Figure 3.9 b). The auxiliary plane associated to this solution is (160,31,-107).

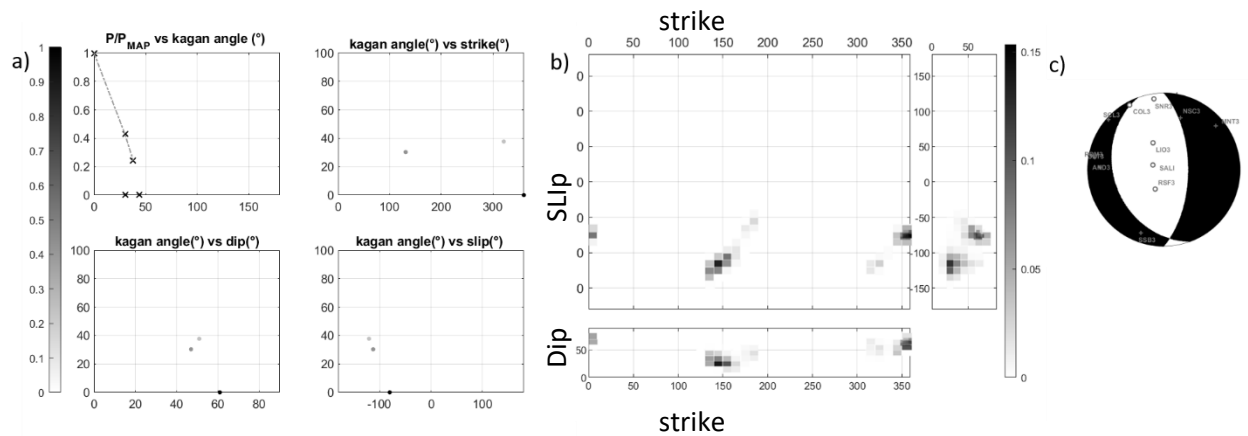


Figure 3.9: results for 2020-07-03 16:19:23 MI 3.0 event with manual picks: a) Kagan's angles respect MAP model, the color is related to the Probability normalized on the MAP model: on the top left the Probability normalized on the MAP model probability for different solutions belonging to the posterior PDF, the dashed line represents the outer envelope of the Kagan's angle distribution with respect to the map model; on the top right we represent the Kagan's angle of solutions respect the MAP model in function of strike, on the bottom left the Kagan's angle of solutions respect the MAP model in function of dip and on the bottom right the Kagan's angle of solutions respect the MAP model in function of the slip; b) sections of marginal Posterior probability density function with a grayscale coded from white to black (0 to maximum of marginal posterior probability). In the top it is the section strike-slip, on the right the section dip-slip, on the bottom the section strike-dip; c) beach ball of the MAP model, empty circle represents a down polarity, cross represents an up polarity.

The result for 2020-07-03 19:46:21 event with a local magnitude of 0.6 MI are shown in Figure 3.10. The number of available station is 5, with 5 amplitudes P, 2 polarities and 4 S-wave/P-wave ratio amplitudes. The results are a strike angle of  $337^\circ \pm 26^\circ$ , a dip of  $67^\circ \pm 11^\circ$  and a slip angle of  $-93^\circ \pm 47^\circ$  (Figure 3.10 b). It is a normal focal mechanism with a strike slip component. The auxiliary plane associated to this solution is (165,23,-83).

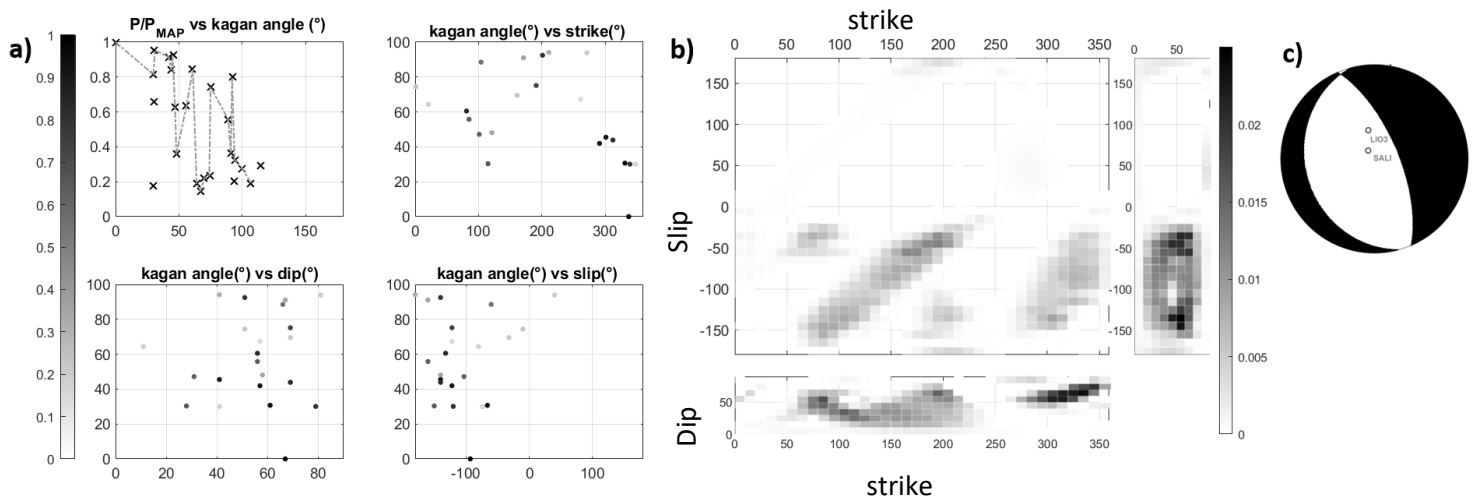


Figure 3.10: as in Figure 3.9 but representing results for 2020-07-03 19:46:21 MI 0.6 event with manual picks

### 3.2.2.2 Rocca San felice with automatic picking by PRESTO

We applied this methodology to 39 events with magnitude ranging between 0.9 – 3.0 MI occurred in Rocca San Felice, Irpinia, from 3<sup>rd</sup> of July to 10<sup>th</sup> of July, detected and located by PRESTO, the system monitoring the area (Figure 3.11 a). The system uses FilterPicker to pick automatically waveforms and where it is possible it assigns a polarity. It is designed to operate stably on continuous, real-time, broad-band signals (Lomax et al., 2012). Each pick has a weight that reflects the quality and uncertainty of the reading; we included it to associate a  $\gamma_j$  (see formula 2.1) to the automatic polarity. We used precomputed empirical relationship to correct P-wave amplitudes for distance. The results in strike, dip and slip angles with their uncertainties for all events are available in the Appendix (Table A3), while the map with beach balls is available in figure 3.11b. To evaluate the automatic performance with respect the results obtained with manual picking, we computed for each event the Kagan’s angle (Kagan,1991) between MAP model from automatic picking with the MAP model solution obtained with manual picking. This

give us a quantitative estimation of how much 2 different fault-plane solutions are different.

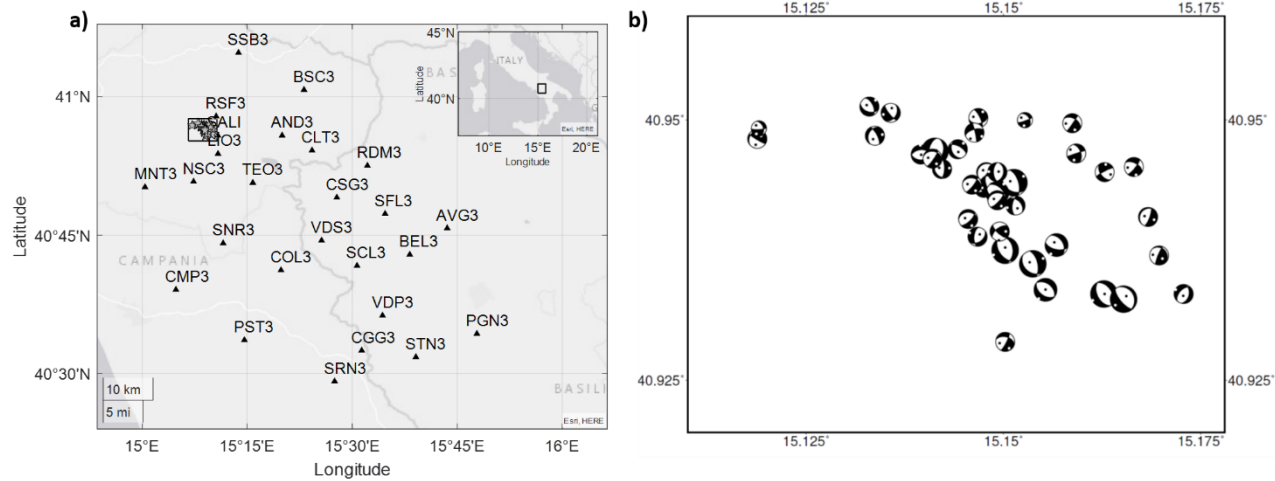


Figure 3.11: Events with automatic picks: a) black triangles represent station, grey stars the epicentral locations of events, the empty box with black border represent the area in figure b), the insert on the right top is map of Italy, with a black empty box representing the study area; b) beach ball for events automatically detected, white dot represent T-axes while black dot the P-axes.

Moreover, if 2 couples of solutions have to each other a Kagan's angle less than  $30^\circ$ , they are accepted as very similar, on the other hand in the case of an angle less than  $60^\circ$ , they are still describing a corresponding focal mechanism (Pondrelli et al., 2006; D'Amico et al., 2011). In this case, considering a comparison one to one respect the 2 MAP models, we obtained a median Kagan's angle equal to  $51^\circ$  with a mode of  $11^\circ$ . In the case we only consider events with at least 4 polarities in agreement between manual and automatic P-wave arrival time picking, the median value is  $37^\circ$  and the mode  $11^\circ$ . This also includes cases with a mismatching of manual and automatic polarities till the 29%. The median value is  $30^\circ$  if we consider at least 6 correct polarities (Fig. 3.12 a). However, if we consider also other multiple solutions until the 75% probability level respect MAP model in the case of the automatic picking, the median Kagan's angle with MAP model obtained with manual picking is  $27^\circ$  with a mode of  $8^\circ$  (see figure 3.12 c). We do this to take into account multiple solutions, that are available also in classic methods as in Festa et al., 2021. For example, for the event 20200703 09:30 59.98 MI 3.0, there are 2 possible solutions. The first one with stdr equal to 0.58 (69/61/168; 165/80/30) and the second one with stdr = 0.87 (95/45/-120; 314/52/-63). The stdr gives us information on how much a solution is well constrained, so the best solution in terms of stdr is the first one, however for the geological context and for the nature of the focal mechanism of the seismic sequence it was selected the second one by Festa et al, 2021. Moreover, the KA between these 2 possible

solutions is  $61^\circ$ . It is common for microseismicity to have multiple solutions and not one well constrained. In case of more solutions, one strategy could be select the focal mechanism most similar within a seismic sequence.

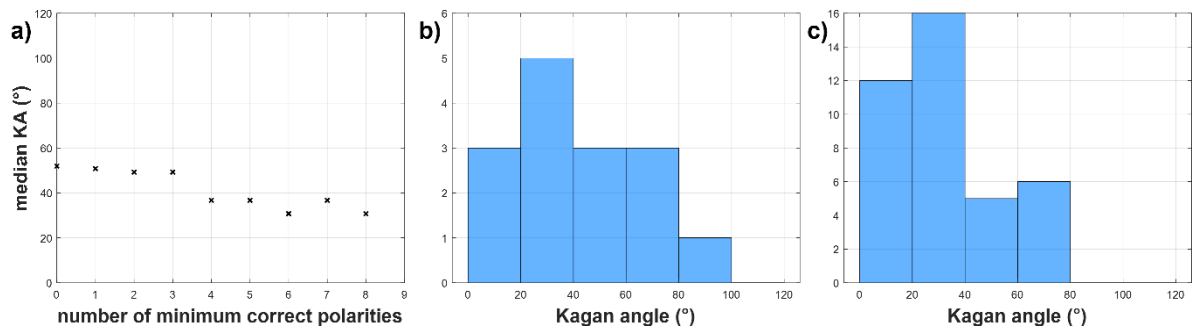


Figure 3.12: Summary of Kagan's angles between solutions obtained with manual picking and those obtained with automatic picking; a) Median Kagan's angle between MAP model obtained with automatic picking respect MAP model in function of minimum number of correct polarities ;b)Kagan's angle between MAP model obtained with automatic picking respect MAP model obtained with manual picking for events with at least 4 correct polarities; c) minimum Kagan's angle between MAP model obtained with manual picking respect all solutions until 75% probability respect the MAP model obtained with automatic picking.

In the Figure 3.13 a) we plotted the T-axis plunge vs P-axis plunge inferred from focal mechanism solution. Most events still show a pure normal focal mechanism (51 %). 28 % of events are normal with a strike slip component, while 5% is pure strike slip. The strike orientation has a mean value of  $329^\circ$  and a median value of  $334^\circ$  (Figure 3.13 b). The mean value for dip is  $49^\circ$  (Figure 3.13 c) and for slip is  $-64^\circ$  (Figure 3.13 d). We plotted the T-axis orientation in the map (Figure 3.13 e). T-axes are mostly oriented North-East East. We also plotted a histogram for T-axis orientation with 2 grey tones, light grey for all events and dark grey for pure normal events (Figure 3.13 f).

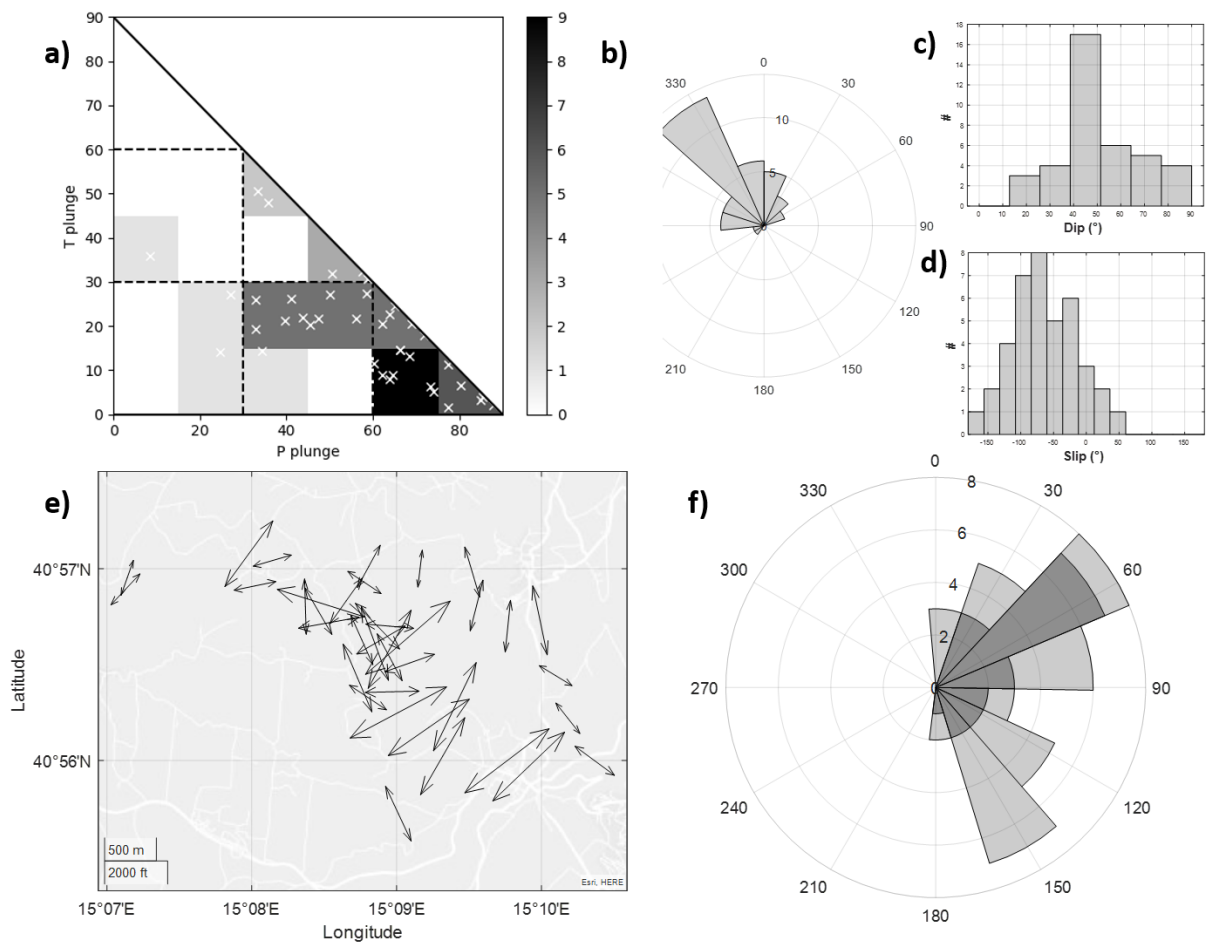


Figure 3.13: Summary results for automatic picks: a) ,b) , c) , d) as in Figure 3; e) Orientation of T-axis, black double arrows f) Polar histogram of T-axis orientation: light grey for all events, only the percentage in dark grey is a pure normal fault.

In the figure 3.14 we show an example, the results for 2020-07-03 16:19:23 event with a local magnitude of 3.0 MI. The number of available stations is 13 , with 13 amplitudes and 8 polarities. We grouped the solutions from posterior probability density function in families and we plot their posterior probability normalized on the MAP model probability value in fuction of Kagan's angle respect MAP model. The posterior probability distribution has a single maximum (Figure 3.14a). The results for MAP model are a strike angle of  $342^{\circ} \pm 19^{\circ}$  , a dip of  $62^{\circ} \pm 17^{\circ}$  and a slip angle of  $-69^{\circ} \pm 36^{\circ}$  (Figure 3.14 c). It is a normal focal mechanism with a strike slip component and its Kagan's angle with respect to the solution obtained with manual picking is  $22^{\circ}$  , so that they are very consistent. We plot the marginal

distribution sections, that show 2 patches corresponding to the solutions associated to the main and auxiliary planes of MAP model (Figure 3.14 b).

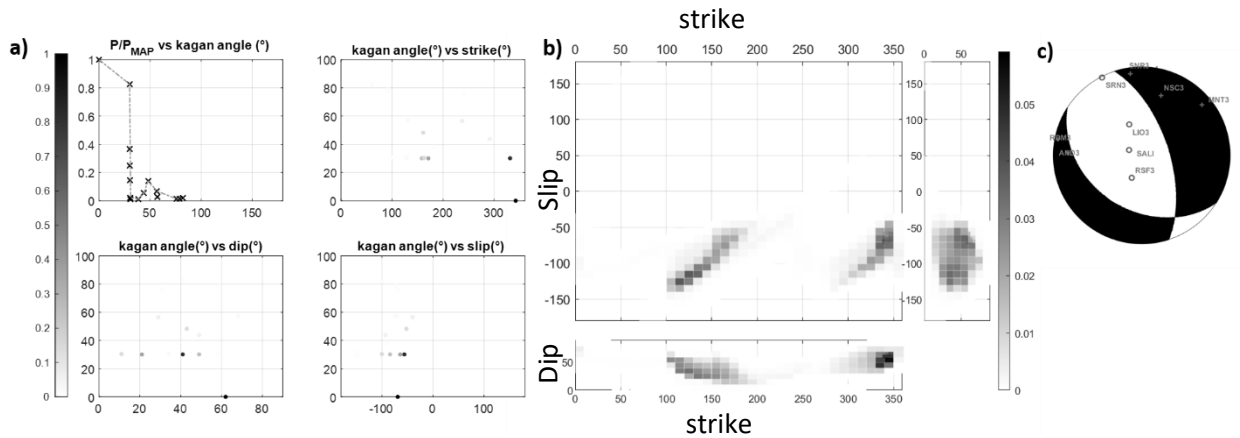


Figure 3.14: as in Figure 3.9 but representing results for 2020-07-03 16:19:23 MI 3.0 event with automatic picks.

The 2020-07-03 19:46:21 event was not triggered by PRESTO and automatic P-wave arrival time picks are not available. In the figure 3.15 (a,b,c) we represent the result for 2020-07-05 14:14:04 event with a local magnitude of 1.2 MI. We have a single maximum in the posterior probability distribution. The map model is strike equal to  $185^\circ \pm 18^\circ$ , dip equal to  $59^\circ \pm 24^\circ$ , slip equal to  $-121^\circ \pm 52^\circ$ , with an auxiliar plane equal to  $54^\circ, 43^\circ, -49^\circ$  respectively for strike, dip. It is a normal focal mechanism with a strike slip component and its Kagan's angle with respect to the solution obtained with manual picking is  $22^\circ$ .

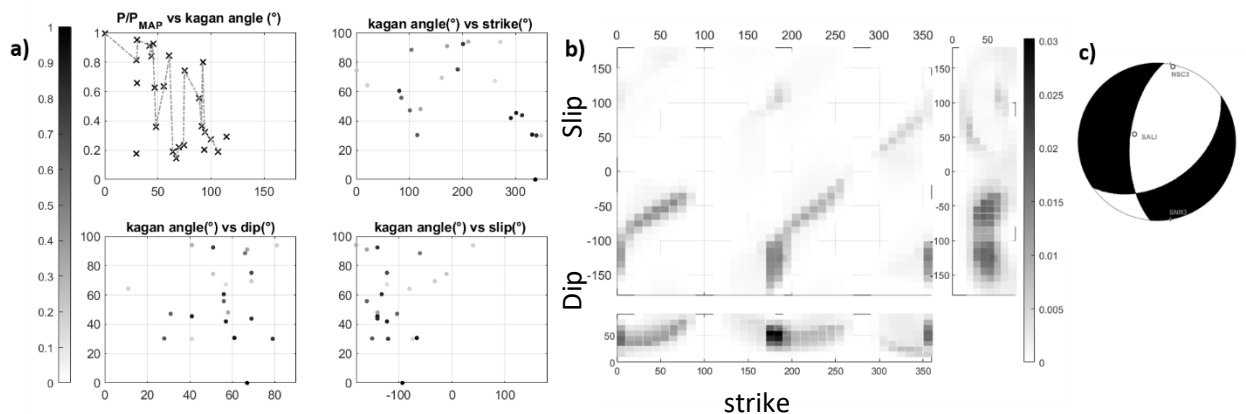


Figure 3.15: as in Figure 3.9 but representing results 2020-07-05 14:14:04 MI 1.2 event with automatic picks.

## 4 BACK PROJECTION APPLICATION

---

### 4.1 BACK PROJECTION ON SYNTHETIC TEST

Back-projection can be used as an effective method for imaging the major asperities of slip, especially at high-frequency, and allows modelling the areas in correspondence with the maximum slip (Maercklin et al., 2012) or can locate the seismic sub-events of an earthquake (Meng et al,2018; Xie & Meng, 2020).

We worked on a fast characterization of kinematic parameters. As soon as an occurred event is located, the Magnitude can be estimated (Nazeri et al, 2019) and a preliminary estimation of the focal mechanism is provided as we see in Chapter 3, we can back-project the recorded amplitudes to fast estimate kinematic parameters. We applied the beamforming and stacking approach to synthetic data simulating a Mw 6.5 in Central Italy, with a fault oriented as 2016, Mw 6.5 Norcia earthquake with a final slip map with a directivity North-Northwest.

The expected length along the strike direction, generally referred to length  $L$  is computed by using the magnitude/fault length Wells & Coopersmith (1994) scaling law.

Since most of the low frequency radiation comes from the main slip asperity, the estimates of source radius from the LPDT curve (Nazeri et al. 2019) can be interpreted as the size of this main patch of fault slip for events as large as the main event of the 2016-2017 central Italy sequence and hence they can be used to constrain the smaller dimension of a rectangular fault plane model, that is the width  $W$  (Wells & Coppersmith, 1994). In particular the width is imposed as the double of the estimated radius.

Finally, the focal mechanism was constrained by exploiting the results of the algorithm presented in Tarantino et al., 2019. In principle, without either any further tectonic constraints or a clear aftershock distribution pattern it is not possible to distinguish the real geometry of the fault plane from the auxiliary nodal plane both provided by the focal mechanism solution.

In this early phase of the seismic phase recording, the main ambiguity is expected to be the dominant propagation direction of the rupture from the hypocenter. Several techniques have been proposed to rapidly determine the rupture directivity, but most of them are based on the azimuthal variation of the peak ground kinematic parameter that are not yet available when only the first P-wave arrivals have been recorded at the closest station. Therefore, rectangular fault planes oriented according to the focal mechanism solution with dimensions  $2L \times W$  have been built. The doubled length of the fault plane allows to place in a random position the main patch of slip accounting for the initial epistemic uncertainty about the position of the main patch of the slip with respect to the hypocenter. The fault plane is centered on the hypocenter of the case-study with respect to the strike direction. The fault is placed such that the hypocenter depth is at the 0.75 times the along dip distance, this choice is justified by the fact that a deeper nucleation is more likely to occur than a shallower one (Causse et al. 2009, Scala et al. 2018). Once a geometry is defined a first update of the point source shake map would be released by using the same GMPE imposing a Joyner & Boore (1988) distance from projection onto the Earth surface of the fault plane. It is worth to note that as long as the ambiguity deriving from focal mechanism solution is not resolved we impose that for each point in the vicinity of the source the distance is imposed as the minimum one from one of the two projection.

### 4.1.1 Set up of model and forward simulation

The fault for the generation of synthetics was discretized in number of sub-sources such that the plane is subdivided in a  $\sim 150$  m spaced regular grid. Considering a rupture propagating at  $\sim 3$  km/s, this would allow to model the generated signal up to  $\sim 4$  Hz properly describing the smallest wavelength with at least 5-6 point.

The slip amplitude distribution  $A$  has been defined following a  $k^{-2}$  paradigm. Such kinds of slip distributions are defined summing a low-frequency deterministic source description and stochastically distributed shorter wavelength asperities with a slip amplitude decaying as  $k^{-2}$  in the wavenumber domain  $k$ . This technique is commonly used in the definition of forward modelling of the seismic source since it is expected to lead to more realistic synthetic seismograms enriching their high-frequency content (Herrero & Bernard, 1994). In this phase, on a rectangle having size  $(L, W; \text{with } L=26 \text{ km and } W=10 \text{ km})$ , the main low frequency patch of slip is defined as a simplified Gaussian distribution re-scaled to take into account

the estimated seismic moment (Figure 4.1 a). To account for the epistemic uncertainty on the non-well constrained source kinematic parameters, a set of 1500 different kinematic models has been generated (Scala et al 2018). Then, only one was used blindly as forward model

For a  $k^{-2}$  slip distribution, the roughness parameter  $K$ , is proportional to the corner wavenumber beyond which the slip amplitude is expected to decrease as  $k^{-2}$  in the wavenumber domain and hence represents a proxy of the slip amount that is subtracted by the shorter wavelength asperities from the low-frequency main asperity. For each of the 1500 slip distributions the parameter  $K$  is extracted from a log-normal distribution having  $\mu = 0.74$  and  $\sigma = 0.28$  (Figure 4.1 b). A constant rupture velocity for each distribution is extracted from a uniform distribution between the 65% and the 85% of the S-wave propagation velocity at the average depth of the fault plane (Figure 4.1 c). To place the slip distribution on the whole fault plane having dimensions  $(2L, W)$ , the center of the Gaussian slip is randomly extracted from a uniform distribution, tapered towards the edge (Figure 4.1 d). The final slip distribution is defined summing the low frequency distribution and short wavelength asperities whose centers are located at a distance  $d \leq L/2$  with respect to the center of the Gaussian. In Figure 4.2 e) an example of a final stochastic slip distribution is shown.

An inhomogeneous rise-time has been imposed on the sub-sources and each of the rise time value has been extracted from a Gaussian distribution having a mean in turn extracted from a uniform distribution in the interval  $[0.5s, 2.0s]$ , (Scala et al., 2018).

The velocity model used to generate synthetics is a one-dimensional model for the Central Italy (Carannante et al., 2013).

To generate the synthetics, we used a modul of LinSlipInv method (Galovič et al., 2015; <https://github.com/fgallovic/LinSlipInv>).

The synthetic seismograms were available at the location of 51 real stations that recorded the Norcia event. The epicenter of the event (red star) and the stations (green triangles) are plotted in Fig. 4.2 (b).

Examples of the three-component signals simulated at the stations T1220, and AMT are showed in Fig. 4.2 (c-d). They represent the synthetic velocity traces at a directive and an anti-directive station, respectively. In figures 4.2 (e-f) the amplitude displacement spectra for the same stations in the panels (c-d) are plotted for the vertical component. The corner frequency ranges from 0.15 to 0.35

Hz for the stations considered in the analysis. We will investigate the back-projection within two ranges, a range at lower frequencies [0.15-0.5 Hz], around the corner frequency of the amplitude spectrum and one at higher frequencies [0.5, 2 Hz], where it is expected the decrease of spectrum as  $k^{-2}$ .

## 4.1.2 BP application and results

The Back-Projection approach we implemented can be considered as an extension of the technique proposed by Maercklin et al. (2012) to a near-source application for a moderate earthquake and is described in the Chapter 1, while it was previously used to study a giant earthquake (2011, Tohoku) at epicentral distance of 100 to 400 km. We use the vertical component as in Maercklin et al. (2012) and compute the  $S_V$  radiation pattern for each sub-source/receiver couple. We also checked the stability of our results respect the threshold on the radiation pattern coefficients.

In an automatic pre-processing phase, the synthetic velocimeters are cosine-tapered to reduce the effect of windowing, and then high-pass filtered with cut-off frequency at 0.5 Hz to avoid amplification of noise at low-frequency during the integration. We integrate the recordings to obtain displacement. Then we cut a window for the S wave at the theoretical S wave arrival time considering a homogenous medium with the S velocity equal to 3.1 km/s. We execute a cosine-tapering to reduce the effects of the S wave windowing.

We passband filter synthetics to select the frequency range of the investigation. As visible in the spectrum of the displacement (Figures 4.2 (e-f)),  $f_c$  is around 0.3 Hz, so the frequency ranges investigated are 0.15 – 0.5 Hz and 0.5 – 2 Hz, in order to explore contributions to the slip imaging around the corner frequency and at higher frequencies, respectively. In this latter frequency band, the slip amplitude is expected to decrease as  $k^{-2}$  (Bernard et al.,1996; Gallovič and Brokešová (2004) in the wavenumber domain.

A crucial element for back-projection is the choice of time window  $t_w$  to be applied for the stacking. A parametric investigation showed that the optimal choice of  $t_w$  correspond to the reciprocal of the central frequency of the corresponding band that is, in our case, 3 s for the low-frequency band and 0.7 s for high-frequency band. To smooth the slip rate and slip time evolution we imposed a time window overlap of 0.5  $t_w$ .

In order to include some noise in the test and because the technique is designed to work with an homogeneous medium, the signals were back-projected considering a constant velocity phase for S-wave (mean value of the 1d velocity model of Carrante et al, 2013) on a fault plane centred on the hypocentre (Latitude=42.832°, Longitude=13.111° Depth=9.52 km) and having the prescribed focal mechanism (strike=151°, dip =56°, slip=-95°) and a rectangular shape with dimensions  $\sim 2L \times 2W$  to take into account the variability of the hypocenter position respect the main patch. L and W are estimated from the empirical relationship (Well and Coppersmith,1994) once the Magnitude is estimated. Through a grid refinement analysis, we verified the consistency of the slip imaging for cell sizes ranging from  $1 \times 1$  km<sup>2</sup> to  $4 \times 4$  km<sup>2</sup>. The presented results refer to the  $1 \times 1$  km discretization. Of course, in a fast estimation (maximum few minutes after O.T.), the same analysis should be computed as well on the auxiliary plan because we cannot discriminate in principle between the 2 planes provided by the focal mechanism.

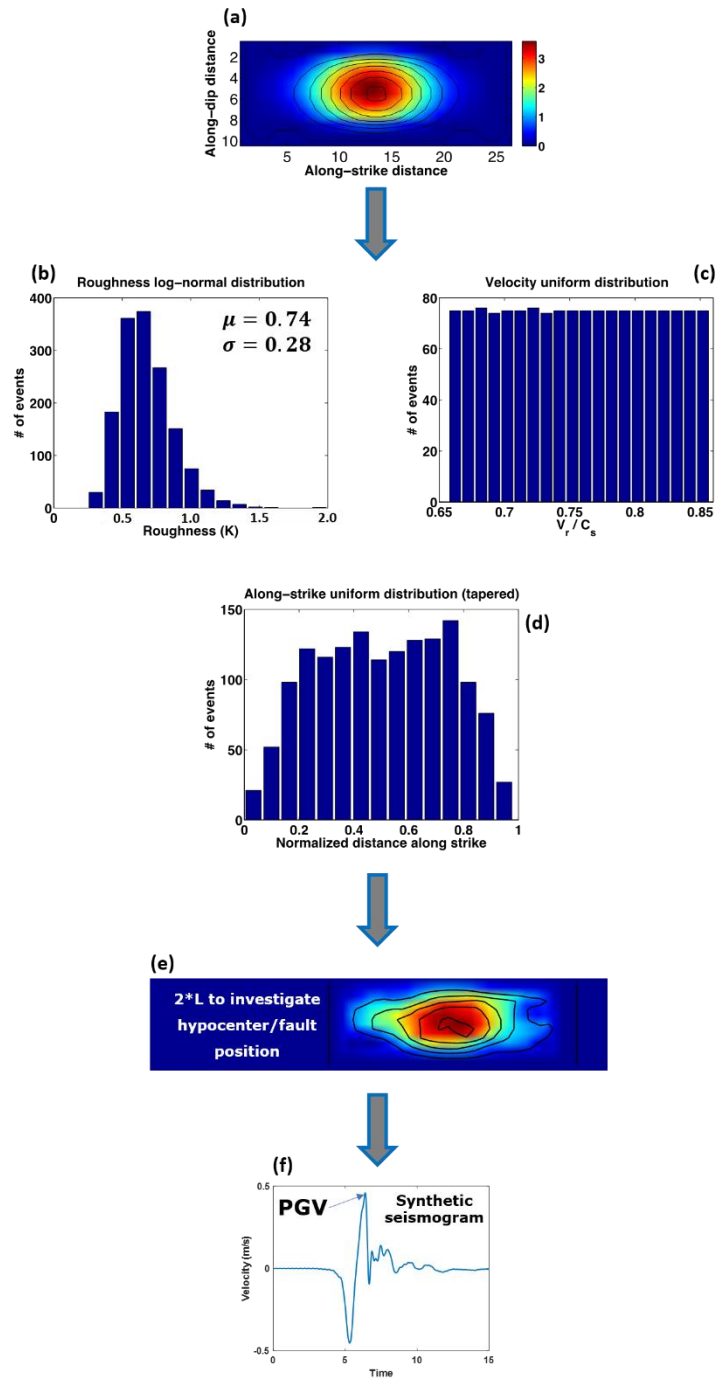


Figure 4.1 (a) Simplified low frequency Gaussian slip distribution centered in the middle of the fault. (b-c-d) log-normal distribution of the parameter roughness  $K$ , uniform distribution of rupture velocity and uniform distribution of the maximum slip with respect to the center of the fault respectively. This variability leads to the definition of 1500 stochastic slip distributions as that one showed in the panel (e). The slip distributions are place on a fault having a double length with respect to  $L$ . (f) From each simulations the PGV is directly extracted from the horizontal components of the synthetic seismograms

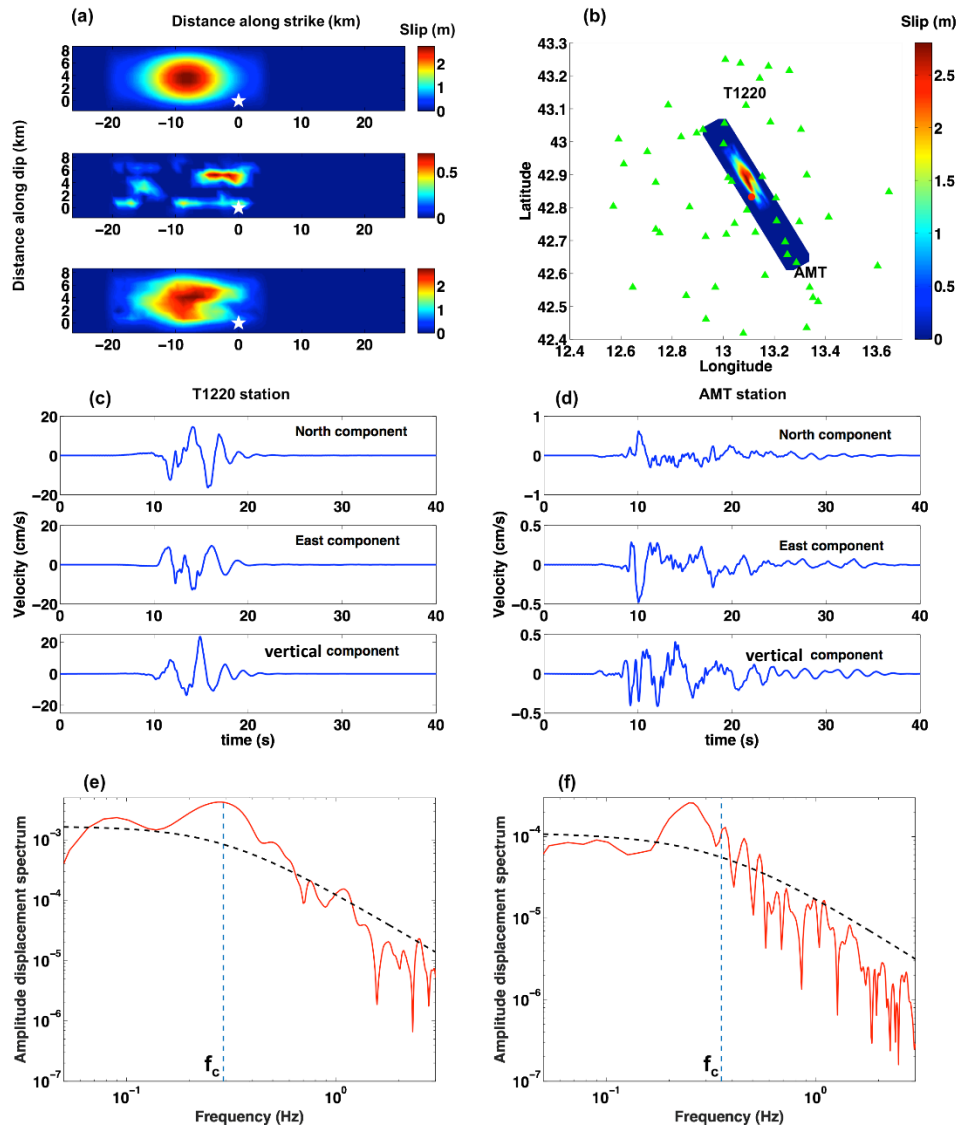


Figure 4.2: Scheme of the  $k^2$  modelling of the source: on the top the Gaussian low-frequency distribution, in the middle the stochastic distribution of the shorter wavelength slip asperities, on the bottom the final model as the summation of the low and high-frequency descriptions. (b) Projection onto the Earth's surface of the fault plane used in the forward model. On the fault projection the slip distribution is plotted. The red dot and the green triangles represent the epicenter and the used stations respectively. The texts refer to the stations whose synthetic traces are plotted in the panels (c) and (d). (e-f): the amplitude displacement spectra for the same stations of panel (c) and (d). The spectra are inverted through a classical  $f^2$  fit (black dashed lines) and the corner frequencies are extracted (blue dashed lines).

The algorithm computes the slip rate for each cell  $i$  as the average of the recorded displacements at the stations  $j$ , normalized to the distance  $R_{ij}$  and corrected for the radiation pattern  $F_{ij}$ . For stations close to the nodal plane

of a sub-source, or when there is a change of polarity in the radiation pattern for the SV component, the radiation pattern is close to zero and this may generate instability in the final solution.

To prevent this instability, for some applications, a constant average radiation pattern can be applied. This is the case, for example, of regional back-projection applications, with all the stations on the same side for the fault (Maercklin et al., 2012).

In principle, to back-project near-source data distributed all around the fault, we cannot neglect the variability of the radiation pattern. Therefore, we define a threshold level  $I_w$ , such that the effective radiation pattern  $F_{ij}$  is imposed to be equal to  $I_w$  when  $F_{ij} < I_w$ .

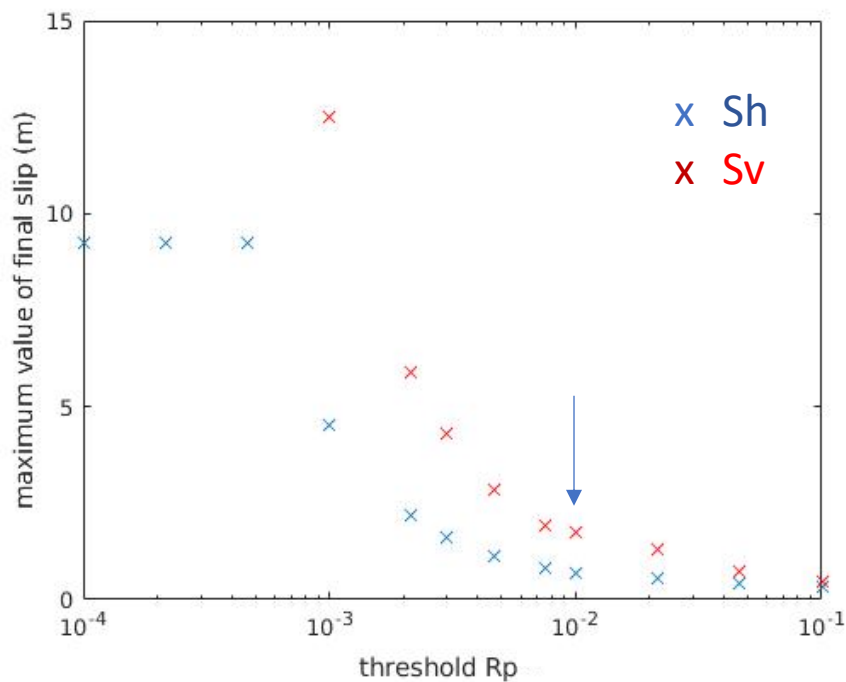


Figure 4.3: Study of stability of the final slip value varying the threshold of Radiation Pattern. The blue arrow indicates the threshold equal to 0.01.

We choose the threshold level  $I_w$  equal to 0.05 which is  $\sim 10\%$  of the average radiation pattern for the SV decomposition of the S-wave phase. We verified the adequacy of this choice, by investigating the maximum slip as a function

of the imposed threshold and evidencing how the solutions become unstable for a threshold smaller than 0.01 (Figure 4.3).

We considered all the stations within the range of distances 15-45 km (Figure 4.3 (a)) to minimize near-field effects and avoid a lack of resolution due to an excessive amplitude attenuation for distant stations. In figure 4.4 (b) the vertical displacement at the stations is shown, after the cut for S arrival time and the filtering in the low-frequency range (0.15-0.5) Hz. In figure 4.3 (c) the displacements at the stations, after the time shift with

respect to the reference station, are represented. The closest station to the

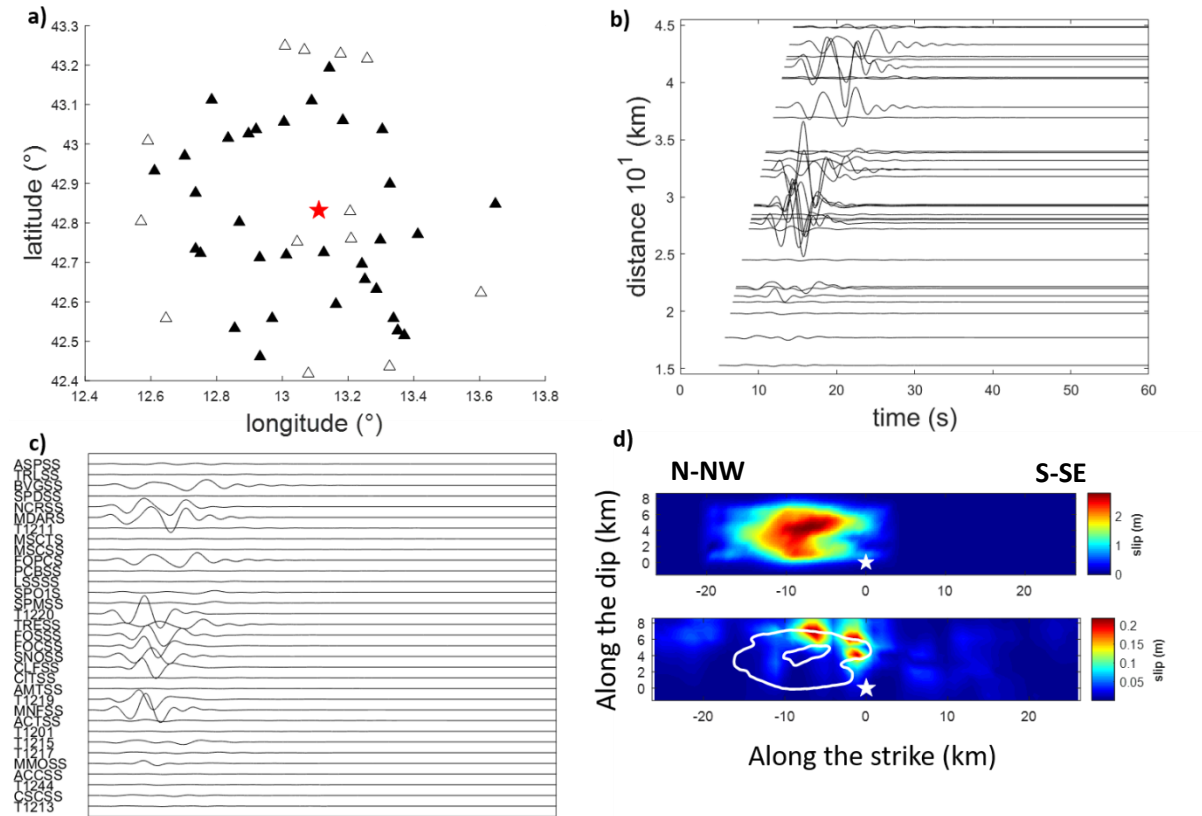


Figure 4.4: Results of back-projection back-projecting the synthetic data from all the stations within the range [15-45 km] and in the frequency band [0.15-0.50 Hz] : a) Map: epicenter is represented as a red star, stations are represented as triangles, black triangles are stations within (15-45) km, white triangles are outside of this range; b) displacement windows for stations ordered in growing distance; c) windows ready for the stacking after time shift respect the reference station, ordered in growing distance (as in b) with corresponding stations names; d) on top the "true" slip map, on the bottom interpolated slip map found by back-projection, for both top and bottom the white star represents the hypocenter and colors are for the values of slip (m). The white lines in the bottom are contour lines of "true" model for value equal to 1 and 2.5 m of slip respectively.

hypocentre is chosen as the reference station.

In figure 4.4 (d – bottom panel), the final back-projected slip is plotted along with the 1 m and 2.5 m isolines of the "true" slip model (top panel of figure 4.1 (d)). We represent the upper part of the fault (2LxW), which is the only part interested by dislocation, while in the bottom part of the fault we do

not find any significant dislocation. We remind that the exploration is done on a plane of size  $2L \times 2W$  and centred on the hypocenter. Considering the “true” model  $k^{-2}$  slip distribution, these isolines can be considered as a good proxy of the boundaries of the maximum slip patches for the long ( $k < k_c$ ) and short ( $k > k_c$ ) wavelength respectively (Figure 4.1 (a)). In this framework  $k_c$  is the corner wavenumber beyond which the slip spectral amplitude is expected to decay as  $k^{-2}$ . The position of the main patch of slip correctly reproduces the NNW orientation respect the hypocenter of the main patch of the “true” slip model. However, the maximum final slip value is about one order of smaller with respect to the maximum final slip of “true” model.

The same analysis, using the same station configuration (Figure 4.5 (a)), has been carried out for the high-frequency range [0.5-2 Hz]. As previously, in the Figures 4.5 (b) and (c) we plot the vertical displacement filtered and shifted, respectively. Differently from the previous case, the main patch of slip is now located on the 2.5 m isoline (Figure 4.5 (d)). In other words, as expected, the inversion in the low-frequency band seems to locate the boundary of portion fault interested by the longest wavelength slip patch. Conversely, the high-frequency maximum slip is retrieved at the boundary of the short wavelength maximum slip. In both cases, the directivity is correctly modeled and the maximum slip is less than 10% as compared to the “true” model. When using all stations within [15,45] km, we found that the portion of fault involved in the rupture is well located, but suffers from an underestimation of slip values as well as in reconstructing the rupture on the fault.



In this study case, stations in the North side of the hypocentre (black triangles in figure 4.6(a)) the traces show more coherency and waveforms are very similar to each other's (figure 4.6(c)). Following this idea, we investigated the solutions for NNW group.

The results of the inversion using stations in the North side of the hypocentre, for a lower frequency band are shown in figure 4.6(d). The slip imaging shows values of higher slip with respect to the case of considering all stations, with a maximum of the slip to the west of the hypocentre along the up-dip direction, in correspondence of the main patch of "true" model.

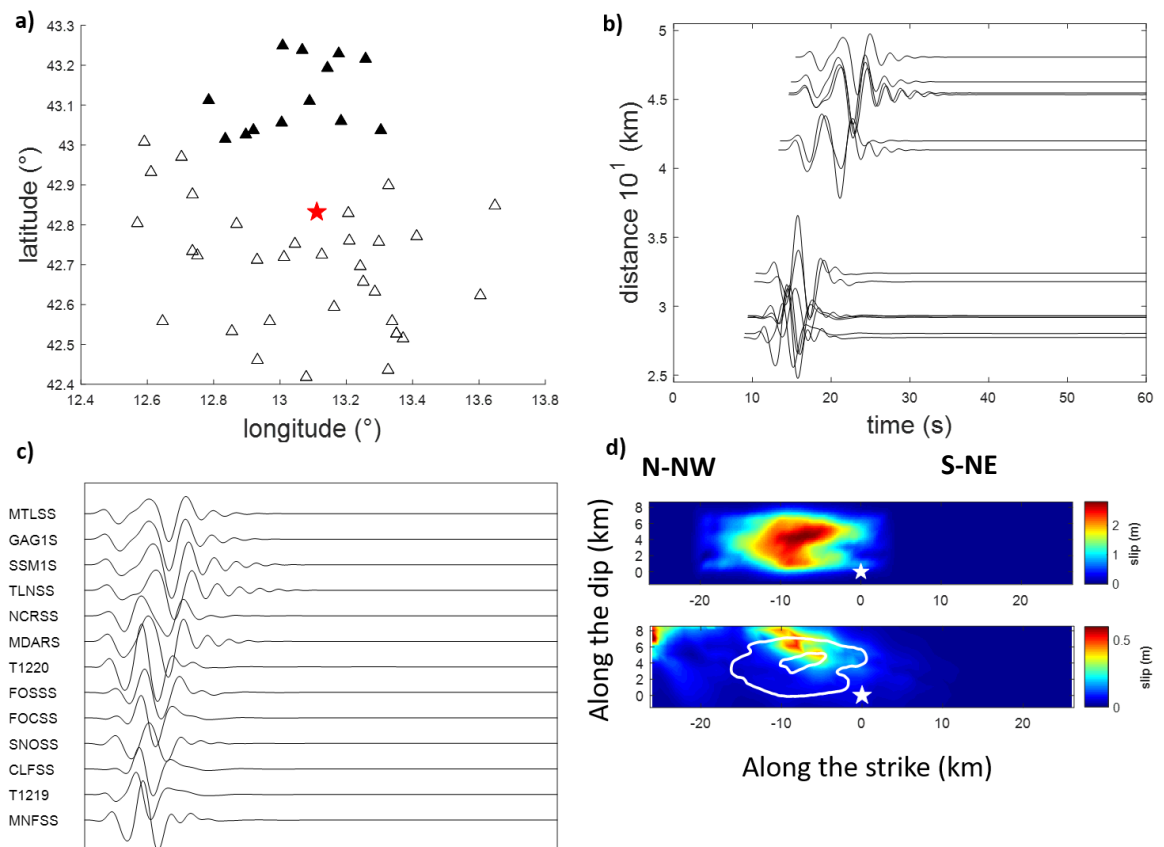


Figure 4.6: Results of back-projection back-projecting the synthetic data from North stations in the frequency band [0.15-0.5 Hz] a) Map: epicenter is represented as a red star, stations are represented as triangles, black triangles are stations in the North side of the hypocentre, white triangles are outside this selection; b) displacement windows for stations ordered in growing distance; c) windows ready for the stacking after time shift respect the reference station, ordered in growing distance (as in b) with corresponding stations names; d) on top the "true" slip map, on the bottom interpolated slip map found by back-projection, for both top and bottom the white star represents the hypocenter and colors are for the values of slip (m). The white lines in the bottom are isolines of "true" model for 1 and 2.5 m of slip respectively.

For the higher frequency band, the final back-projected slip is plotted along with the 0.25 m and 0.5 m isolines of the high-frequency  $k^{-2}$  contribution of “true” model (figure 4.7(d)). We found two maxima of final slip, one west of the hypocentre along the up-dip direction, located in the point of maximum  $k^{-2}$  contribution of “true” model, the other in the NNW direction about 20 km from the hypocentre along the direction of the strike, highlighting the border of the dislocation zone of the “true” model, although some spurious contributions appear on the boundary of the fault in the direction of the array.

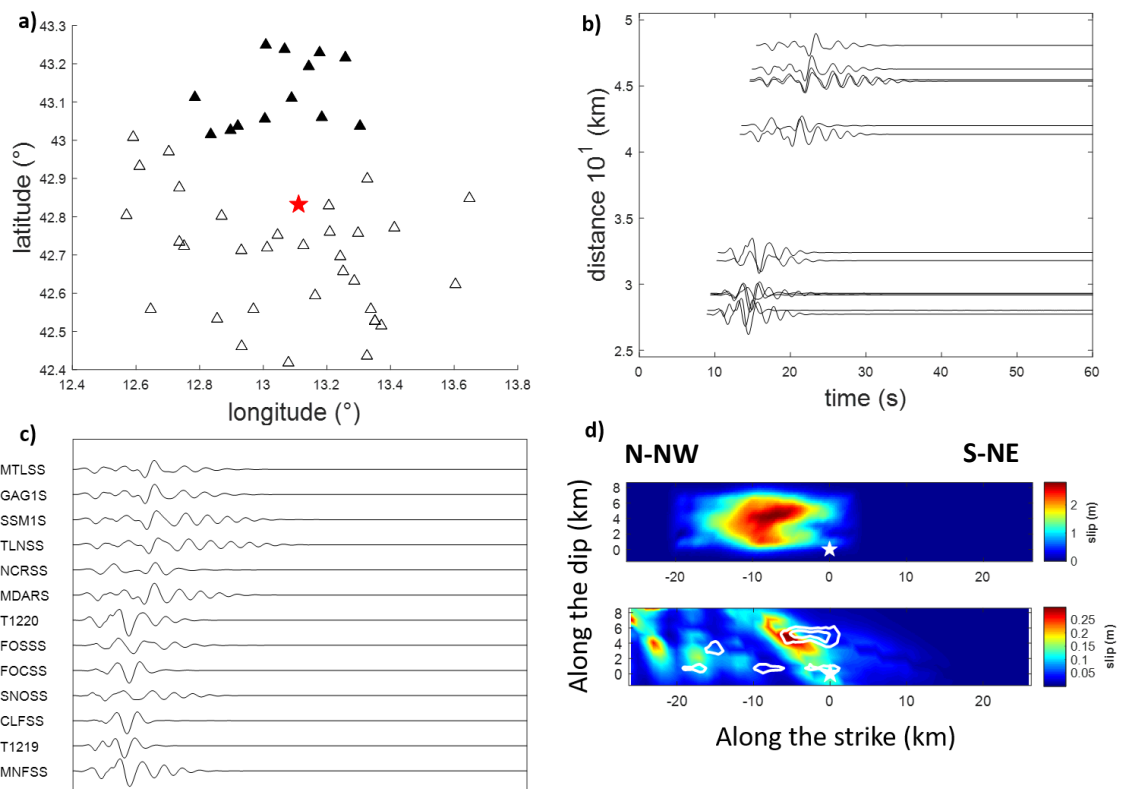


Figure 4.7: Results of back-projection back-projecting the synthetic data from North stations in the frequency band [0.5-2 Hz] a) Map: epicenter is represented as a red star, stations are represented as triangles, black triangles are stations in the North side of the hypocenter, white triangles are outside this selection; b) displacement windows for stations ordered in growing distance; c) windows ready for the stacking after time shift respect the reference station, ordered in growing distance (as in b) with corresponding stations names; d) on top the “true” slip map, on the bottom interpolated slip map found by back-projection, for both top and bottom the white star represents the hypocenter and colors are for the values of slip (m). The white lines in the bottom are contour lines of  $k^{-2}$  contribution of “true” model for 0.25 and 0.5 m of slip respectively.

Another important result of back-projection is the indirect determination of the rupture velocity. For stations in the North direction, in the low-frequency band (0.15-0.5 Hz), we consider the sub-sources that dislocated at least 10% of the maximum slip and picked the activation time of each sub-source as represented in figure 4.8 (a) in colour on the fault plane, while the black contour are contour lines for the activation time. The white line joins the points on the plane to which correspond the maximum slip rate over time. We represent the distance of the point at which occurs the maximum of slip rate in that time in Figure 4.8 (b). An approximately linear trend of the points suggests that the average rupture velocity can be considered uniform.

We estimate the average value of the rupture velocity on the fault for time less or equal to 6 s, that is the time rupture is propagating toward the shallow part of the fault, after that some spurious effects appear at the border. We obtain a velocity of  $2.4 \pm 0.3$  km/s (red line in figure 4.8 (b)), while the rupture velocity for the “true” model was set at 2.72 km/s.

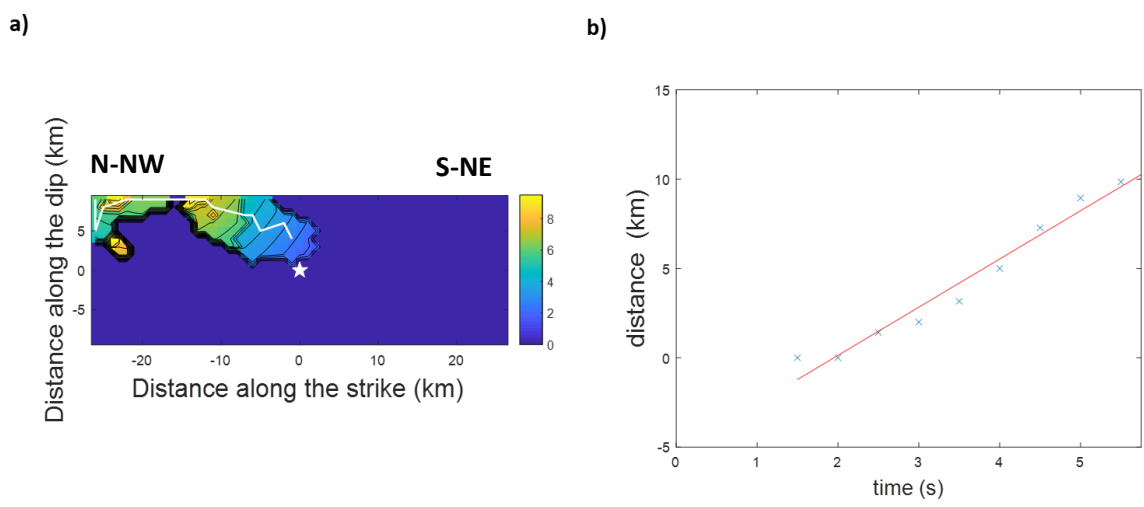


Figure 4.8: Rupture velocity: a) activation time in color on the fault of the sub-sources that have dislocated, the white star represents the hypocenter, the white line joins the points on the plane to which correspond the maximum slip rate over time; b) distance vs time corresponding to the sub-source with maximum slip rate. Red line represents the fit, of which the slope gives a rupture velocity of  $2.4 \pm 0.3$  km/s.

### 4.1.3 Application to the 2016, Mw 6.5 Norcia earthquake

We performed the stacking Back-Projection to the 2016, Mw 6.5 Norcia earthquake. We double integrated the waveforms in acceleration recorded on the vertical component at 28 stations of the RAN network (Fig 4.9 a), as in Maercklin et al., (2012). The back projection is performed on the waveform passband filtered in the lower frequency band [0.15-0.5 Hz] as we performed in the synthetic tests. We selected a window containing the S-wave (Green patch in the Fig. 4.9 b). The fault plane is centred in latitude equal to  $42.83^\circ$ , longitude  $13.11^\circ$  and a depth equal to 10 km (INGV). The plane is oriented with strike equal to  $151^\circ$  and dip equal to  $47^\circ$  (as obtained in Tarantino et al, 2019).

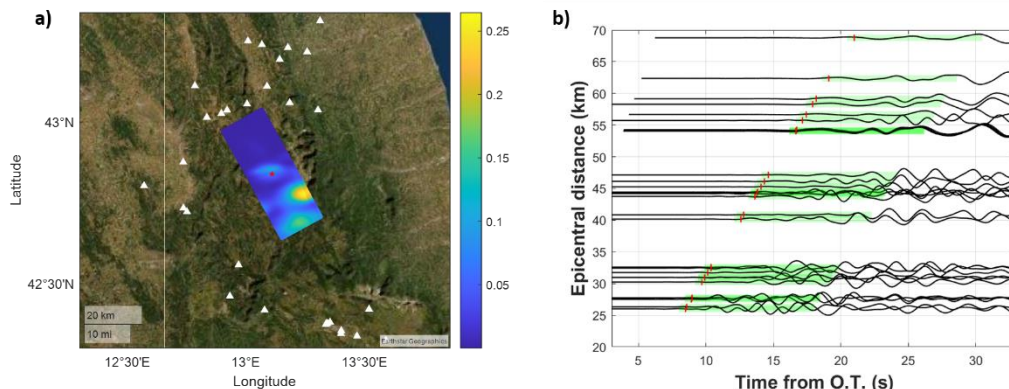


Figure 4.9: Application to real data of the 2016, Mw 6.5 Norcia earthquake: a) stations are represented as white triangles, the red star represents the epicenter, values of final slip retrieved on the fault plane investigated are plotted in color (m).

The final slip map is plotted in the 4.9 a, the maximum of final slip is 0.26 m. The highest value of final slip is located south respect the hypocenter, even if a small portion northern the hypocenter shows a no null dislocation. Indeed, the dislocation starts from the hypocenter, firstly the major slip rate is located northern to the hypocenter and then it is dominant toward S-SE with a main patch Up-Dip. This technique illuminates the regions that are affected by largest slip rate values, however we can say that the rupture starts bilateral and is almost expired at 8 s from the beginning (Figure 4.10).

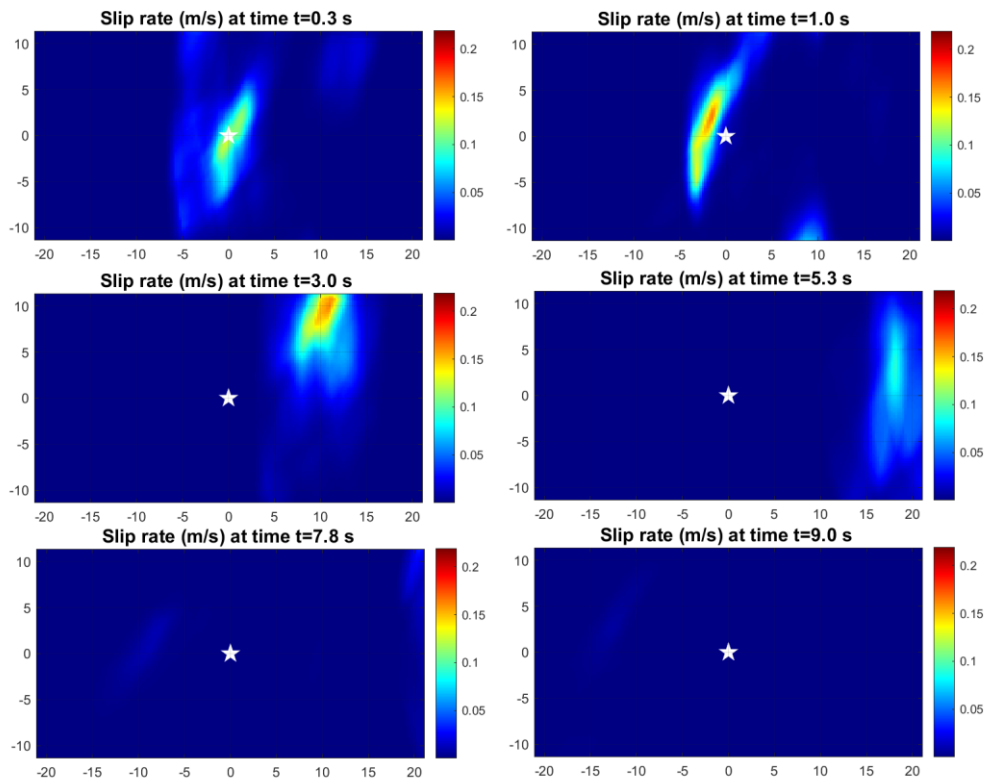


Figure 4.10: 6.5 Mw, 2016, Norcia earthquake: slip rate (m/s) in the time on the fault plane.

It was observed by Pizzi et al., (2017), and Scognamiglio et al., (2018) that the rupture model displays a modest amount of slip in the vicinity of the nucleation area. In Pizzi et al., (2017), the rupture propagates mainly updip and then continue SE. Moreover, Scognamiglio et al., (2018) inferred a complex rupture involving 2 fault planes. The earthquake rupture starts propagating on a N155° fault segment, but quite suddenly (within 1.0–2.0 s) also on a deeper N210° fault segment. During the first 4 s the coseismic rupture is propagating nearly updip and along-strike into the N210° fault segment reaching similar peak slip values ( $\sim 3$  m) on both faults.

In our analysis we retrieved smaller values (0.26 m) since we performed back-projection in a limited frequency band [0.15-0.5 Hz] and just on S-phase on the vertical component. Moreover, we assume that dislocation is all displaced in a single fault plane, not including the possibility of activation of further planes.

However, we retrieved the dominant propagation SE, after a brief propagation Northern the hypocenter and toward shallow part of the fault.

## 4.2 MULTI-ARRAY BACK PROJECTION

The Multi-Array BP method is based on the correlation stacking technique (Xie and Meng, 2020, Meng et al., 2014, Fletcher and Spudich, 2006) and described in the Chapter 1.

The station selection criteria we adopted to design a cluster depends on the density of the network. If stations are close enough (i.e., within 20 km), waveforms tend to be similar and more coherent with each other, so it is possible to investigate recorded signals at higher frequencies preserving a greater complexity of the waveforms and more information of the breaking process. On the other hand, at higher frequencies waveforms reflect the heterogeneities of the medium at a small scale. To solve this trade-off between the necessity of signals coherency, more easily obtained at lower frequency, and the necessity of getting rupture's details, visible at a higher frequency, a selection on the stations is necessary.

This is for example the case of strong-motion sensors available the 2016, 6.5 Mw Norcia Earthquake in Italy. We select the stations considering the radiation pattern and avoiding those in correspondence of the nodal planes. For example, we considered the stations in each quadrant delimited by the P-wave's nodal planes and performed separately successive alignments at increasing frequency. We have performed progressively 6 alignments at 0.05-0.1Hz, 0.05-0.2 Hz, 0.05-0.3 Hz, 0.1-0.4 Hz, 0.15-0.5, 0.15-0.6 Hz and selecting the final stations that show the highest mutual coherence of waveforms aligned to the first P-wave arrival, in the frequency band 0.05-1 Hz, based on the K-nearest-neighbour algorithm (Fix & Hodges, 1951). Otherwise, in the case of very sparse networks, we just adopt the spatially available station clusters.

For each designed cluster, we performed the BP for a specific phase, P-wave or  $S_H$  component, for example, in a selected frequency band with an appropriate time window, such as the reciprocal of the chosen frequency band central value.

The  $S_H$  component is obtained as:

$$u_{S_H}(t) = -\cos(ba) u_E(t) + \sin(ba) u_N(t)$$

where  $ba$  is the back-azimuth angle, defined as the direction from the seismic station towards a seismic source. It is  $180^\circ$  off from the azimuth and  $u_E(t)$  and  $u_N(t)$  are respectively the East component and North component. For simplicity we are rotating the components  $u_E(t)$  and  $u_N(t)$  respect to the hypocenter, of course this is an approximation. In fact, in the case of a finite source, each subsource would have its own azimuth and back-azimuth angles. For early warning

purposes, using the P-wave reduces warning times, however it is essential in the case of using the first arrival times at local distances to have a theoretical window available between the arrival of the S-wave and the arrival of the P-wave large enough to avoid contamination by the slower and more energetic S-wave.

The choice of the bands in which performing BP for single cluster depends on the coherence of the waveforms, for example in the case of Central Italy where the stations of Rete Accelerometrica Nazionale (RAN) were very dense, we chose a band of 0.05-0.5 Hz, a time window of 4 s and we performed our analysis on the vertical component focusing on the P-wave. So, in this case the choice fell on phase P because it is the fastest wave and it allows forecasts before the more energetic arrival of the S wave, responsible for higher ground intensity measures.

We applied Multi Array BP to the 2016, 6.5 Mw Norcia Earthquake (Italy), the 2015 8.3 Mw, Illapel Earthquake (Chile) and the 2010, Mw 7.2 El Mayor Cucapah Earthquake (Baja California). A map representing the epicentral location of the earthquakes is shown in Fig 4.11.

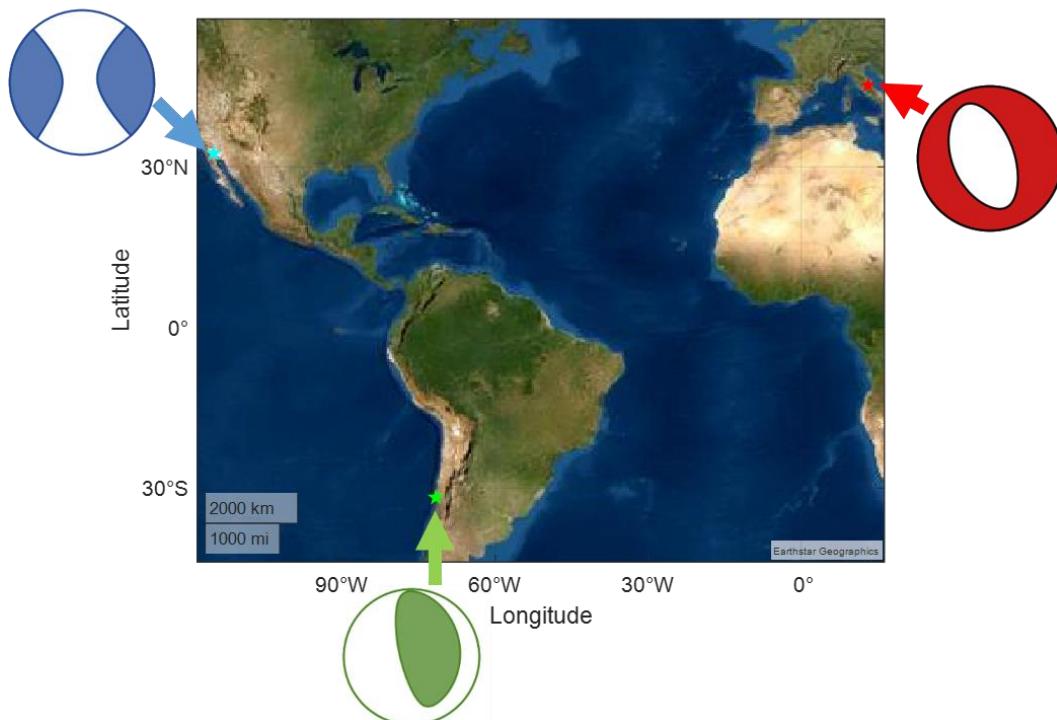


Figure 4.11: Map of analysed earthquakes with the Multi Array Back Projection

## 4.2.1 The 2015, Mw 8.3, Illapel Earthquake

The Chilean margin is under a compressive tectonic setting and a moment magnitude 8.3 earthquake occurred in 2015 at the depth of 23.3 km (red star in Figure 4.12 a) in the subduction zone. The focal mechanism was almost purely trust, with strike equal to  $353^\circ$ , dip of  $19^\circ$  and a slip angle of  $83^\circ$  (USGS).

We used the three-component accelerometric waveforms, recorded by Centro Sismológico Nacional (CSN) de la Facultad de Ciencias Físicas y Matemáticas de la Universidad de Chile. The surface accelerometers are located along the western coast of central Chile (blue squares in Figure 4.12 a). The stations are in the distance  $1^\circ$ - $2.69^\circ$  (120-300 km) and displaced in the north and in the south with respect to the hypocenter.

A single-cluster back-projection for the stations in the north (9 stations) was performed considering the  $S_H$ -component in the frequency band 0.05-0.1 Hz and a time window of 20 s, the same analysis we did for the stations in the south. For this latter cluster (23 stations), we also performed a separate back-projection for the vertical component, in the frequency band 0.05-0.2 Hz with time window 10s. Merging the results obtained from single-cluster analysis into a single image for the rupture process (see Methodology, paragraph 1.3.2) , we obtained the spatial-temporal distribution of radiators at each second and showing a good propagation toward North (Figure 4.12 (a)). Anyway, it is missing any resolution along up-dip because of the relative position of the stations with respect to the fault, unlike in Meng et al., 2018 in which the stations used were in North America, with a large distribution along with the dip.

We obtained a length of 130 km and a mean rupture speed of 2.5 km/s, which are both reasonable values (Wei et al, 2011; Mendoza et al; 2013).

Then, we wanted to check quality of source model in terms of the fit between observed and simulated Pseudo acceleration spectra. We computed the PSa, using the GMPEs for the subduction zone, in the periods 0.02-10 s (Abrahamsom et al, 2016). In figure 4.9 (b) we represented the RMSE of PSa versus period (see equation 1.5) using three different distances, firstly the distance from stations to radiators obtained in this work in regional distances and low-frequency band (blue crosses), secondly the distance from stations to radiators obtained in Meng et al,2018 in a teleseismic framework back-projection (red circles), and in conclusion

the truncated Joyner-Boore distance considering the fault extension as in An and Meng, (2017) (black squares).

The distance from low-frequency radiators shows results very similar to that with distance from high-frequency radiators, with their best performance in the period range 0.4-10 s (which translates into the frequency range 0.1-2.5 Hz) with a RMSE of  $PSa$  smaller than 0.8, this is a reasonable result (Feng & Meng, 2018). Even with higher values for RMSE, the Joyner-Boore distance has its best performance in the range 0.5-10s.

The figure 4.12 in the panel c,d,e shows residual of the PGA, which is the maximum in absolute value, in the unit of g between observation and the prediction for the 3 different metrics of distance. The predictions for the stations in the south are good enough for the PGA values estimated from high-frequency radiators (4.12 c), a slightly low overestimation for the PGA values estimated from low-frequency radiators (4.12 e) and with a more considerable overestimation of predictions obtained using Joyner-Boore distance. In the north the prediction with high-frequency radiators suffers of an overestimation, we still observed an overestimation, but with lower values, for the truncated Joyner-Boore distance and finally a general good agreement for the stations in the north for the low-frequency radiators, but with an underestimation for the station on the east border of the fault.

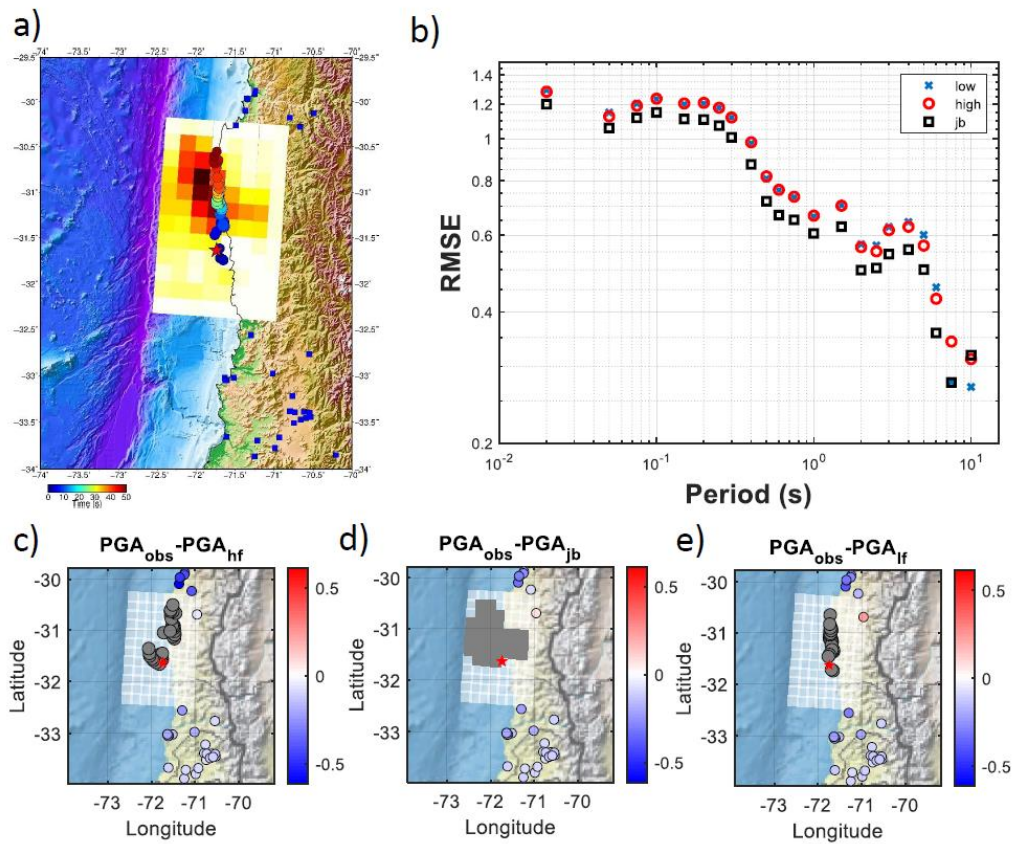


Figure 4.12: The case study of the 2015 Mw 8.3 Illapel earthquake: a) The circles are back-projection radiators color-coded by time and sized by the normalized power. The red star is the epicenter and blue squares are strong motion stations. The tiles are the slip distribution estimated by An & Meng, 2017; b) RMSE of PSA vs Period computed for stations distance from low-frequency radiators as obtained in this work (blue crosses), from high-frequency radiators by Meng et al. 2018 (red circles) and for Joyner-Boore distance considering the slip model of An & Meng, 2017 (black squares); c), d), e) white tiles represent the fault and the red star represents the epicenter, in c) the grey circles represent the 80% strongest high-frequency radiators by Meng et al. 2018 while the stations are represented as circles color-coded by the residual between the Observed PGA and the prediction based on this radiators; in d) the gray tiles represent fault portion whose dislocation exceed the 20% of the maximum of the slip (An & Meng, 2017), while the stations are the circles color-coded by the residual between the Observed PGA and the prediction based on truncated Joyner-Boore distance considering the slip model of An & Meng, 2017); in e) gray circles represent the 80% strongest low-frequency radiators obtained in this work (as in a) of this figure) and the stations are the circles color-coded by the residual between the Observed PGA and the prediction based on the low-frequency radiators.

### 4.2.2 The 2010, Mw 7.2, El Mayor Cucapah earthquake

The 2010, Mw 7.2, El Mayor Cucapah earthquake is a strike-slip event well studied in the literature (Wei et al., 2011; Mendoza et al., 2013). Studies revealed that the

mainshock involved the system of continental parallel right-lateral strike-slip faults including the San Andreas, San Jacinto and Elsinore faults matched with a system of transform faults and active spreading centres in the Gulf of California to the south (Wei et al., 2011).

We inverted the  $S_H$  component of the signal recorded at broadband stations of USArray N-NW the hypocentre for 2 clusters, respectively at the distance of 1.5-3.7° and 2.9-5.2°, in the frequency band 0.05-0.1 Hz and a time window of 20 s. We also inverted the vertical component of two clusters stations, one located North-East side the hypocentre stations at 7.80-10° and one East side at 9.1-10°, in the frequency band 0.05-0.2 Hz and a time window of 10 s (blue squares in

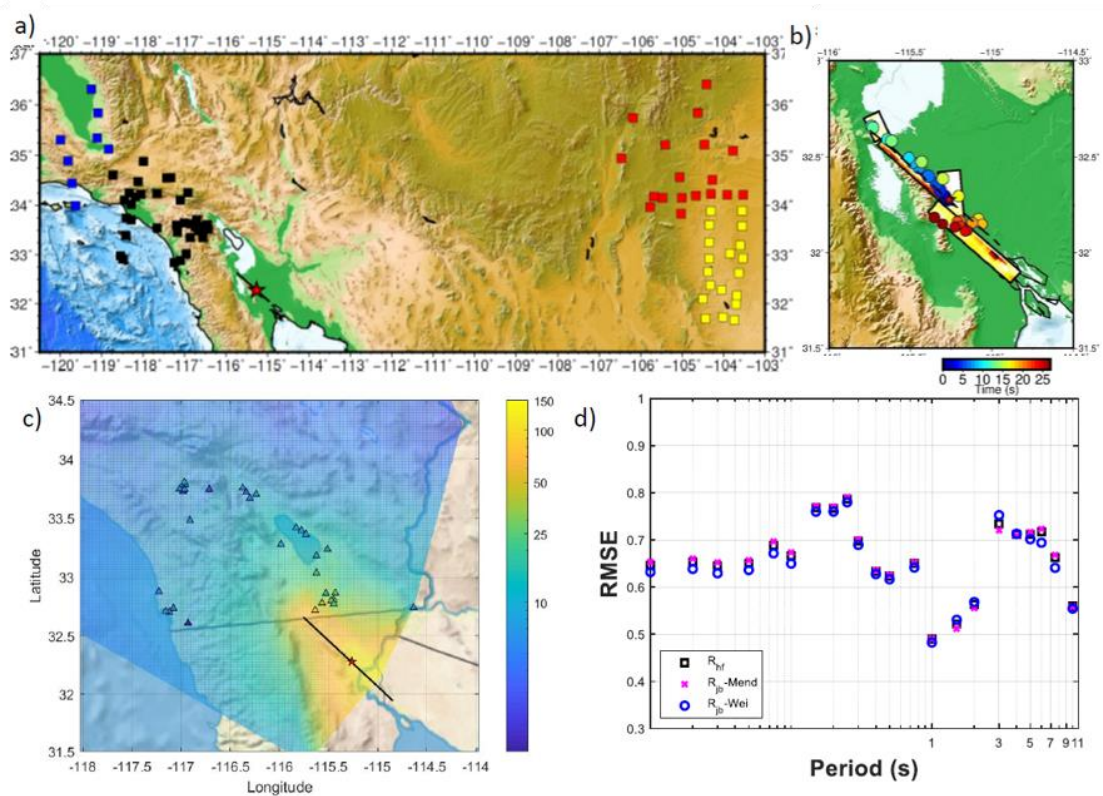


Figure 4.13: The case study of the 2010 Mw 7.2 El Mayor Cucapah earthquake: a) The red star is the epicenter and squares are strong motion stations, each colour is for different clusters, while the line fault is by Mendoza et al, 2013. b) The circles are back-projection radiators color-coded by time and sized by the normalized power. The red star is the epicenter and the black dashed line represents the trace of fault as in Mendoza et al, 2013. The tiles are the slip distribution estimated by Wei et al, 2011 ; c) In the background there is the prediction of PGV (cm/s), the red star is the epicenter, the black line is the the line fault by Mendoza et al., (2013), while the triangles represent stations color-coded for the observed peak absolute velocity; d) RMSE of  $PS_a$  vs Period computed for stations in c) considering distance from radiators (black squares) and with Joyner-Boore distance for the Mendoza et al., 2013) model (magenta crosses) and Wei et al (2011) model ( blue circles).

Figure 4.13 a, for a total of 98 stations). We used a velocity model for Southern California (Hadley & Kanamori, 1977).

Even if the earthquake involves a very complex structure, the multi-array BP technique allows for properly identifying the main rupture propagation direction along the strike (Figure 4.13 b). In this case, we find a bilateral rupture, but we are unable to provide reasonable values of the rupture speed.

The estimated length of the fault, projecting the radiators along the strike, is 85 km. The northern segment length is equal to 62 km, in agreement with previous studies (Wei et al., 2011; Meng et al., 2014), but BP gives only 23 km for the southern segment, lower than the 60 km as in Wei et al., (2011), however this underestimation is consistent with Meng et al, probably due to directive effect.

We computed the PGV and the PSa, using the GMPEs for California, in the periods 0.01-10 s (Abrahamsom et al, 2014). In figure 4.13 c we represented the PGV in the background with stations color-coded for the observed PGV in absolute value. As we can see in figure 4.13 d we represented the RMSE of PSa computed at the stations in 4.13c and obtained with radiators (black squares) and the truncated Joyner-Boore distance considering the model of Wei et al (2011) (blue circles), with a complex faults system and a simpler model, Mendoza et al., (2013), with a single fault, plotted as red crosses. Because of the frequency range in which we performed Multi Array BP, we can focus on the range 5-10s. All the distance metrics in GMPE performed similarly, obtaining RMSE of PSa always less than 0.8.

### 4.2.3 2016, Mw 6.5 Norcia earthquake

Moderate earthquakes, that occur along the NW-SE trending normal faulting system, affect Italian Apennines region and the direction of rupture propagation does not seem to be random. In fact, there is a predominant SE-SEE rupture propagation direction to the north of Amatrice up to Colfiorito, while from the northernmost part of the Campotosto fault up to Amatrice the ruptures trending is NNW-NW (Calderoni, 2017).

A seismic sequence affected the complex fault system in Central Italy in the years 2016-2017. We analysed the mainshock of Mw 6.5 in Norcia, located at 10 km of depth (red star in Figure 4.14 (a)).

We used the three-component accelerometric waveforms, recorded by Rete Accelerometrica Nazionale (RAN), and by the Istituto Nazionale di Geofisica e

Vulcanologia (INGV) and we selected stations whose waveforms showed similarity and which are at a hypocentral distance of less than 70 km.

We performed single cluster back-projection in the frequency band 0.05-0.5 Hz with a 4 s time window on the vertical component and using a 1-dimensional velocity model for Central Italy to compute travel times (Carannante et al 2013).

Merging 2 clusters, which are one South-East the source (10 stations) and the other in the west part (10 stations), even with no constraint on the fault plane, we found the right rupture propagation along strike SE-SEE (Scognamiglio et al.,2018). There is a good resolution on the up-dip projecting the radiators at the surface on the fault plane (strike=151°, dip=47°). In Figure 4.14, we represented the radiators each 0.5 s and the final slip model of Pizzi et al. (2017) on the background. The radiators are going toward the main patch.

We computed the mean rupture speed from hypocentral distance distribution versus time and we found 2.9 km/s, which is in a good agreement with reference value of 2.8 km/s (Scognamiglio et al.,2018) and a length of 13 km.

We computed 5% damping PSa (Pseudo Spectral acceleration), for all stations available from RAN and using the distance from stations to the source in ground-motion prediction equations for Italy, designed in the periods 0.04-3s (Bindi et al, 2014). In the figure 4.14 c and d we plotted RMSE for all periods between 0.02 s and 3 s considering minimum distance from stations to radiators and a truncated Joyner-Boore distance, that is the minimum distance of stations from the fault plane portions that exceeds a threshold, in this case the 20 % of the maximum slip observed on the fault.

For all stations within 200 km of distance, distance from radiators is performing similarly to the truncated Joyner-Boore distance. Values for both kinds of distance in the range 0.2-3s are less than 0.9 (Figure 4.14 (c)).

For stations with Joyner-Boore distance less than 70 km, distance from radiators is performing very similarly to the truncated Joyner-Boore distance computed

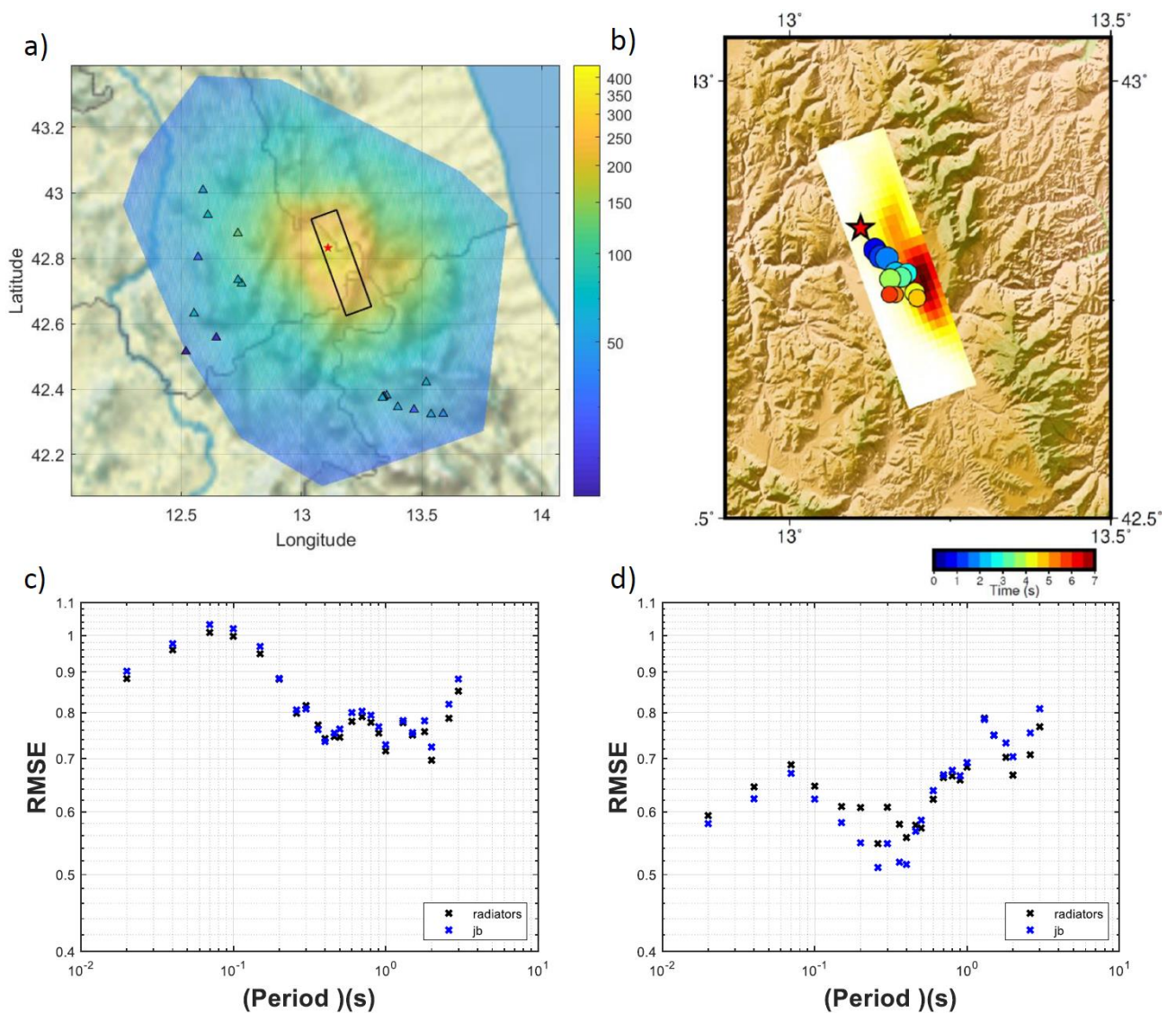


Figure 4.14: The case study of the 2016 Mw 6.5 Norcia earthquake: a) In the background there is the prediction of PGA ( $\text{cm/s}^2$ ), the red star is the epicenter, the dashed black lines are contour levels, the black line is the edge of the projected fault, while the triangles represent the stations used in the BP and their color represent the observed peak absolute acceleration b) The circles are back-projection radiators color-coded by time and sized by the normalized power. The red star is the epicenter and blue squares are strong motion stations. The tiles are the slip distribution estimated by Pizzi et al, 2017; c) RMSE of  $\text{PSa}$  vs Period in the range 0.02-3 s computed for all stations within 200 km of Joyner-Boore distance, black crosses are for distance from radiators while blue crosses are for Joyner-Boore distance; d) the same as in c, but for distance within 70 km.

respect the fault of Pizzi et al., 2017. BP is done at lower frequency ( $< 0.5$  Hz) than the GMPEs predictions and we can be more confident about our result in the domain 1-3 s, however RMSE in the case of the prediction using distance from radiators is always less than 0.8 for all periods (Figure 4.14 (d)). This is a reasonably small value (Feng & Meng, 2018).

#### 4.2.3.1 Potential implementation of the Multi Array BP in *near-real-time*

We also focused on the potential implementation of the Multi Array BP in near real time.

In a practical timeline, an early warning system with stations that record in continuous can detect an ongoing earthquake. Just a few seconds after the origin time, the location of the hypocenter could be available, performed with automatic picks at the triggered nearest stations to the source. The magnitude could be found from the average of the logarithm of the P-wave amplitude (LPDT curves, Colombelli and Zollo 2015, Nazeri et al 2019). The system could perform single array BP of strategically pre-allocated stations for the target source and merge the results into a single rupture process, providing a first order estimate of rupture length. Finally, knowing the magnitude and location of the event, as well as distance from seismic radiators, the prediction of an intensity measure can be evaluated at a target site.

The potential benefit is that it is possible to overcome the limits associated with a point source, without involving a priori knowledge on the kinematics of the rupture and without waiting for more time-consuming processing, and easier to potentially implement. However, this approach can be combined in a Bayesian framework with these pre-existing algorithms modelling the point source, implemented in EEW systems, just combining all together the single predicted ground shaking as suggested by Minson et al, 2017.

This approach is still very easy to implement and could allow to give warning about the intensity measures predicted in tempestive way, for example in the case of Mw 6.5 Norcia earthquake in Italy a warning can be issued after just 19.3 s, considering the travel time of the P-wave toward all the stations of the clusters (11.3s) and the portion of recorded signal necessary to imagine the entire rupture process. These intensity measures can be provided 1.7 s before the arrival time of S-wave at the furthest station.

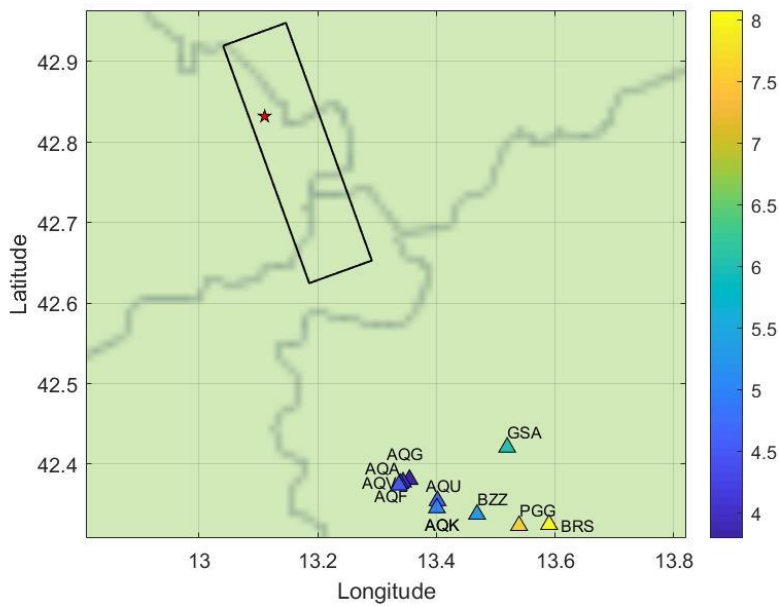


Figure 4.15: Case study Italy, stations names at the cluster at south respect hypocenter: color represents available time in seconds between the last updated prediction (thanks to the use of the distance between the station and radiators in the GMPE of Bindi et al, 2014) and occurrence of the observed maximum Peak Ground Acceleration.

However, one strategy could be to consider an evolutionary approach in which the estimation of intensity measures is updated at each time, considering the seismic radiators localized until that time. For this purpose, we focused on the south cluster (Fig 4.15). In Figure 4.16 we represent for the South cluster the prediction over time of the PGA (black crosses) with its uncertainty (GMPE of Bindi et al 2014), represented by the green patch, and the observed PGA in red. The general behaviour reflects an improvement on the final estimate in the time, with a very accurate prediction at stations *AQF*, *AQV*, *GSA* and *AQU*. Otherwise, we have a mean predicted value that is overestimating or underestimating respect the observed peak acceleration, but still consistent prediction within the uncertainties (see green patch for *AQA*, *AQG*, *AQK*, *BZZ*, *PGG* and *BRS* in Fig. 1.16). The final

maximum predicted acceleration is obtained 3.5 s before the observed maximum acceleration at *AQF* and 8 s at *BRS*.

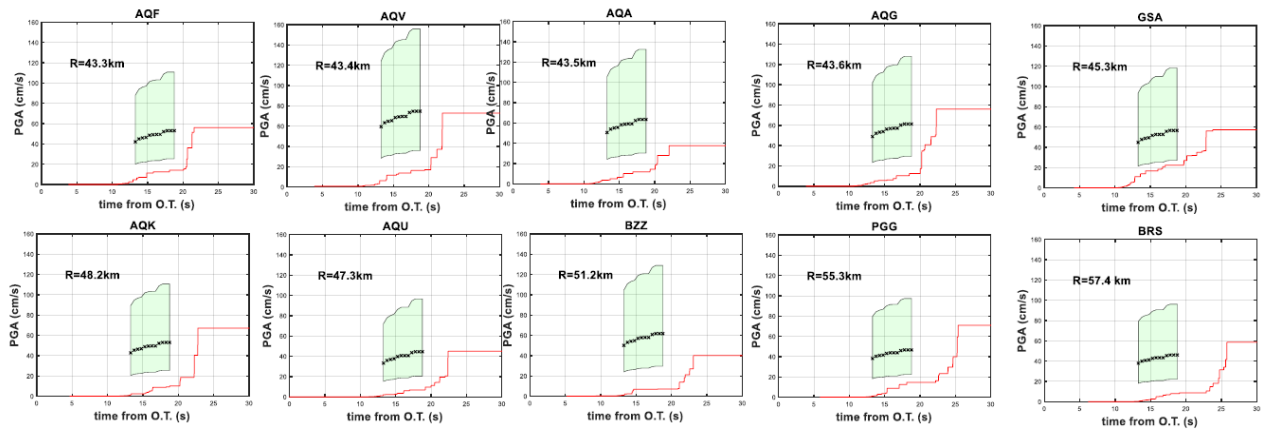


Figure 4.16: Case study Italy, stations at the cluster at south respect hypocenter: red lines represent observed absolute peak acceleration at each station, black crosses represent the predicted peak acceleration at each 0.5 s in an evolutionary approach, green patch is the uncertainty on the prediction in the GMPE of Bindi et al, 2014. Stations location are plotted in Fig. 4.13.

In the case of the Mw 8.3 Illapel earthquake, a rapid hazard shake map could be released after 2' and 21'' since the origin time. In the case of El Mayor Cucapah, the time needed before a rapid hazard shake map is available could be 2' and 58''.

The use of arrays at regional distances allows us in the case of the El Mayor Cucapah earthquake and the Illapel earthquake to be faster than teleseismic analyses which can take more than 10 minutes just for the data collection (An and Meng, 2016) and in the case of the Norcia earthquake, the use of local arrays allows a faster estimation of regional systems as well.

## 5 CONCLUSIONS

---

The general goal of this thesis has been to characterize the seismic source of an earthquake. A source can be characterized by macroscopic characteristics in the approximation of a point source, as the location of the hypocenter, moment magnitude of the event and the focal mechanism. Moreover, we can also provide characteristics of the extended source, as its spatial dimensions or the final slip map on the fault plane rather than an average value. Another punctual quantity that can be provided is rupture velocity.

The characterization of the source parameters, both in the case of the point source and extended source, can reveal essential information about the rupture process and its possible causes. In fact, an active fault system tends to be affected in time by similar earthquakes from the point of view of macroscopic characteristics. These pieces of knowledge can be used for the installation of new seismic networks, as well as helping in the mitigation of the seismic risk.

Thanks Ground Motion Predictive Equations it is possible to have fast prediction of ground shaking measures. To be robust as much as possible, it is important to be able to characterize in a more possible complete way the source in the first minutes after the origin time. That is a challenging topic and very helpful for the managing of the response emergency.

The first EEW systems treated the earthquake as a point source, but for the largest earthquakes ( $M > \sim 7.5$ ) this can lead to a significant underestimation of the ground shaking because of the underestimation of the magnitude as well as the absence of information about the location and rupture extent of the fault. Therefore, the new generation of EEW systems is proceeding in the characterization of the finite dimensions of the fault in real-time. In this perspective, we worked for the characterization of the seismic source in near-real-time. As soon as a preliminary location of an event is available, the fast estimation of the focal mechanism, together with a preliminary magnitude estimation, together with the length and width estimation (Well & Coppersmith, 1994) can be used to improve estimations of shaking map. It has been demonstrated that Fault finiteness improves EEW timeliness for users in the forward rupture direction because less time is required to issue an alert if the system identifies that the user's distance to the rupture is decreasing as the rupture propagates, and thus, the minimum magnitude to issue

an alert for a certain ground motion threshold decreases with time (Minson et al, 2018).

In this thesis, we have focused not only on the moderate-to-large events, but we have also tried to infer characteristics for micro-seismicity, believing that the latter is a key to understanding more large-scale mechanisms (De Matteis, 2012). In particular, we focused on the estimation of focal mechanism of microearthquakes ( $M_w < 3$ ).

Firstly, we have developed an algorithm in an evolutionary Bayesian framework to give a rapid estimation of the earthquake focal mechanism using the few seconds of P-wave since the origin time of a set of recording stations for moderate earthquakes ( $M_w$  4-5 to 6.5). The system can provide estimations in time that are updated each second as new data are acquired and, when a convergence condition is satisfied, a final result with its uncertainties is provided. This piece of information can be used in the improvement of the predictions of the ground shaking at a target site, in fact together with the information of the length and width of the fault, it is possible to substitute the distance receiver-hypocenter with the receiver to fault distance inside the GMPEs. Moreover, this information is needful to infer the final slip map in techniques which back projects the displacement recorded at network stations directly on the fault plane. To do that we used the peak ground acceleration, velocity and displacement measured on the vertical component in the first seconds in an increasing time window (1 to 3 s). We obtained within 6.3 to 12.7 s from origin time solutions consistent with references (mean Kagan's angle equal to  $17^\circ$ ).

Then, opportunely modifying this procedure allowing for the inclusion of S/P amplitude and inclusion of polarity, we tried to infer the focal mechanism also of micro-earthquakes (local magnitude  $< M_l$  3.0). The orientation of these small fractures and their rupture mechanism seems to be not casual but can be led by regional stress. In fact, we analysed a seismic sequence that occurred in a seismic active region of Southern Italy characterized by an extensional regime and inferred from the focal mechanism the orientation of T-axes (its average plunge and azimuth angles). This is in agreement with observations for the region (Pantosti and Valensise, 1990; Frepoli and Amato, 2000; Montone et al., 2004; DISS Working Group, 2010; Pasquale et al., 2009).

This technique to infer focal mechanism can be applied to moderate events (4.5-6.5  $M_w$ , Tarantino et al., 2019) and here we show that in offline approach can be applied to very low magnitude earthquakes integrating S/P amplitudes dataset. Specifically, this technique can be applied to events of various magnitudes by

suitably tuning the measurement windows for the amplitude peaks of the P wave and it does not require very precise picking performed by a human operator, in fact it can work with an automatic P-wave arrival time picking, even if the solutions can be multiple and not well constrained. However, this happens also for classical methods (such as with FPFIT in Festa et al,2021). In the future, we aim to interpret the stress field of the entire region of Irpinia and to deep inside the tectonic of this area. Irpinia region, in the Southern Apennines, represents an interesting open laboratory for microseismicity studies thanks to the installation of the ISNet network. This procedure could also be applied to characterize low magnitude seismicity induced by fracture stimulation in enhanced geothermal systems and fluid injection in geothermal fields thanks to high-density networks recording high-quality waveforms, which are generally installed in those regions of interest. Moreover, we believe that it could integrate automatic platforms to provide the focal mechanism for a detected and located event.

We then investigated two different approaches for back-projection. The back-projection techniques are used for the location of source contributions (nucleation and arrest phases, short wavelength asperities) at higher frequency ( $>0.1-0.2$  Hz), through the analysis of the signal coherence in narrow frequency bands. By analysing the signal coherency in moving time window, whose duration depends on the frequency band, the back-projection based on the stacking of displacement amplitudes on the sub-sources also allows tracking the evolution of the slip rate in space and time hence providing estimates of other kinematic quantities such as the rupture velocity. This approach allows imaging the major asperities of slip, especially at high-frequency, and allows identifying the areas in which the rupture ends (See synthetic test on a line source available in the Appendix).

With a beamforming and stacking amplitude displacement waveforms, we inverted the synthetic data of a simulated Mw 6.5 earthquake and we investigated two frequency ranges, 0.15-0.5 Hz (low-frequency band) and 0.5-2.0 Hz (high-frequency band). These bins are complementary to each other. It is also worth noting that the low-frequency band contains the estimated corner frequency for the event ( $\sim 0.25$  Hz).

By using all the near-source stations in the distance range 15-45 km from the hypocenter, we showed that this technique locates the main slip contributions at the boundary of the 1 m and 2.5 m isolines when we filter the data in the low frequency band. In other words, this analysis confirmed that the back-projection is able to adequately locate the position of the phase generated by the abrupt changes in the slip values at the border of the main asperities at different

wavelengths. Nevertheless, for this application, the retrieved final maximum slip amplitude is quite small (tens of centimeters) and the time-space evolution of the slip rate and the rupture velocity are incompatible with the expected directivity of the “true” model. These inconsistencies have to be investigated further, but they are possibly related to the uneven and numerically insufficient station distribution for the explored fault geometry.

By analogy with some other regional and tele-seismic previous applications (Maercklin *et al.* 2012; Satriano *et al.*, 2014) we inverted data following an array approach, that is grouping the stations as a function of their position with respect to the fault plane. The best results were obtained for the northern stations that are deployed along the directive direction of the “true” model. Although some spurious contributions appear on the boundary of the fault in the direction of the array, the boundary of the 1 m isoline is still retrieved, at least for the low-frequency band.

Then, we performed the back projection to the real data of the 2016, Mw 6.5 Norcia earthquake, retrieving the dominant rupture propagation toward south. Moreover, the duration (~8s) is in agreement with references (Pizzi *et al.*,2017; Scognamiglio *et al.*,2018).

This work shows the advantages and limitations of the approach and its ability to retrieve specific details of the kinematic rupture model. How the retrieved model could be combined with a lower frequency model in order to provide a refined and complete-frequency source description has to be investigated in the future. In particular, which is the best representation of the source for the prediction of peak ground motion. Further synthetic analyses in different source and station geometries are needed to understand whether BP could be used to provide the precise contouring of the high slip patches, previously determined by other algorithms able to constrain the low-frequency patch (i.e., SLIPNEAR, Delouis, 2014).

All the presented back-projection analysis, also including the pre-processing phase has been carried out over computational time ranging from seconds to few minutes. The process can be easily implemented in an automatic procedure to be triggered once stable solutions for the hypocenter and the source geometry are available.

The approach followed was to use the information on the macro-parameters of the fault (nucleation earthquake location, seismic moment, focal mechanism and fault length) derived from the real-time analysis of the early P-waves, which

allowed to set a preliminary location, geometry and mechanism of the fault which is used as an a priori for the following kinematic inversion. An error in the depth can generate a bias in the final slip map, as this affects the position of the sub-sources and the related travel time calculations, however for small uncertainties in the depth we do not expect large differences in the final result. As it is represented in the schematic picture of figure 5.1 the entire chain of signal processing and modelling from early P-wave signals to the late S-arrival can provide useful source kinematic models to be used for generating synthetic peak ground motion data to be integrated with observed ones in generating real-time shake-maps.

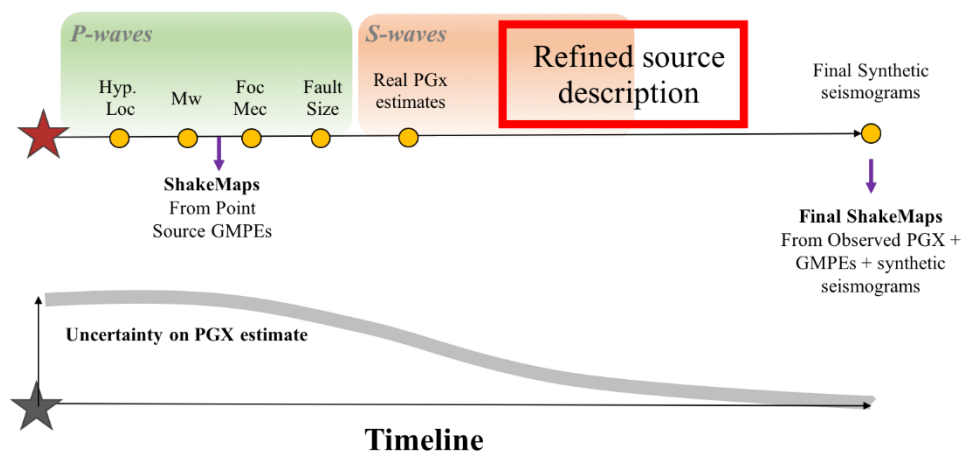


Figure 5.1: Schematic description of some of an ideal processing of data when an earthquake occurs. (top) At the occurrence of an event, moving on the timeline in the P-waves time window fast estimates of the hypocenter, magnitude and fault geometry are computed. During the recording of the S-wave phase, the real PGA estimates becomes available. The S-waves recording along with the previous estimates are hence used to compute refined source models with complementary approaches. Finally, these models can be used to compute refined synthetic seismograms and the final Shake Maps. (bottom) The definition of a refined source model is expected to reduce the uncertainty on the PGx estimates few minutes after the end of the event.

To summarize, the stacking and beamforming approach allows retrieving slip and slip rate directly on the fault plane discretized in sub-sources. The retrieved values of final slip and slip rate are referring to a narrow frequency band in which BP is performed (i.e.,  $< 0.5$  Hz), for this reason these values are smaller than the values referring to the full spectrum of the source. These values reflect the higher frequency contents, and they should be merged with values of slip at low frequency band to fully recover the final slip map of the fault. The retrieved source kinematic models can then be used for generating synthetic peak ground motion data to be integrated with observed ones in generating real-time shake-maps.

There is also a different strategy to get the estimation of ground motion measures at a site target. An example is the use of the seismic radiators. We applied the Multi-array Back-projection to study 3 different earthquakes at local and regional scales, in different tectonic regimes, to determine the location of seismic radiators and we used the distance from seismic radiators as source-to-site distance metric to considering for the path effect in local Ground Motion Prediction Equations. This technique does not require the discretization of the source in sub-sources, neither to orient the fault plane in the space. It works to match the coherency of waveforms to locate seismic radiators, which distribution reflects the main direction of the rupture and also the rupture length. Of course, if the focal mechanism is available, it is possible to infer the rupture velocity thanks to the projections of seismic radiators on the fault plane.

The results in different tectonic regimes show that the method can work in any region and without any criticality for a specific setting, this encourages us about its potential applications to monitor seismic active sources that could cause moderate to large earthquakes.

The distributions of radiators in space and in time are properly oriented toward the main patch of the final slip model in all the cases. The rupture lengths can be slightly underestimated as in the 2016 Norcia earthquakes. In fact, the Multi array Back Project can reconstruct only the south major branch of the fault, although a further north portion with respect to the hypocenter dislocates to a smaller entity than the southern branch. This is due to a directive effect, as well as in the 2010 El Mayor Cucapah, as already evident in a previous application for this event (Meng et al., 2018). Moreover, we found a rupture speed of 2.9 km/s for the Norcia earthquake, which is reasonable in agreement with reference (Scognamiglio et al., 2018).

The rupture length for the 2015 Illapel earthquake is satisfactory. However, for this event we have no resolution along with the up-dip since the stations are all from one side respect the fault. It is evident that the position of the arrays plays a key role for the scanning of the breaking process; in fact, for the other two events we have a good seismometer coverage and no lack of resolution.

To evaluate the performance of our results on the ground motion prediction, we computed the residuals between observations (PGA, PGV or PSa) and our predictions at all periods in local and site-dependent GMPE, obtaining the best results, with RMSE < 1, in the range 0.4-10 s for the 2015 Illapel earthquake and an RMSE < 0.8 for all periods for the 2010 El Mayor Cucapah, however we are more confident about our predictions in low frequencies range (periods > 1 s).

For the 2016 Norcia earthquake, the local GMPE's equations are limited until 3 s and we cannot go further, but even if we performed our BP analysis at low frequencies (0.04-0.5 Hz), we still obtain very good results with RMSE always lower than 0.8 for stations at distances less than 70 km.

The technique proves to be applicable in all contexts to determine the main rupture direction even with stations all located on one side with respect to the fault like in the Illapel earthquake case study in which the stations were all on the coast, east side of the fault, in particular North-East and South-East. However, it is desirable to have seismometers well distributed also along the dip in the case of normal and thrust faults to well resolve the seismic radiators distribution along this direction, as it has been obtained in the Norcia earthquake where we could properly find the propagation along strike, evident from other studies. This approach also provides an estimation for the rupture length and an average rupture velocity if the orientation fault is available.

Moreover, our results compare very similarly to those obtained with a truncated Joyner-Boore distance, revealing that in automatic processing this kind of distance metric could work well and without the need for fault or slip map assumptions.

We also studied a possible application of Multi array BP to integrate already existing EEW systems.

The array-based EEW system developed by Meng et al.2014, working on high frequencies, could see, if the rupture terminated abruptly with a strong stopping phase, a rupture size as large as or even larger than the low-frequency size. In this case the array sees only the strongly radiating parts of the rupture but cannot resolve a smooth rupture arrest.

Conversely, the view of the rupture obtained from low-frequency multi-array analysis is not necessarily correlated to the high-frequency aspects of the rupture process and we can miss their contribution.

Furthermore, we simulated in the case of the Norcia Earthquake the streaming of the data and we applied an evolutionary approach in which the estimation of intensity measures is updated at each time, considering the seismic radiators localized until that time. We obtained a reliable prediction for Peak Ground Acceleration seconds before the observation occurrence.

The rapidity to get ground motion prediction allowed for complementary ground motion predictions for Earthquake Early Warning purposes in the case of the

Norcia Earthquake as well as to obtain rapid hazard seismic assessment for Illapel and El mayor Cucapah earthquakes.

In the next future, we will work on an implementation of this method for the near-real-time with a magnitude target greater than  $M_w$  6.5.

We define this lower limit on the magnitude because of possible resolution limits since the technique allows to solve the rupture process of moderate to large earthquakes with rupture length  $> 10$  km (Xie and Meng, 2020). With this threshold, it is possible to include earthquakes that produce a considerable shaking of the ground motion and that in some regions of the world cause damage and deaths.

This implementation can be very suitable in already dense networks (interdistance stations 30 km), such as the RAN network in Italy, USArray in the United States and Hi-net in Japan. It could be also possible to perform a feasibility study to design the best allocation and aperture of new seismic arrays with respect to the potential seismogenic sources, based on the historical earthquakes or active faults catalogs.

Once the network has been designed, the choice of the stations in real-time is a key point to improve the quality and coherence of waveforms. A criterion can be the selection of traces after successive automatic alignment with an automatic picker and discarding the waveforms with a lower coefficient of cross-correlation, i.e., more than 0.8 (as described in Xie et al, 2020).

In conclusion, the greatest risk of an automatic system is represented by false alarms, which means that an alert has been issued, while the strong motion does not exceed the interest threshold. However, users interested in low amplitude ground motion thresholds and those who are concerned with strong ground motion but who are willing to receive many needless alerts in exchange for receiving timely warnings can obtain the greatest benefits from the EEW systems (Minson et al, 2018).

# References:

Abrahamson, N., Gregor, N., & Addo, K.: BC Hydro ground motion prediction equations for subduction earthquakes, ES, 2016

Abrahamson, N. A., Silva, W. J., & Kamai, R.: Summary of the ASK14 ground motion relation for active crustal regions, ES, 2014

Aki, K., and P. Richards (2000). Quantitative Seismology, University Science Books, Sausalito, California.

Allen, R. V. (1978). Automatic earthquake recognition and timing from single traces, *Bull. Seismol. Soc. Am.* 68, 1521–1532.

Allen, R. M., and Kanamori, H. (2003), The potential for earthquake early warning in Southern California, *Science*, **300**, 786–789, doi:10.1126/science.1080912.

Allen, R.M., P. Gasparini, O. Kamigaichi and M. Bose, (2009), The Status of Earthquake Early Warning around the World: An Introductory Overview, *Seismol Res Lett*, **80**(5), 682-693, doi 10.1785/gssrl.80.5.682.

An & Meng, (2016) Application of array backprojection to tsunami prediction and early warning, *GRL*, *43*, 3677-3685, doi <https://doi.org/10.1002/2016GL068786>

Bernard, P., Herrero, A. and Berge, C., 1996, Modeling directivity of heterogeneous earthquake ruptures, *Bull. Seism. Soc. Am.* 86, 1149–1160

Bindi et al: Ground Motion Prediction Equations Derived from the Italian Strong Motion Database, BEE, 2011

Bobbio A. Vassallo M., and Festa G. (2009), A local magnitude scale for southern Italy, *Bull. Seismol. Soc. Am.* **99**, 2461–2470

Boore, D. M. and Joyner, W.B. (1982) The empirical prediction of ground motion, *Bull. Seism. Soc. Am.*, **72**, S269–S268.

Böse, M., E. Hauksson, K. Solanki, H. Kanamori, and T. H. Heaton (2009), Real-time testing of the on-site warning algorithm in southern California and its performance during the July 29 2008, Mw5.4 Chino Hills earthquake, *Geophys. Res. Lett.*, **36**, L00B03, doi:10.1029/2008GL036366.

Böse, M., T. H. Heaton, and E. Hauksson (2012). Real-time finite fault rupture detector (FinDer) for large earthquakes, *Geophys. J. Int.* 191, no. 2, 803–812, doi: 10.1111/j.1365-246X.2012.05657.x.

Brillinger, D. R., A. Udías, and B. A. Bolt (1980). A probability model for regional focal mechanism solutions, *Bull. Seismol. Soc. Am.* 70, 149–170.

Calderoni, G., Rovelli, A., & Di Giovambattista, R. (2017). Rupture directivity of the strongest 2016–2017 central Italy earthquakes. *Journal of Geophysical Research: Solid Earth*, 122, 9118–9131. <https://doi.org/10.1002/2017JB014118>

Carannante, S., G. Monachesi, M. Cattaneo, A. Amato, and C. Chiarabba (2013), Deep structure and tectonics of the northern-central Apennines as seen by regional-scale tomography and 3-D located earthquakes, *J. Geophys. Res. Solid Earth*, 118, 5391–5403, doi:10.1002/jgrb.50371.

Carranza Gómez, M. (2016). Sistema de alerta sísmica temprana para el sur de la Península Ibérica: determinación de los parámetros de la alerta, Ph.D. Thesis, available at <https://eprints.ucm.es/44161/1/T39045.pdf> (last accessed July 2018) (in Spanish).

Causse, M., Chaljub, E., Cotton, F., Cornou, C., Bard, P.Y. (2009). New approach for coupling  $k_2$  and empirical Green's functions: Application to the blind prediction of broadband ground-motion in the Grenoble Basin. *Geophysical Journal International*, 179(3), 1627–1644. <https://doi.org/10.1111/j.1365-246X.2009.04354.x>

Cesca, S., S. Heimann, and T. Dahm (2011). Rapid directivity detection by azimuthal amplitude spectra inversion, *J. Seismol.* 15, no. 1, 147–164, doi: 10.1007/s10950-010-9217-4.

Chiarabba, C.; Jovane, L.; Distefano, R. A new view of Italian seismicity using 20 years of instrumental recordings. *Tectonophysics* **2005**, 395, 251–268.

Chiaraluce, L., R. Di Stefano, E. Tinti, L. Scognamiglio, M. Michele, E. Casarotti, M. Cattaneo, P. De Gori, C. Chiarabba, G. Monachesi, et al. (2017). The 2016 central Italy seismic sequence: A look at the mainshocks, aftershocks and source models, *Seismol. Res. Lett.* 88, no. 3, doi: 10.1785/0220160221.

Chopra, A. K. (2001). *Dynamics of structures: Theory and applications*.

Colombelli, S., and A. Zollo (2015). Fast determination of earthquake magnitude and fault extent from real-time P-wave recordings, *Geophys. J. Int.* 202, no. 2, doi: 10.1093/gji/ggv217.

Colombelli, S., A. Zollo, G. Festa, and H. Kanamori (2012). Early magnitude and potential damage zone estimates for the great Mw 9 Tohoku-Oki earthquake, *Geophys. Res. Lett.* 39, L22306, doi: 10.1029/2012GL053923.

Colombelli, S., A. Zollo, G. Festa, and M. Picozzi (2014). Evidence for a difference in rupture initiation between small and large earthquakes, *Nature Comm.* 5, Article Number 3958, doi: 10.1038/ncomms4958.

De Matteis, R., V. Convertito, and A. Zollo (2016). BISTROP: Bayesian inversion of spectral-level ratios and P-wave polarities for focal mechanism determination, *Seismol. Res. Lett.* 87, no. 4, 944–954, doi: 10.1785/0220150259.

De Matteis, R.; Matrullo, E.; Rivera, L.; Stabile, T.A.; Pasquale, G.; Zollo (2012), A. Fault Delineation and Regional Stress Direction from the Analysis of Background Microseismicity in the southern Apennines, Italy. *Bull. Seism. Soc. Am.*, 102, 1899–1907.

De Landro, G.; Amoroso, O.; Stabile, T.A.; Matrullo, E.; Lomax, A.; Zollo, (2015) A. High-precision differential earthquake location in 3-D models: Evidence for a rheological barrier controlling the microseismicity at the Irpinia fault zone in southern Apennines. *Geophys. J. Int.* , 203, 1821–1831.

Delouis, B. (2014). FMNEAR: Determination of focal mechanism and first estimate of rupture directivity using near-source records and a linear distribution of point sources, *Bull. Seismol. Soc. Am.* 104, no. 3, 1479–1500.

DISS Working Group (2010). Database of Individual Seismogenic Sources (DISS), Version 3.1.1: A compilation of potential sources for earthquakes larger than M 5.5 in Italy and surrounding areas: available from the Istituto Nazionale di Geofisica e Vulcanologia (INGV) at <http://diss.rm.ingv.it/dissNet/> (last accessed July 2011).

Dreger, D. S. (2003). 85.11 TDMT\_INV: Time domain seismic moment tensor inversion, *Int. Geophys.* 81, 1627.

Dreger, D. S., and D. V. Helmberger (1993). Determination of source parameters at regional distances with three-component sparse network data, *J. Geophys. Res.* 98, 8107–8125.

Emolo, A.; Convertito, V.; Cantore, L. (2011) Ground-motion predictive equations for low-magnitude earthquakes in the Campania– Lucania area, Southern Italy. *J. Geophys. Eng.* , 8, 46–60

Fang, S., S. Huang, R. Srinivasan, and R. Raghavan (1996). Deformable volume rendering by 3D texture mapping and octree encoding, *Proc. of the IEEE Visualization Conference*, 73–80, doi: 10.1109/VISUAL.1996.567609.

Feng & Meng: A High-Frequency Distance Metric in Ground-Motion Prediction Equations Based on Seismic Array Backprojections, *GRL*, 2018

Festa, G.; Adinolfi, G.M.; Caruso, A.; Colombelli, S.; De Landro, G.; Elia, L.; Emolo, A.; Picozzi, M.; Scala, A.; Carotenuto, F.; et al. (2021). Insights into Mechanical Properties of the 1980 Irpinia Fault System from the Analysis of a Seismic Sequence. *Geosciences*, 11, 28. <https://doi.org/10.3390/geosciences11010028>

Festa, G. and A. Zollo, 2012. From data to source parameters: kinematic modeling

Fix, Evelyn; Hodges, Joseph L. (1951). *Discriminatory Analysis. Nonparametric Discrimination: Consistency Properties* . USAF School of Aviation Medicine, Randolph Field, Texas.

Frepoli, A.; Amato, A. (1997) Contemporaneous extension and compression in the Northern Apennines from earthquake fault-plane solutions. *Geophys. J. Int.*, 129, 368–388.

Funasaki, J. and Earthquake Prediction Information Division (2004): Revision of the JMA Velocity Magnitude (in Japanese), *Quart. J. Seis.*, 67, 11 – 20.

Gallovič, F., Brokešová, J. (2004). On strong ground motion synthesis with  $k^2$  slip distributions, *J. Seismology*, 8, 211-224, doi:10.1023/B:JOSE.0000021438.79877.58

Gallovič, F., Imperatori, W., & Mai, P. M. (2015). Effects of three-dimensional crustal structure and smoothing constraint on earthquake slip inversions: case study of the  $M_w$ 6.3 2009 L'Aquila earthquake. *Journal of Geophysical Research: Solid Earth*, 120, 428– 449. <https://doi.org/10.1002/2014JB011650>

Goldstein, P., D. Dodge, M. Firpoand, and L. Minner (2003). SAC2000: Signal processing and analysis tools for seismologists and engineers, in *The IASPEI International Handbook of Earthquake and Engineering Seismology*, W. H. K. Lee, H. Kanamori, P. C. Jennings, and C. Kisslinger (Editors), Academic Press, London.

Joyner, W. B. and D. M. Boore (1981), Peak horizontal acceleration and velocity from strong-motion records including records from the 1979 Imperial Valley, California, earthquake, *Bull. Seism. Soc. Am.* 71, 2011-2038.

Kagan, Y. Y. (1991). 3-D rotation of double-couple earthquake sources, *Geophys. J. Int.* 106, no. 3, 709–716, doi: 10.1111/j.1365- 246X.1991.tb06343.x.

Kanamori, H. (2005), Real-time seismology and earthquake damage mitigation, *Annu. Rev. Earth Planet. Sci.*, **33**, 195–214, doi: 10.1146/annurev.earth.33.092203.122626.

Kanamori, H., (1983), Global seismicity, in *Earthquakes: Observation, Theory and Interpretation*, Proceedings of International School of Physics "Enrico Fermi," course LXXXV, edited by H. Kanamori and E. Boschi, pp. 596-608, North-Holland, Amsterdam.

Kiser, E., & Ishii, M., (2013). Hidden aftershocks of the 2011 Mw~9.0 Tohoku, Japan earthquake imaged with the backprojection method. *J. Geophys. Res* **118**, 5564-5576, doi:10.1002/2013JB010158.

Hadley D., Kanamori H., (1977). Seismic structure of the transverse ranges, California, *Bull. geol. Soc. Am.*, 88, 1469–1478 [10.1130/0016-7606\(1977\)88%3c1469:SSOTTR%3e2.0.CO;2](https://doi.org/10.1130/0016-7606(1977)88%3c1469:SSOTTR%3e2.0.CO;2)

Hardebeck, J., and M. Shearer (2003). Using S/P amplitude ratios to constrain the focal mechanisms of small earthquakes, *Bull. Seismol. Soc. Am.* 93, no. 6, 2434–2444, December 2003.

Hoshiya, M. (2013), Real-time prediction of ground motion by Kirchhoff-Fresnel boundary integral equation method: Extended front detection method for earthquake early warning. *Journal of Geophysical Research: Solid Earth*, **118**(3):1038-1050.

Hoshiya, M. and Aoki, S. (2015), Numerical shake prediction for earthquake early warning: Data assimilation, real-time shake mapping, and simulation of wave propagation. *Bulletin of the Seismological Society of America*, **105**(3):1324-1338

Improta, L.; De Gori, P.; Chiarabba, C. (2014) New insights into crustal structure, Cenozoic magmatism, CO<sub>2</sub>degassing, and seismogenesis in the southern Apennines and Irpinia region from local earthquake tomography. *J. Geophys. Res. Solid Earth*, 119, 8283–8311.

Ishii, M., (2011). High-frequency rupture properties of the Mw 9.0 Off-the-Pacific-Coast-of-Tohoku earthquake. *Earth, Planets, Space* **63**, 609-614.

Lomax A. and A. Curtis (2001). *Fast, probabilistic earthquake location in 3D models using oct-tree importance sampling*. *Geophys. Res. Abstr.* **3**, 955.

Lomax A., Virieux J., Volant P., and C. Berge-Thierry (2000), Probabilistic Earthquake Location in 3D and Layered Models. In: Thurber C.H., Rabinowitz N. (eds) *Advances in Seismic Event Location. Modern Approaches in Geophysics*, vol 18. *Springer*, Dordrecht.

Lomax, A. (2005), A reanalysis of the hypocentral location and related observations for the great 1906 California earthquake, *Bull. Seismol. Soc. Am.*, **95**, 861–877.

Lomax, A., S. Satriano and M. Vassallo, (2012), Automatic picker developments and optimization: FilterPicker - a robust, broadband picker for real-time seismic monitoring and earthquake early-warning, *Seism. Res. Lett.*, **83**, 531-540, doi: 10.1785/gssrl.83.3.531

Kaka, S. I., and G. M. Atkinson (2004). Relationships between instrumental ground motion parameters and Modified Mercalli Intensity in eastern North America, *Bull. Seism. Soc. Am.* 94, no. 5, 1728–1736.

Maercklin, N., Festa, G., Colombelli, S., & Zollo, A. (2012). Twin ruptures grew to build up the giant 2011 Tohoku, Japan, earthquake. *Scientific Reports*, **2**(1), 709. <https://doi.org/10.1038/srep00709>

Melgar, D., Allen, R. M., Riquelme, S., Geng, J., Bravo, F., Baez, J. C., Parra, H., Barrientos, S., Fang, P., Bock, Y., & Bevis, M. (2016). Local tsunami warnings: Perspectives from recent large events. *Geophysical Research Letters*, **43**, 1109– 1117. <https://doi.org/10.1002/2015GL067100>

Melgar, D., & Bock, Y. (2013). Near-field tsunami models with rapid earthquake source inversions from land-and ocean-based observations: The potential for forecast and warning. *Journal of Geophysical Research: Solid Earth*, **118**, 5939– 5955. <https://doi.org/10.1002/2013JB010506>

Melgar, D., & Bock, Y. (2015). Kinematic earthquake source inversion and tsunami runup prediction with regional geophysical data. *Journal of Geophysical Research: Solid Earth*, **120**, 3324– 3349. <https://doi.org/10.1002/2014JB011832>

Mendoza, C. and Hartzell, S., 2013. Finite-fault source inversion using teleseismic P waves: Simple parameterization and rapid analysis. *Bull. Seis. Soc. Am.* 103(2A), 834-844.

Meng, L., Allen, R. M., & Ampuero, J. P. (2014). Application of seismic array processing to earthquake early warning. *Bulletin of the Seismological Society of America*, **104**(5), 2553– 2561. <https://doi.org/10.1785/0120130277>

Meng, L., Inbal, A., & Ampuero, J. P. (2011). A window into the complexity of the dynamic rupture of the 2011 Mw 9 Tohoku-Oki earthquake. *Geophysical Research Letters*, **38**, L00G07. <https://doi.org/10.1029/2011GL048118>

Meng, L., Zhang, A., & Yagi, Y. (2016). Improving back projection imaging with a novel physics-based aftershock calibration approach: A case study of the 2015 Gorkha earthquake. *Geophysical Research Letters*, **43**, 628– 636. <https://doi.org/10.1002/2015GL067034>

Michele, M., S. Custódio, and A. Emolo (2014). Moment tensor resolution: Case study of the Irpinia seismic network, southern Italy, *Bull. Seismol. Soc. Am.* 104, no. 3, 1348–1357, doi: 10.1785/0120130177.

Minson S. E., Simons M. and J. L. Beck (2013), Bayesian inversion for finite fault earthquake source models I—theory and algorithm, *Geophysical Journal International*, **194** (3), 1701–1726, <https://doi.org/10.1093/gji/ggt180>.

Montone, P., M. T. Mariucci, S. Pondrelli, and A. Amato (2004). An improved stress map for Italy and surrounding regions (central Mediterranean), *J. Geophys. Res.* 88, no. B10410, 22, doi 10.1029/2003JB002703.

Nakamura, Y., J. Saita, T. Sato, On an earthquake early warning system (EEW) and its applications, *Soil Dynamics and Earthquake Engineering*, Volume 31, Issue 2, 2011, Pages 127-136, ISSN 0267-7261, <https://doi.org/10.1016/j.soildyn.2010.04.012>

Nazeri, S., S. Colombelli, and A. Zollo (2018). Straightforward approach to quickly characterize the earthquake magnitude and the expected length of the rupture, *Geophys. Res. Abstr.* 20, EGU2018–17506.

Pantosti, D.; Schwartz, D.P.; Valensise, G. Paleoseismology along the 1980 surface rupture of the Irpinia Fault: Implications for earthquake recurrence in the southern Apennines, Italy. *J. Geophys. Res. Solid Earth* **1993**, 98, 6561–6577

Pantosti, D., and G. Valensise (1990). Faulting mechanism and complexity of the 23 November, 1980, Campania–Lucania earthquake inferred from surface observations, *J. Geophys. Res.* 95, no. B10, 15,319– 15,341, doi 10.1029/JB095iB10p15319.

Petersen, G. M., Cesca, S., Heimann, S., Niemz, P., Dahm, T., Kühn, D., Kummerow, J., Plenefisch, T., and AlpArray working group, T.: Implications on recent tectonics in the Alps from centroid moment tensor inversion of weak to moderate seismicity, EGU General Assembly 2021, online, 19–30 Apr 2021, EGU21-3164, <https://doi.org/10.5194/egusphere-egu21-3164>, 2021.

Pizzi, A., A. Di Domenica, F. Gallovič, L. Luzi, R. Puglia (2017). Fault segmentation as constraint to the occurrence of the main shocks of the 2016 Central Italy seismic sequence, *Tectonics*, doi: 10.1002/2017TC004652.

Reasenber, P.; Oppenheimer, D. (1985) FPFIT, FPLOT and FPPAGE: Fortran Computer Programs for Calculating and Displaying Earthquake Fault-Plane Solutions; Open File Report 85–739; US Geological Survey: Menlo Park, CA, USA; pp. 85–739.

Satriano, C., Elia L., Martino C., Lancieri M., Zollo A. and G. Iannaccone (2011), PRESTo, the earthquake early warning system for Southern Italy: concepts, capabilities and future perspectives. *Soil Dyn. Earthq. Eng.* **31** (2), 137–153, doi: 10.1016/j.soildyn.2010.06.008.

Satriano, C., Lomax, A., & Zollo, A. (2008), Real-Time Evolutionary Earthquake Location for Seismic Early Warning, *Bull. Seismol. Soc. Am.*, **98**, 1482–1494, doi: 10.1785/0120060159.

Scognamiglio, L., Tinti, E., Casarotti, E., Pucci, S., Villani, F., Cocco, M., et al. (2018). Complex fault geometry and rupture dynamics of the MW 6.5, 30 October 2016, central Italy earthquake. *Journal of Geophysical Research: Solid Earth*, 123, 2943–2964. <https://doi.org/10.1002/2018JB015603>

Sokos, E. N., and J. Zahradník (2008). ISOLA a FORTRAN code and a MATLAB GUI to perform multiple-point source inversion of seismic data, *Comput. Geosci.* 34, 967–977.

Tarantino S., S. Colombelli, A. Emolo, A. Zollo; (2019) Quick Determination of the Earthquake Focal Mechanism from the Azimuthal Variation of the Initial *P*-Wave

Amplitude. *Seismological Research Letters*; 90 (4): 1642–1649.  
doi: <https://doi.org/10.1785/0220180290>

Tarantola A. (1987). *Inverse problem theory*. Elsevier.

Xie, Y, Bao, H, & Meng, L.: Coseismic behaviors of the 2019 M 6.4 and M 7.1 Ridgecrest earthquakes inferred from local and teleseismic backprojections, GRL, 2020

Xie, Y. & Meng, L. (2020). A multi-array back-projection approach for tsunami warning. *Geophysical Research Letters*, 47, e2019GL085763. <https://doi.org/10.1029/2019GL085763>

Wald, D. J., V. Quitoriano, T. H. Heaton, and H. Kanamori (1999). Relationships between peak ground acceleration, peak ground velocity, and Modified Mercalli intensity in California, *Earthquake Spectra* 15, no. 3, 557–564.

Wei, S., Fielding, E., Leprince, S. et al. (2011) Superficial simplicity of the 2010 El Mayor–Cucapah earthquake of Baja California in Mexico. *Nature Geosci* 4, 615–618. <https://doi.org/10.1038/ngeo1213>

Wessel, P., and W. H. F. Smith (1995). New version of the Generic Mapping Tools released, *Eos Trans. AGU* 76, 329.

Zahradník, J., J. Janský, and K. Papatsimpa (2001). Focal mechanisms of weak earthquakes from amplitude spectra and polarities, *Pure Appl. Geophys.* 158, 647–665, Birkhäuser Verlag, Basel, Switzerland.

Zollo, A., and B. Bernard (1991). Fault mechanism from near source data: Joint inversion of S polarization and P polarities, *Geophys. J. Int.* 104, 441–451.

Zollo, A. and A. Emolo (2011). *Terremoti e Onde. Metodi e pratica della sismologia moderna*.

Zollo, A., A. Orefice, and V. Convertito (2014). Source parameter scaling and radiation efficiency of microearthquakes along the Irpinia fault zone in southern Apennines, Italy, *J. Geophys. Res.* 119, no. 4, 3256–3275, doi: 10.1002/2013JB010116

# Appendix:

## Estimation of focal mechanism

We report in figure A1 the prior PDF at first step, combination of a Gaussian function (centered at strike = 150°, dip = 45° and slip = -90°) with a cosine taper function at the edge of the space, to smooth the transition toward zero.

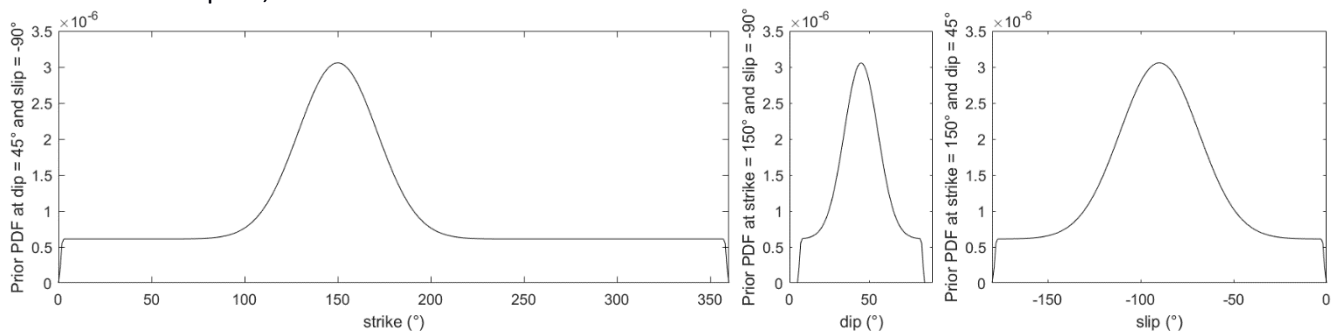


**Figure A1.** Prior Probability Density Function (PDF).

We extracted for each event the attenuation coefficients  $c$  in the relations:

$$\log_{10}(P_*) = a' + c \log_{10}(dist)$$

Both using velocity and displacements.

The mean values are used to correct for the distance the velocity and displacement amplitudes.

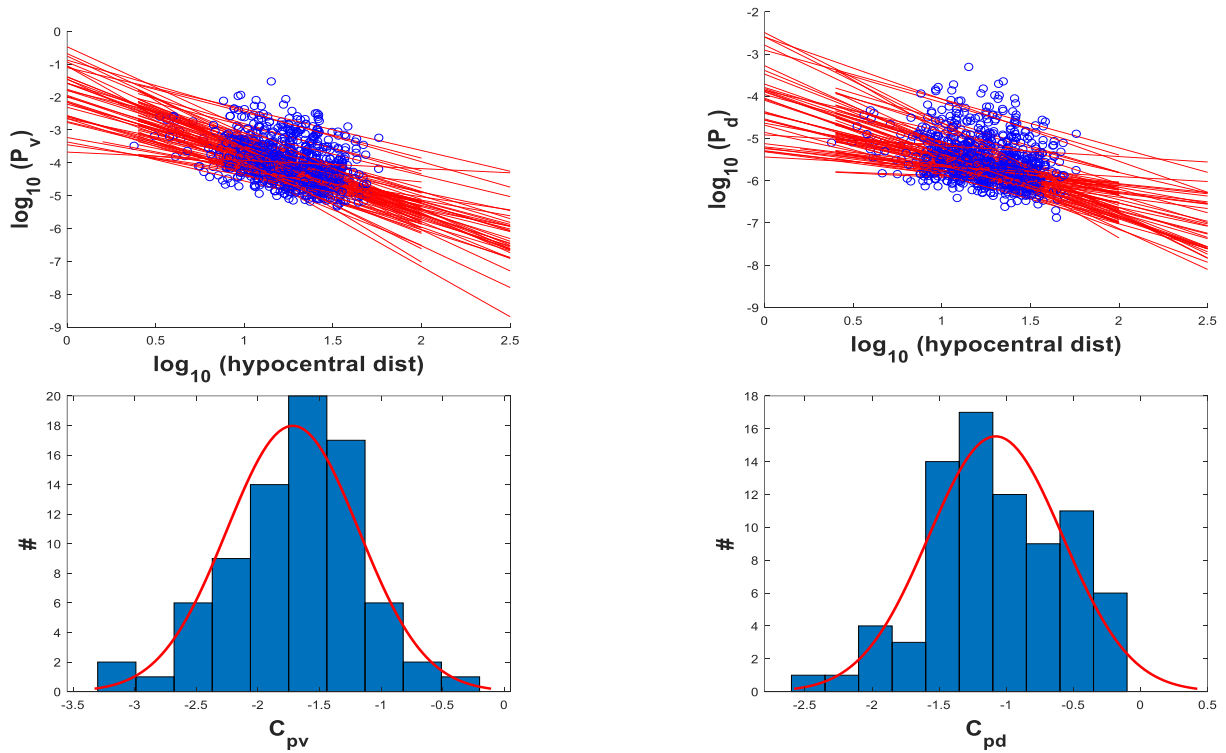


**Figure A2.** Attenuation coefficient for Nagano region.

**Table A1**

Nagano region: In the columns you can progressively find the origin time (UTC), the latitude, longitude, depth, magnitude (Mv), strike, dip and slip of first plane and strike, dip and slip of auxiliary plane, RSM on amplitude and RMS on the polarity.

yyyy.mm.dd.hh.mm.ss.ss	Latitude	longitude	depth	Mag	Stri1	Dip1	Rak1	Stri2	Dip2	Rak2	RMS	RMS_P
2011.05.01.16.32.28	137.98	36.34	2.05	-0.17	181	86	68	81	22	169	0.04	0.00
2011.05.02.19.11.00	137.98	36.23	12.31	0.55	299	62	51	179	47	140	0.25	0.25
2011.05.02.19.48.01	137.97	36.23	9.23	0.07	183	87	-3	273	87	-177	0.05	0.00
2011.05.02.23.59.02	138.03	36.40	3.59	1.16	280	73	-135	174	47	-23	0.29	0.06
2011.05.03.10.44.58	138.00	36.34	3.08	0.13	98	85	-145	5	55	-6	0.11	0.00
2011.05.03.20.12.01	138.00	36.23	8.72	0.50	353	70	94	161	20	79	0.28	0.11
2011.05.03.21.47.56	138.00	36.34	3.59	-0.38	343	26	-107	182	65	-82	0.10	-1.00
2011.05.05.20.10.48	137.94	36.24	4.10	0.16	355	47	-27	104	71	-134	0.08	0.00
2011.05.05.21.28.28	138.04	36.31	3.08	0.10	354	26	23	243	80	114	0.22	0.00
2011.05.05.23.06.59	137.94	36.24	4.10	-0.10	335	56	-59	108	45	-127	0.15	0.25
2011.05.06.20.11.04	137.94	36.24	2.56	0.23	109	67	-144	3	57	-28	0.21	0.00
2011.05.07.16.29.28	137.99	36.43	4.62	0.69	193	79	97	340	13	58	0.24	0.29
2011.05.07.22.18.43	137.77	36.56	4.62	0.51	187	87	75	86	15	169	0.24	0.25
2011.05.07.22.37.20	138.00	36.28	8.72	-0.04	310	61	106	99	33	64	0.16	0.25
2011.05.09.01.38.52	137.94	36.24	10.77	0.06	171	86	25	79	65	176	0.16	0.00
2011.05.09.03.37.44	137.87	36.37	5.13	-0.32	346	87	-42	79	48	-176	0.07	-1.00
2011.05.09.10.35.30	138.04	36.49	8.72	0.70	225	76	-89	41	14	-94	0.21	0.20
2011.05.09.16.17.35	137.99	36.34	9.74	0.69	316	58	121	87	43	51	0.07	0.00
2011.05.09.18.55.25	138.04	36.49	8.72	-0.11	25	85	20	293	70	175	0.10	0.00
2011.05.10.01.03.40	137.98	36.34	8.21	1.88	285	62	158	26	71	30	0.29	0.14
2011.05.10.01.35.46	137.99	36.34	8.21	0.57	99	63	63	327	37	132	0.20	0.33
2011.05.10.01.57.26	138.03	36.40	2.56	-0.15	294	80	109	51	21	28	0.03	0.33
2011.05.10.02.07.24	137.92	36.22	8.21	1.34	183	79	30	87	61	167	0.30	0.25
2011.05.10.03.45.33	137.98	36.34	9.23	1.84	327	39	139	91	66	59	0.30	0.33
2011.05.10.09.13.07	138.00	36.34	8.72	0.43	82	37	-7	178	86	-127	0.07	0.33
2011.05.10.13.07.01	137.91	36.31	5.64	0.13	208	87	-3	298	87	-177	0.07	0.33
2011.05.10.15.01.37	138.00	36.34	8.72	0.68	319	56	121	92	45	53	0.20	0.00
2011.05.10.18.55.50	137.92	36.22	8.72	0.85	269	51	144	24	63	45	0.26	0.17
2011.05.10.19.07.32	137.91	36.24	8.72	0.04	189	70	-177	98	87	-20	0.04	0.00
2011.05.11.10.10.36	137.96	36.53	14.87	0.47	19	37	55	240	60	113	0.03	0.00
2011.05.11.13.16.14	137.88	36.54	6.15	0.81	237	77	100	19	16	53	0.07	0.25
2011.05.11.15.09.17	137.88	36.55	7.18	0.53	245	77	85	86	14	111	0.21	0.00
2011.05.11.18.15.12	137.88	36.54	5.64	0.27	276	77	91	92	13	86	0.09	0.33
2011.05.12.04.28.02	137.89	36.55	6.15	0.29	255	74	87	86	16	100	0.18	0.00
2011.05.12.05.51.25	137.91	36.29	1.54	0.06	26	82	-69	136	22	-159	0.20	0.33
2011.05.12.06.14.11	138.05	36.50	7.69	0.72	332	79	22	238	68	168	0.24	0.25
2011.05.15.05.40.41	138.00	36.33	3.08	-0.15	201	85	99	320	10	29	0.04	0.20
2011.05.15.18.15.07	137.99	36.34	9.74	0.21	57	49	93	232	41	87	0.13	0.00
2011.05.16.11.10.08	138.03	36.40	1.03	0.79	31	59	53	267	47	135	0.25	0.00
2011.05.16.13.25.05	137.98	36.34	8.72	2.55	119	73	-161	23	72	-18	0.32	0.27
2011.05.16.13.26.24	137.99	36.34	9.74	0.46	204	60	62	71	40	129	0.06	0.33
2011.05.16.13.30.01	138.00	36.34	9.23	0.74	128	74	-93	319	16	-80	0.23	0.25
2011.05.16.15.19.29	137.98	36.34	7.18	1.06	344	54	-45	104	55	-134	0.28	0.08
2011.05.16.18.45.53	137.98	36.34	9.23	0.79	91	68	-137	342	51	-29	0.28	0.00

2011.05.17.01.19.13	138.03	36.42	6.15	0.34	23	71	155	122	66	21	0.18	0.00
2011.05.17.03.12.17	138.00	36.35	8.72	0.11	40	61	86	228	29	97	0.02	0.00
2011.05.17.03.57.38	137.94	36.24	5.64	0.31	51	68	94	220	22	80	0.21	0.20
2011.05.17.06.14.25	137.92	36.22	8.72	0.75	103	55	174	196	85	35	0.28	0.17
2011.05.18.05.17.58	138.00	36.34	10.26	0.24	51	47	35	295	65	131	0.13	0.00
2011.05.20.06.47.51	138.03	36.49	9.74	-0.34	164	63	-32	270	62	-149	0.18	0.00
2011.05.21.03.43.35	138.05	36.49	7.69	0.05	230	86	-92	77	4	-63	0.19	0.17
2011.05.22.03.56.09	137.96	36.26	6.15	-0.01	13	79	27	277	64	168	0.15	0.00
2011.05.22.10.45.49	138.04	36.49	7.69	0.66	162	42	78	358	49	101	0.33	0.33
2011.05.22.11.22.23	138.05	36.49	6.15	-0.12	233	74	144	334	56	20	0.20	0.00
2011.05.24.02.35.30	137.98	36.34	9.23	-0.02	101	57	-127	335	48	-47	0.18	0.00
2011.05.26.17.23.44	137.99	36.35	11.28	0.18	185	38	90	5	52	90	0.15	0.33
2011.05.28.18.40.50	138.00	36.29	8.72	0.37	14	60	34	265	61	145	0.07	0.00
2011.05.31.03.57.52	137.91	36.35	7.69	-0.26	170	73	-3	261	87	-163	0.27	0.00
2011.05.31.14.47.39	138.06	36.41	5.64	-0.08	350	28	171	88	86	62	0.21	0.25

**Table A2**

Rocca San Felice, manual arrival time picking: In the columns you can progressively find the date, the origin time (UTC), the latitude, longitude, depth, magnitude, strike, dip and slip of first plane and strike, dip and slip of auxiliary fault plane, error from 68% confidence ellipsoide for strike, dip and slip of each event.

yyyy-mm-dd	hh:mm:ss	Latitude	longitude	depth	Mag	Stri1	Dip1	Rak1	Stri2	Dip2	Rak2	e_s	e_d	e_r
2020-07-03	09:32:32	40.9380	15.1595	13.75	1.1	354	85	-133	258	43	-8	44	19	34
2020-07-03	16:13:16	40.9572	15.1657	14.89	1.1	314	41	-46	82	62	-121	43	17	30
2020-07-03	09:30:59	40.9435	15.1475	9.74	1.9	341	48	-78	143	43	-103	39	10	36
2020-07-03	16:14:25	40.9375	15.1502	9.62	3.0	332	57	-119	197	43	-54	3	7	4
2020-07-03	16:15:06	40.9482	15.1188	7.50	1.6	48	73	-128	297	41	-26	28	16	30
2020-07-03	16:17:41	40.9505	15.1530	13.40	1.4	28	72	-83	185	19	-112	35	15	35
2020-07-03	16:16:58	40.9502	15.1468	10.47	1.2	25	71	-96	223	20	-73	43	25	34
2020-07-03	16:18:11	40.9450	15.1478	10.00	1.9	20	52	-92	203	38	-88	10	8	10
2020-07-03	16:18:55	40.9472	15.1442	9.84	1.4	6	69	-61	129	35	-142	19	14	17
2020-07-03	16:21:40	40.9450	15.1698	13.82	0.8	351	90	-150	261	60	0	22	11	36
2020-07-03	16:23:35	40.9227	15.1717	13.59	0.9	343	44	-147	228	68	-51	39	22	40
2020-07-03	16:24:49	40.9353	15.1522	12.37	1.1	341	39	-90	161	51	-90	65	31	60
2020-07-03	16:19:23	40.9440	15.1513	10.55	3.0	360	61	-80	160	31	-107	7	13	8
2020-07-03	16:29:43	40.9492	15.1190	7.21	0.9	15	69	-136	266	50	-28	25	18	35
2020-07-03	16:50:08	40.9462	15.1545	13.16	1.9	19	58	-61	153	42	-128	21	10	16
2020-07-03	16:55:33	40.9485	15.1337	9.32	1.3	18	75	-72	148	23	-138	54	16	52
2020-07-03	18:13:27	40.9420	15.1815	15.30	1.0	278	33	-78	84	58	-98	48	24	44
2020-07-03	18:00:10	40.9507	15.1357	9.23	1.2	11	80	-71	128	22	-151	28	16	28
2020-07-03	18:32:24	40.9522	15.1137	8.14	0.5	275	37	-93	98	53	-88	34	12	37
2020-07-03	18:35:07	40.9503	15.1343	9.43	0.9	58	68	-48	171	46	-149	33	21	16
2020-07-03	18:23:24	40.9468	15.1592	13.33	1.3	357	38	-8	93	85	-128	14	11	4
2020-07-03	18:36:08	40.9333	15.1728	14.27	1.3	331	61	-110	188	35	-58	13	24	10
2020-07-03	19:19:56	40.9428	15.1690	13.25	0.8	301	31	-90	121	59	-90	94	12	53
2020-07-03	19:42:24	40.9470	15.1728	13.33	0.7	317	48	-78	119	43	-103	31	7	45
2020-07-03	19:46:21	40.9428	15.1673	13.14	0.6	337	67	-93	165	23	-83	25	11	47
2020-07-03	19:05:29	40.9470	15.1413	10.22	2.6	341	61	-121	212	41	-47	4	4	6
2020-07-03	19:47:25	40.9467	15.1395	8.88	1.2	347	57	-66	128	40	-122	8	10	12
2020-07-03	20:50:39	40.9438	15.1482	10.34	1.6	349	31	-91	170	59	-89	6	5	7
2020-07-03	20:51:00	40.9455	15.1665	14.74	1.6	280	31	-150	164	75	-63	64	4	26
2020-07-03	23:27:12	40.9395	15.1590	13.31	1.0	7	55	-102	207	37	-74	37	17	24
2020-07-03	21:03:59	40.9402	15.1575	11.93	0.8	1	69	-90	181	21	-90	51	17	58
2020-07-04	00:44:57	40.9418	15.1515	11.59	1.5	27	60	-84	195	31	-100	2	2	3
2020-07-04	00:47:47	40.9500	15.1527	12.55	0.9	339	43	-72	135	49	-106	49	18	34
2020-07-04	21:12:42	40.9535	15.1345	13.19	1.2	351	51	-131	225	54	-51	46	22	31
2020-07-04	12:34:03	40.9362	15.1537	12.19	2.7	335	58	-82	140	33	-103	1	3	3
2020-07-05	11:47:37	40.9450	15.1492	9.52	1.4	319	39	-112	166	54	-73	39	19	39
2020-07-05	12:35:05	40.9370	15.1697	13.28	1.5	295	38	-72	93	54	-104	41	11	20
2020-07-05	13:23:29	40.9405	15.1455	11.99	1.8	351	41	-66	140	53	-109	7	11	18
2020-07-05	13:43:42	40.9532	15.1438	13.17	1.5	311	31	-70	108	61	-102	28	6	42
2020-07-05	13:59:26	40.9425	15.1608	15.16	1.4	10	71	-100	218	21	-63	23	21	39
2020-07-05	13:25:35	40.9453	15.1422	11.49	1.9	339	43	-72	135	50	-106	2	5	2
2020-07-05	14:06:43	40.9333	15.1627	12.77	2.8	11	61	-31	117	63	-147	2	6	5
2020-07-05	14:09:11	40.9513	15.1330	8.54	2.0	343	59	-38	95	58	-142	3	5	3
2020-07-05	14:29:54	40.9523	15.1460	12.73	0.9	11	65	-100	214	27	-70	44	26	22

2020-07-05	14:14:04	40.9388	15.1467	9.05	1.2	23	45	-78	186	46	-102	3	8	2
2020-07-05	14:35:04	40.9488	15.1463	10.32	1.1	20	64	-52	139	45	-142	27	13	29
2020-07-05	15:18:40	40.9328	15.1652	11.82	2.8	4	43	-58	144	55	-116	5	10	8
2020-07-05	15:19:26	40.9287	15.1502	10.73	1.5	28	77	-139	287	50	-17	29	19	26
2020-07-05	16:05:50	40.9545	15.1363	9.79	1.0	63	76	-77	199	19	-132	37	15	26
2020-07-05	16:19:39	40.9528	15.1518	12.67	1.2	321	31	-30	77	75	-117	65	21	43
2020-07-05	16:51:16	40.9367	15.1552	13.37	1.2	351	51	-120	214	48	-58	49	28	27
2020-07-05	15:25:27	40.9438	15.1460	10.84	1.4	9	69	-102	220	24	-62	34	21	31
2020-07-05	17:45:24	40.9380	15.1567	10.65	2.3	45	55	-96	235	35	-82	2	5	5
2020-07-05	18:29:51	40.9463	15.1410	10.21	1.5	1	51	-60	138	48	-122	11	15	14
2020-07-05	19:12:57	40.9337	15.1553	11.09	2.1	337	36	-79	143	55	-98	30	9	50
2020-07-05	19:19:42	40.9430	15.1492	10.54	2.1	347	46	-67	135	49	-112	2	0	2
2020-07-06	04:26:04	40.9497	15.1587	13.72	1.3	61	61	-120	291	41	-48	29	9	18
2020-07-06	05:18:05	40.9423	15.1492	10.00	1.4	347	55	-63	125	43	-123	4	8	4
2020-07-07	02:23:39	40.9452	15.1258	7.84	0.4	340	44	-28	91	71	-130	20	16	26
2020-07-07	11:49:49	40.9303	15.1600	12.26	1.0	3	60	-84	171	31	-100	63	31	50
2020-07-06	16:55:15	40.9407	15.1683	13.62	1.2	353	53	-74	148	40	-110	11	8	21
2020-07-10	05:07:24	40.9393	15.1495	8.93	1.9	28	82	-43	125	48	-169	12	6	15
2020-07-10	22:45:43	40.9505	15.1192	8.87	0.6	328	73	-78	112	21	-124	29	17	33
2020-07-10	05:08:05	40.9450	15.1628	10.40	1.2	51	59	-90	231	31	-90	8	8	24

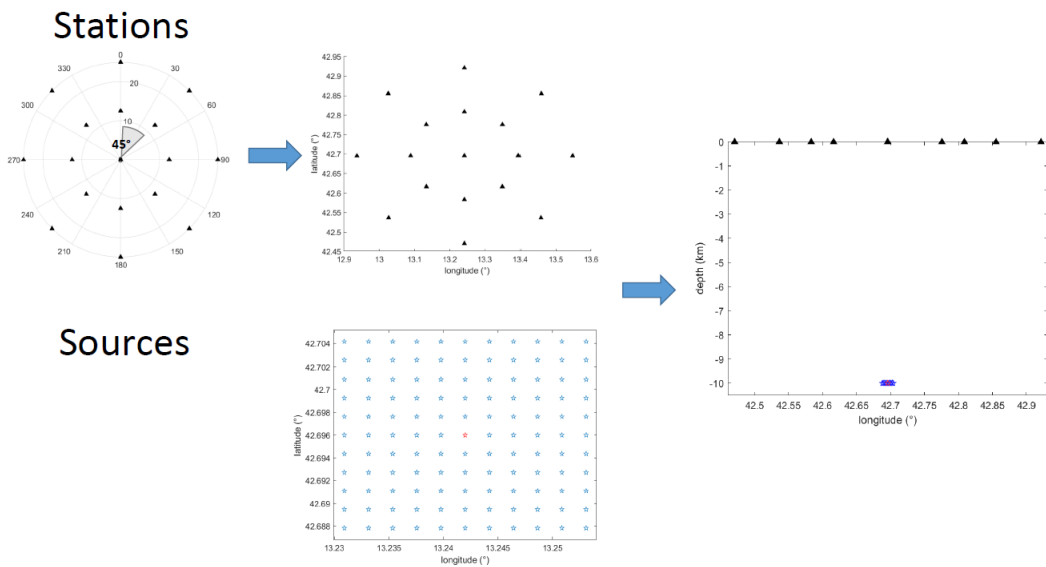
**Table A3**

Rocca San Felice, automatic arrival time picking. In the columns you can progressively find the date, the origin time (UTC), the latitude, longitude, depth, magnitude, strike, dip and slip of first plane and , dip and slip of auxiliary fault plane, error from 68% confidence ellipsoide for strike, dip and slip of each event analysed with automatic picking performed by PRESTO.

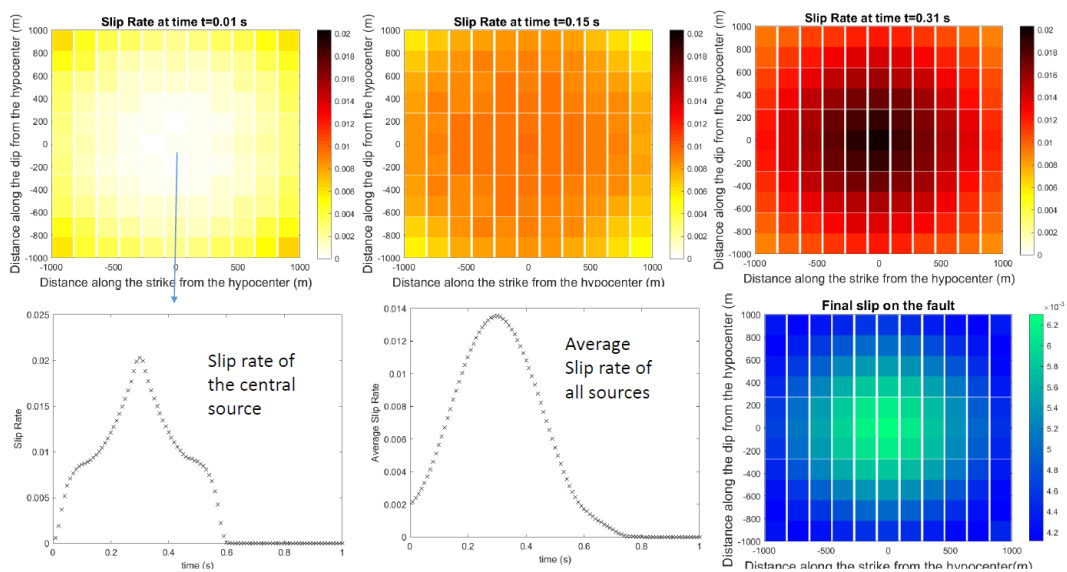
yyyy-mm-dd	hh:mm:ss	latitude	longitude	depth	Mag	Stri1	Dip1	Rak1	Stri2	Dip 2	Rak2	e_s	e_d	e_r
2020-07-03	09:30:59	40.9435	15.1475	9.90	1.9	60	66	-96	253	25	-78	22	12	24
2020-07-03	16:14:25	40.9375	15.1502	7.90	3.0	355	41	-66	144	53	-109	55	41	63
2020-07-03	16:15:06	40.9482	15.1188	10.36	1.6	229	20	19	121	84	109	63	21	66
2020-07-03	16:16:58	40.9502	15.1468	3.74	1.2	334	75	-51	82	41	-157	19	16	42
2020-07-03	16:18:11	40.9450	15.1478	12.76	1.9	36	77	-93	228	13	-78	26	13	38
2020-07-03	16:18:55	40.9472	15.1442	13.71	1.4	298	62	-111	157	34	-56	41	18	22
2020-07-03	16:19:23	40.9440	15.1513	11.78	3.0	342	62	-69	123	34	-124	18	16	35
2020-07-03	16:29:43	40.9492	15.1190	7.40	0.9	341	41	-20	86	77	-129	43	38	69
2020-07-03	16:55:33	40.9485	15.1337	12.70	1.3	332	71	-116	208	32	-38	54	25	61
2020-07-03	18:00:10	40.9507	15.1357	13.31	1.2	31	39	-25	141	75	-126	21	27	28
2020-07-03	18:23:24	40.9468	15.1592	14.84	1.3	341	50	0	71	90	-140	30	12	18
2020-07-03	18:36:08	40.9333	15.1728	12.82	1.3	13	42	-113	223	52	-71	54	20	43
2020-07-03	19:05:29	40.9470	15.1413	10.12	2.6	21	39	-79	187	52	-99	14	13	16
2020-07-03	19:47:25	40.9467	15.1395	10.05	1.2	264	48	-95	92	42	-84	29	11	42
2020-07-03	20:50:39	40.9438	15.1482	10.79	1.6	334	27	-94	158	63	-88	30	14	27
2020-07-03	20:51:00	40.9455	15.1665	8.07	1.6	299	55	-16	38	77	-144	42	21	27
2020-07-04	00:44:57	40.9418	15.1515	11.38	1.5	315	41	-134	187	62	-59	24	14	27
2020-07-04	00:47:47	40.9500	15.1527	7.01	0.9	329	39	-14	70	81	-128	47	16	50
2020-07-04	12:34:03	40.9362	15.1537	11.67	2.7	346	60	-71	131	35	-120	26	13	38
2020-07-05	11:47:37	40.9450	15.1492	9.07	1.4	11	34	-80	179	57	-97	47	24	52
2020-07-05	12:35:05	40.9370	15.1697	7.00	1.5	317	21	26	203	81	109	48	25	52
2020-07-05	13:23:29	40.9405	15.1455	12.13	1.8	269	29	-51	46	68	-109	51	15	55
2020-07-05	13:25:35	40.9453	15.1422	12.45	1.9	3	69	-76	149	25	-121	43	20	30
2020-07-05	14:06:43	40.9333	15.1627	11.98	2.8	328	41	-93	152	49	-87	50	11	31
2020-07-05	14:09:11	40.9513	15.1330	9.40	2.0	335	57	-60	108	43	-128	49	18	44
2020-07-05	14:14:04	40.9388	15.1467	9.54	1.2	54	43	-49	185	59	-121	17	23	52
2020-07-05	14:35:04	40.9488	15.1463	6.67	1.1	347	83	-152	253	62	-8	22	15	36
2020-07-05	15:18:40	40.9328	15.1652	8.85	2.8	335	21	-76	140	70	-95	16	12	33
2020-07-05	15:19:26	40.9287	15.1502	10.73	1.5	285	45	-16	26	79	-134	25	28	48
2020-07-05	15:25:27	40.9438	15.1460	12.16	1.4	285	30	-26	38	77	-117	43	17	52
2020-07-05	17:45:24	40.9380	15.1567	9.62	2.3	328	42	-53	103	58	-118	32	17	40
2020-07-05	18:29:51	40.9463	15.1410	13.36	1.5	35	80	-111	281	23	-26	32	24	36
2020-07-05	19:12:57	40.9337	15.1553	11.24	2.1	308	43	-89	127	47	-91	34	13	22
2020-07-05	19:19:42	40.9430	15.1492	11.22	2.1	318	48	-73	113	45	-108	43	16	16
2020-07-06	04:26:04	40.9497	15.1587	1.89	1.3	300	46	-6	34	86	-136	31	21	45
2020-07-06	05:18:05	40.9423	15.1492	11.10	1.4	267	22	-48	43	74	-105	34	20	39
2020-07-06	16:55:15	40.9407	15.1683	21.27	1.2	20	76	-95	221	15	-70	60	19	52
2020-07-10	05:07:24	40.9393	15.1495	10.58	1.9	233	59	21	132	72	147	25	11	18
2020-07-10	05:08:05	40.9450	15.1628	9.93	1.2	242	81	-141	145	52	-11	28	33	33

## Test on Beamforming and stacking technique with a point source

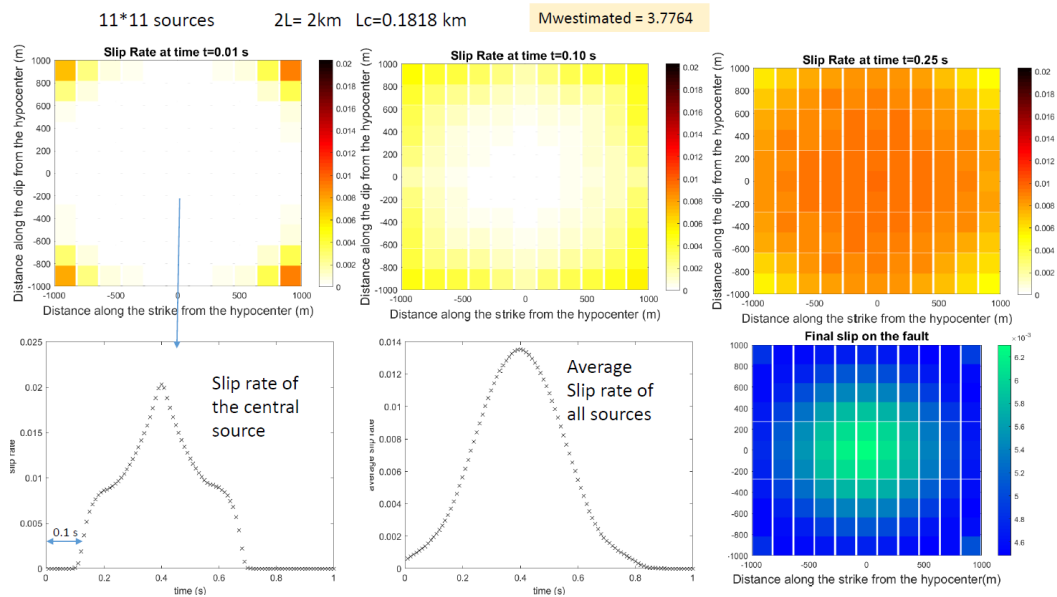
**TEST 1:** Configuration of candidate sources (blue stars), hypocenter located at a depth equal to 10 km (red star) and stations (black triangles). The medium is homogenous, the source time function has a triangle shape, and we model an earthquake equal to Mw 4.0 with a rupture velocity equal to 3.3 km/s, The source fault is square, horizontally oriented and its length is 2 Km. The final slip on the fault is constant. The duration of source is 0.6 s and origin time=0. the prescribed slip rate function has a triangular shape. We directly back project the synthetic signals without applying any filter for a specific frequency band.



We retrieve the proper duration for the central source. There is an effect of smearing for the final slip distribution of the fault, but it is properly centred on the hypocenter.

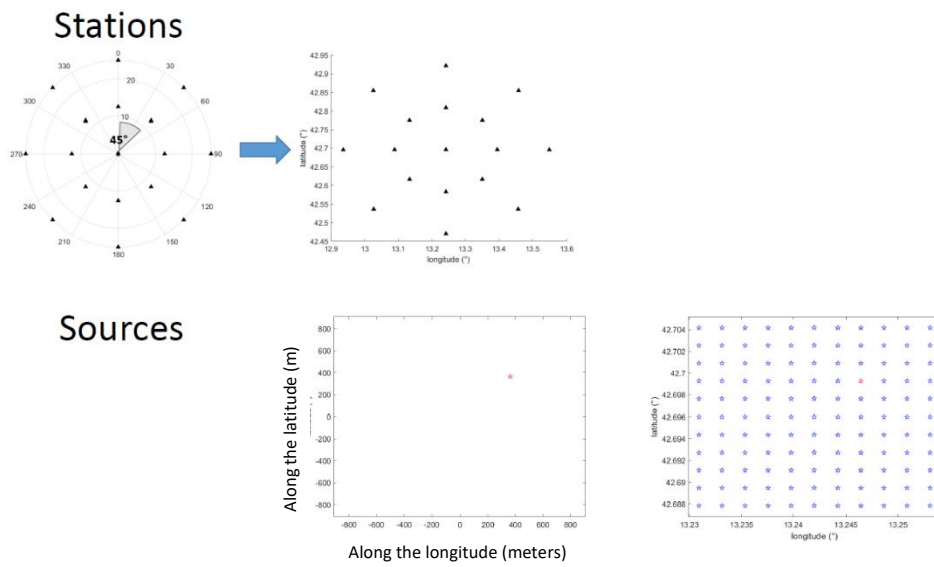


**TEST2: same as TEST1 but origin time equal to 0.1 s.** Configuration of candidate sources (blue stars), hypocenter located at 10 km in depth (red star) and stations (black triangles) is as in Test 1. The medium is homogenous, the source time function has a triangle shape, and we model an earthquake equal to Mw 4.0 with a rupture velocity equal to 3.3 km/s, The source fault is square, horizontally oriented and its length is 2 Km. The final slip on the fault is constant. The duration of source is 0.6 s and origin time=0.1. We retrieve the proper duration for the central source. There is an effect of tapering for the final slip

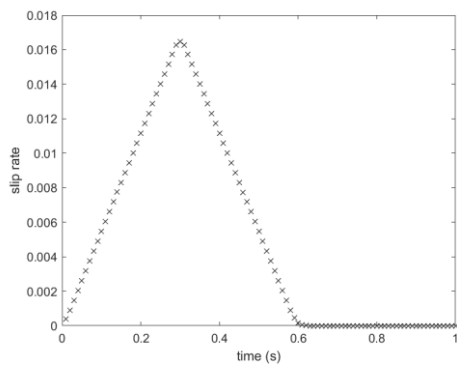


distribution of the fault, but it is properly centred on the hypocenter.

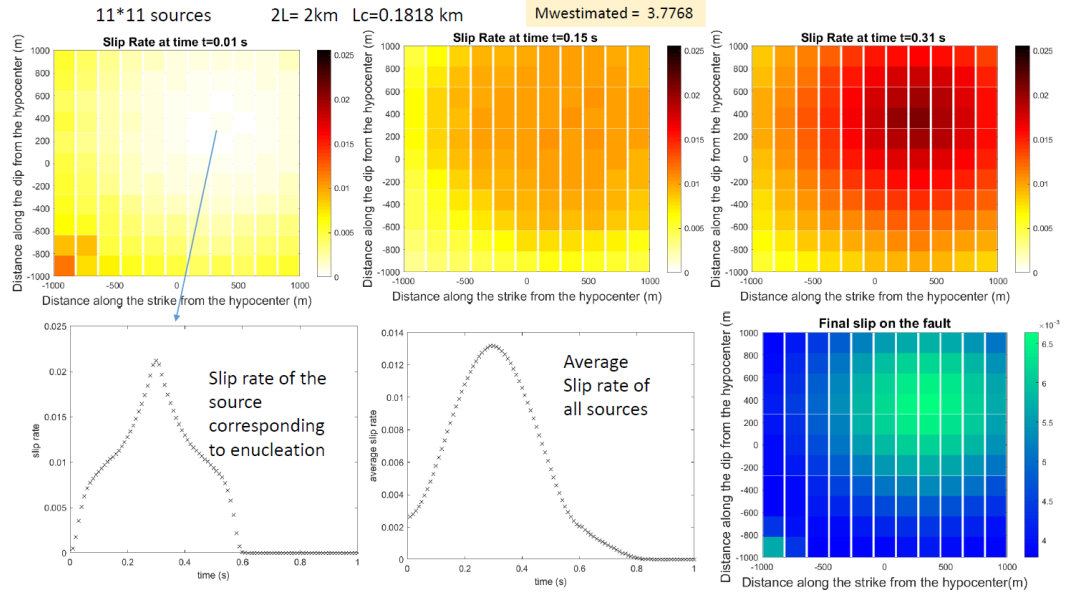
**TEST 3: Hypocenter not centered in the plane of investigation** Configuration of candidate sources (blue stars), hypocenter at depth 10 km (red star) and stations (black triangles). The medium is homogenous, the source time function has a triangle shape, and we model an earthquake equal to Mw 4.0 with a rupture velocity equal to 3.3 km/s. The source fault is square, horizontally oriented and its length is 2 Km. The final slip on the fault is constant. The duration of source is 0.6 s and origin time=0. The hypocenter in this test is located not in the center of the plane of investigation for backprojection.



The theoretical slip rate should be as in the following picture.

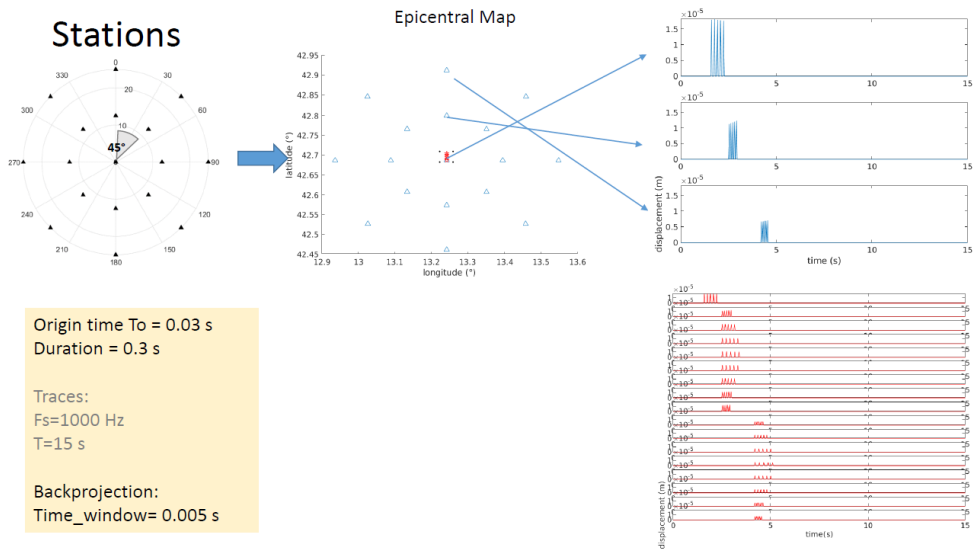


We retrieve the proper duration for the central source. There is an effect of smearing for the final slip distribution of the fault, but it is properly located on the fault plane.

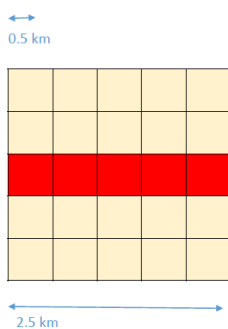


## Test on Beamforming and stacking technique with a line source

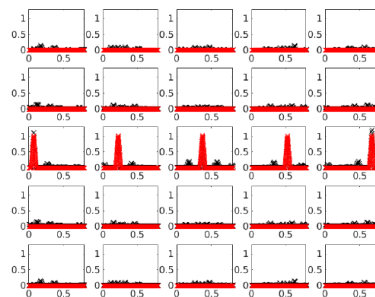
**TEST 4:** Configuration of sub-sources (red star) and stations (black triangles). The medium is homogenous, the source time function of sub-sources has a triangle shape, and we model an earthquake equal to Mw 4.0 with a rupture velocity constant and equal to 3.3 km/s. The source is a source line with  $L=2.5$  km and we model a unilateral rupture propagating from source to north.



Using all stations we retrieved the highest value of final slip at the border, highlighted by the initial and stopping phases, while the true slip model was constant (red squares in the following sketch). The red arrow indicates the direction of propagation.

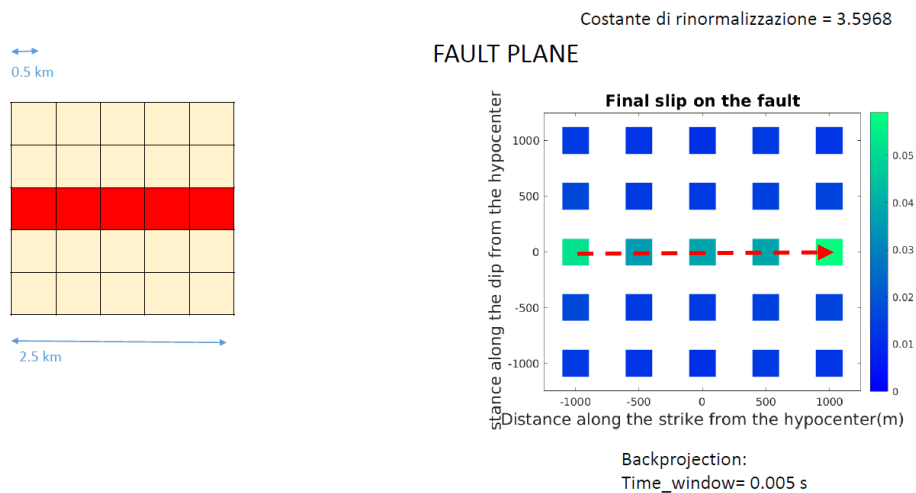


FAULT PLANE Slip rate on subsources



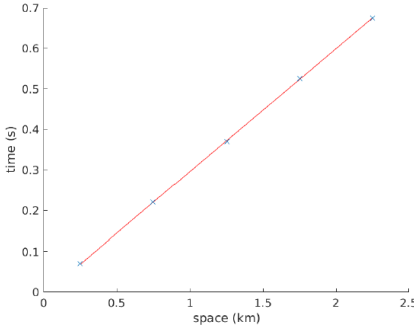
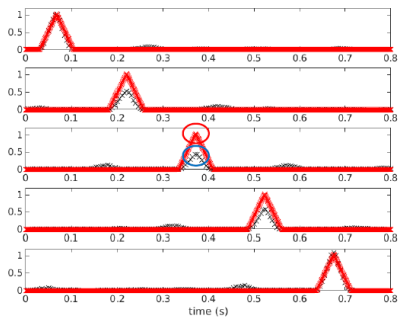
Backprojection:  
Time\_window= 0.005 s

The above image is the representation of the investigated fault plane, while in the following image we focus on the cells referring to the line source in which we properly observe the highest value of the slip rate. The red curves represent the theoretical slip rate of the subsources, while the black is the retrieved one. There is a good agreement for the first and last cell, while the slip rate for the central subsources is not completely retrieved due to the fact that the displacement observed at the stations could be

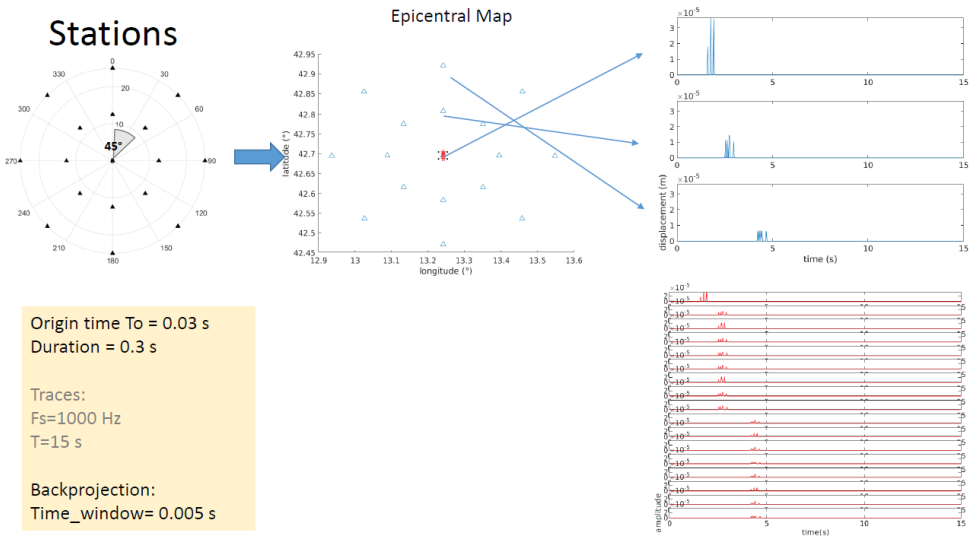


equivalently produced by the two adjacent sub-sources. This noise is also present in the other subsources, albeit to a lesser entity. In fact, due to the symmetry because of the horizontal fault plane, there is an equivalence between the single subsources along the central line or two symmetrical and equidistant subsources with respect to it and that dislocates soon later than it and in a less entity respect the central one, but in equal measure among each other. Furthermore, we picked the time at which we observe the maximum of the slip rate along the line fault, and we properly retrieved a constant rupture speed.

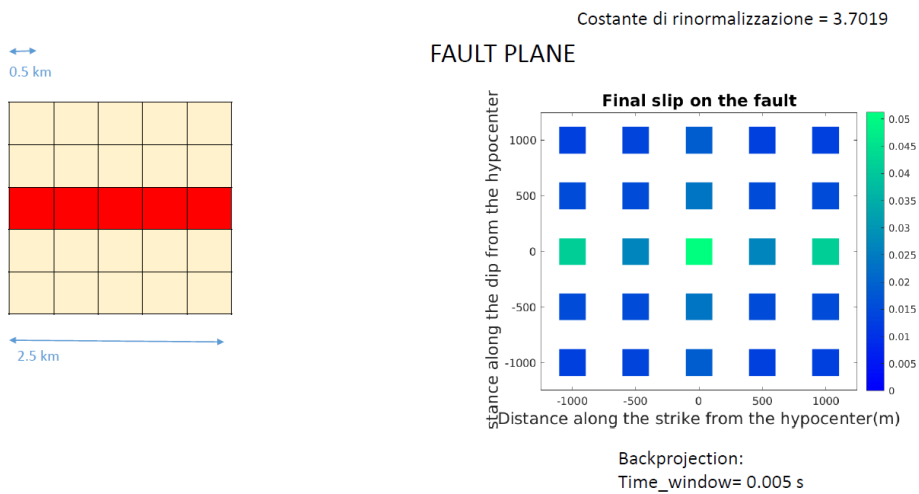
Taking time at which we have maximum of slip rate



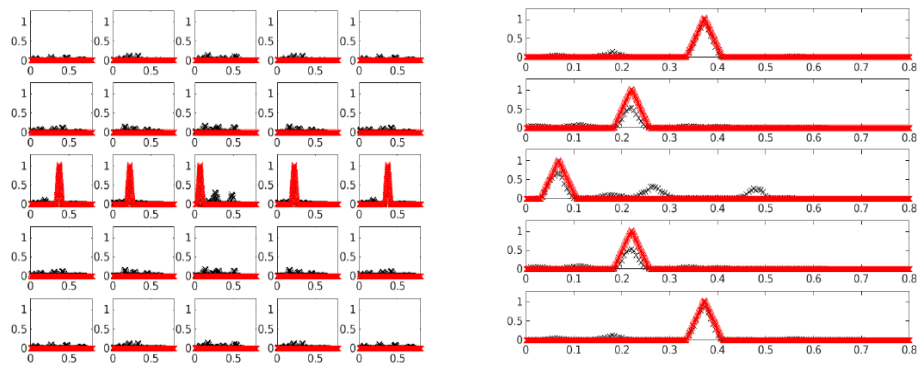
**TEST 5: Bilateral rupture** Configuration of sub-sources (red star) and stations (black triangles). The medium is homogenous, the source time function of sub-sources has a triangle shape, and we model an earthquake equal to Mw 4.0 with a rupture velocity constant and equal to 3.3 km/s. The source is a source line with L=2.5 km and we model a bilateral rupture.



The highest values of final slip are located in the hypocenter and in the edge of the line source.



The timing of the slip rate is properly retrieved, as well as the 'true model' rupture speed (red line is theoretical slip rate while the black is the retrieved, in particular on the left side there is the slip rate on the entire fault and on the right the values on the cells corresponding on the 'true' line fault. The rupture is properly propagating from the hypocenter bilaterally, but with an underestimation of slip rate and of slip for cells not interested by the starting of rupture or its end, because of equivalently produced by the two adjacent sub-sources, producing for this reason some noise.

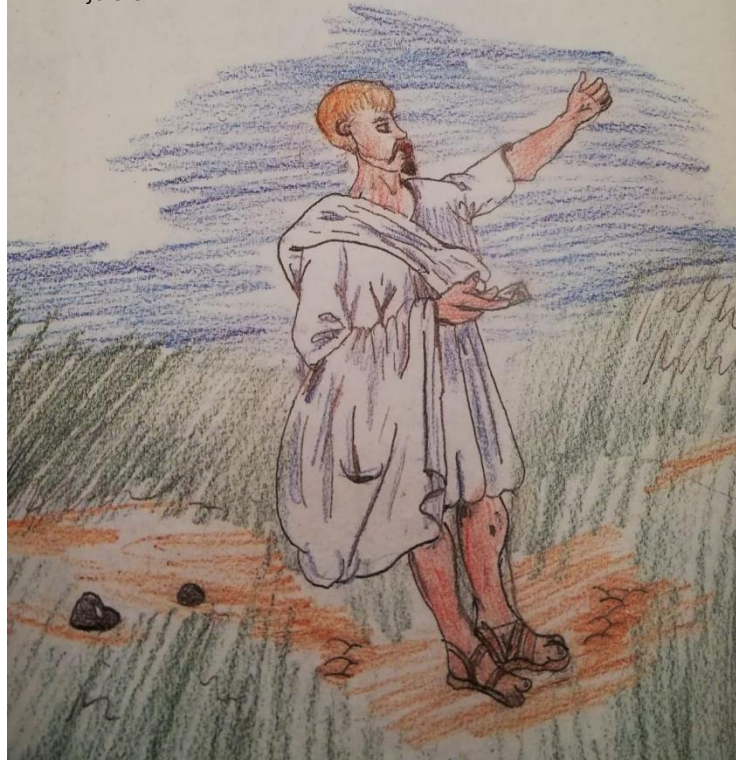


Backprojection:  
Time\_window= 0.005 s



"Caro amico Tacito,  
tu mi chiedi come morì mio zio, per farlo sapere ai posteri ed io ti  
sono grato, perché, così, egli sarà ricordato per sempre".

*"Dear friend Tacitus, you ask me how my uncle died to let posterity know  
and I am grateful to you because in this way he will be remembered  
forever".*



Tratto da Quaderno vesuviano, redatto a cura degli alunni  
di terza elementare della scuola G.Mazzini di San Giorgio a  
Cremano nell'anno scolastico 2000/2001

From the Quaderno vesuviano, edited by third grade  
students of primary school G.Mazzini of San Giorgio a  
Cremano in the 2000/2001 school year